Jianjun Fang

THE CLUSTERIZATION OF NUCLEAR MATTER IN A NEUTRON STAR UNDER STRONG MAGNETIC FIELDS

Tese de Doutoramento em Física, Ramo de Física Nuclear e das Partículas, orientada pela Prof. Dra. Constança Providência e pela Dra. Helena Pais e apresentada ao Departamento de Física da Faculdade de Ciências e Tecnologia da Universidade de Coimbra

Agosto de 2017

· U C ·

UNIVERSIDADE DE COIMBRA

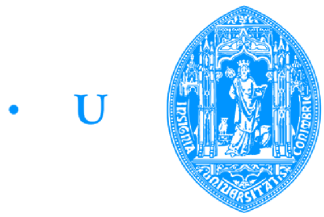

UNIVERSIDADE DE COIMBRA

The clusterization of nuclear matter in a neutron star under strong magnetic fields

Jianjun Fang

Supervisors: Prof. Dr. Constança Providência and Dr. Helena Pais

Department of Physics
Faculty of Science and Technology
University of Coimbra

August 2017

Acknowledgments

I should say thanks to many people for their help and encouragements. This thesis could not be finished if there is not their help.

First of all, I sincerely appreciate my supervisor Professor Constança Providência for introducing me these interesting, exciting topics. Working under Professor Providência' supervision is a pleasant and very lucky thing. Particularly, I am thankful for her quite patiently teaching me many scientific fundamentals during my study, spending much time to discuss the work with me, communicating a lot of researchers to discuss my work. She starts my research life. I will remember it all of my life.

I am very grateful to my second supervisor Dr. Helena Pais. She spent lots of time to discuss the calculations, programs with me, correct the text, give many useful comments. I also feel very lucky to have a such nice supervisor.

Much thanks should be given to all the other people in the Centre for Physics of the University of Coimbra (CFisUC): Professor João Providência, Professor Lucília Brito, Dr. Isaac Vidaña, Dr. Pedro Costa, Dr. Silvia Chiacchiera and Dr. Márcio Ferreira for their friendship, support and even the smile.

Thanks to the financial support from the project with the reference PTDC/FIS/113292/2009.

Last but not least, I would give my special thanks to my parents, my wife and my lovely daughter for their love and encouragements.

Resumo

Apresentamos um estudo da estabilidade da matéria no interior da crosta duma estrela de neutrões sob a ação de um campo magnético externo muito intenso, como os que poderão existir no interior de magnetares. Neste trabalho, consideramos campos magnéticos com intensidades da ordem de $2\times10^{15} < B < 5\times10^{16}$ G. O método utiliza um modelo de campo médio relativista da matéria nuclear acoplado ao campo magnético. O momento magnético anómalo de neutrões e protões é incluído, e o seu efeito estudado explicitamente. A estabilidade do estado fundamental é analisada, sendo calculada a relação de dispersão no formalismo da equação de Vlasov relativista para os modos longitudinais e usando a mesma interacção. Verificamos que o campo dá origem a uma heterogeneidade adicional na estrutura da crosta interna com flutuações significativas no tamanho do agregado com a densidade. Além disso, a densidade de transição crosta-núcleo pode aumentar de pelo menos 0.01 fm^{-3}, resultando num aumento significativo da massa e do momento de inércia da crosta. Verifica-se ainda que uma intensidade de campo suficientemente elevada pode dar origem a uma alternância de camadas de matéria nuclear homogénea e matéria com agregados nas camadas profundas da crosta interior.

Os efeitos simultâneos da intensidade do campo magnético, da energia de simetria e da temperatura no núcleo da crosta são discutidos. Sob a ação de campos magnéticos fortes, a extensão da crosta é muito sensível à dependência da energia de simetria na densidade. As propriedades que dependem da espessura da crosta podem estabelecer uma forte restrição na equação de estado. As spinodais termodinâmicas são usadas para estudar a estabilidade da matéria estelar a temperatura finita. É mostrado que o efeito do campo magnético sobre a extensão da transição da crosta-núcleo desaparece para temperaturas acima de 10^9 K. No entanto, para temperaturas inferiores a esse valor, o efeito é importante, e aumenta à medida que a temperatura diminui, devendo ser levado em consideração quando a evolução de magnetars é estudada.

Abstract

We study the stability of stellar matter in the inner crust of neutron stars under the effect of strong external magnetic fields, as the ones that may occur in magnetars. Quantizing magnetic fields with intensities in the range of $2 \times 10^{15} < B < 5 \times 10^{16}$ G are considered. We use relativistic mean-field models to describe nuclear matter coupled to the magnetic field. The anomalous magnetic moment of neutrons and protons are explicitly included in the study and their effect analyzed. The stability of the ground state is then examined with respect to longitudinal modes using the relativistic Vlasov formalism, and the explicit calculation of the dynamical spinodal. We find that the strong magnetic field introduces additional heterogeneity into the structure of the inner crust with significant fluctuations in the cluster size with density. It can extend the crust-core transition density by 0.01 fm^{-3}, or even more, which would result in a significant increase in the mass and moment of inertia of the crust and, perhaps most interestingly, at high enough field strength, we obtain layers of homogeneous nuclear matter sandwiched in-between clustered matter in the deep layers of the inner crust.

The simultaneous effects of the magnetic field intensity, and both the symmetry energy and the temperature, on the crust-core transition of a magnetar are also discussed. Under strong magnetic fields, the crust extension is very sensitive to the density dependence of the symmetry energy, and the properties that depend on the crust thickness could set a constraint on the equation of state. The thermodynamical spinodals are used to study the stability of stellar matter at finite temperature. It is shown that the effect on the extension of the crust-core transition is washed out for temperatures above 10^9 K. However, for temperatures below that value, a noticeable effect exists, that grows as the temperature decreases, and which should be taken into account when the evolution of magnetars is studied.

Publications

Three publications resulted from my PhD studies:

1. Jianjun Fang, Helena Pais, Sidney Avancini, and Constança Providência, *Larger and more heterogeneous neutron star crusts: A result of strong magnetic fields*, Phys. Rev. C **94**, 062801(R) (2016).

2. Jianjun Fang, Helena Pais, Sagar Pratapsi, Sidney Avancini, Jing Li, and Constança Providência, *Effect of strong magnetic fields on the crust-core transition and inner crust of neutron stars*, Phys. Rev. C **95**, 045802 (2017).

3. Jianjun Fang, Helena Pais, Sagar Pratapsi, and Constança Providência, *Crust-core transition of a neutron star: Effects of the symmetry energy and temperature under strong magnetic fields*, Phys. Rev. C **95**, 062801(R) (2017).

Contents

Acknowledgements i

Abstract iii

Publications vii

1 Introduction 1
- 1.1 Neutron stars . . . 1
  - 1.1.1 Constitution . . . 2
  - 1.1.2 The nuclear pasta phase . . . 3
- 1.2 Liquid gas phase transition . . . 6
- 1.3 The crust-core transition . . . 8
- 1.4 Collective modes . . . 9
- 1.5 Constraints on the EoS . . . 11
- 1.6 Magnetars . . . 13
- 1.7 Objectives . . . 16

2 Relativistic mean field models 17
- 2.1 Mean field approximation . . . 17
- 2.2 The equation of state . . . 18
  - 2.2.1 The $\sigma - \omega$ model . . . 18
  - 2.2.2 Generalizing the $\sigma - \omega$ model . . . 19
  - 2.2.3 Adjusting the parameters . . . 22
- 2.3 Equation of state of magnetized nuclear matter . . . 23
- 2.4 Neutron star structure . . . 25
- 2.5 The moment of inertia . . . 26

3 Collective modes and instability region 31
- 3.1 Dynamical spinodal under strong magnetic fields . . . 32
- 3.2 Thermodynamical spinodal under strong magnetic fields 39

4 Dynamical spinodal **45**
4.1 Spinodal section 45
4.2 Growth rates 53
4.3 Maximum growth rates 56
4.3.1 Thickness of the crust 65
4.3.2 Final comments 67

5 Thermodynamical spinodal **69**
5.1 Thermodynamical versus dynamical spinodal 69
5.2 Thickness of the crust within the thermodynamical spinodal 70
5.3 Joint effect of temperature and magnetic field on the thermodynamical spinodal section 75
5.4 Effect of temperature on the crust-core transition under a strong magnetic field 77
5.5 Effect of the magnetic field on the distillation effect . . . 83

6 Conclusions **91**

A Equations of motion of the fields **95**

B The coefficients of the determinant of the dispersion relation **97**

C Some useful integrals **101**

List of Figures **105**

List of Tables **110**

Bibliography **113**

Chapter 1

Introduction

1.1 Neutron stars

Neutron stars are one of the possible remnants of the end of the stellar evolution for very massive stars, with a mass larger than $8M_\odot$ [Shapiro and Teukolsky, 2004], and are formed in a type-II supernova explosion called core-collapse supernova. The mass of a typical neutron star is around $1.4M_\odot$ and the radius is about 10 km. They were first predicted by Baade and Zwicky [Baade and Zwicky, 1934] in 1934, and due to their exotic constitution, they have been attracting the curiosity of scientists ever since. Fifty years ago, in 1967, Jocelyn Bell and Anthony Hewish observed the first pulsar [Hewish et al., 1968].

Due to the extreme conditions (high pressures and densities, large isospin asymmetry, and high temperatures), which laboratories on earth cannot reach, neutron stars have become an amazing laboratory in the universe. The research of neutron stars attracts interest of scientists from many areas, such as nuclear and particle physics, astrophysics, cosmology and general relativity. In particular, nuclear physics plays an important role in understanding these objects, because the fundamental nuclear interaction is necessary to determine the equation of state (EoS), responsible for the constitution and structure of the stars. Furthermore, neutron stars can be thought of a giant very neutron-rich nucleus, meaning that understanding the constitution and properties of the star leads to a better understanding of the nuclear force. Astrophysical observations can, therefore, be used to put constrains on the properties of nuclear matter.

In September 2015, the first gravitational waves were detected by the LIGO interferometer [Abbott et al., 2016]. Their origin was the

collision of two massive blackholes. This has opened an important window to the observation of massive stars and neutron stars. Due to their extreme gravitational field, they are also strong candidates for gravitational wave observation. One expects that gravitational waves from supernova explosions, binary merging or neutron star oscillations could be detected in the near future.

Scientists hope to use various observations (electromagnetic radiation of different wavelengths and gravitational waves) together with theoretical methods to probe the properties of matter in a neutron star under extreme conditions.

1.1.1 Constitution

A neutron star roughly includes four different regions: atmosphere, outer crust, inner crust, and core, see Fig. 1.1.

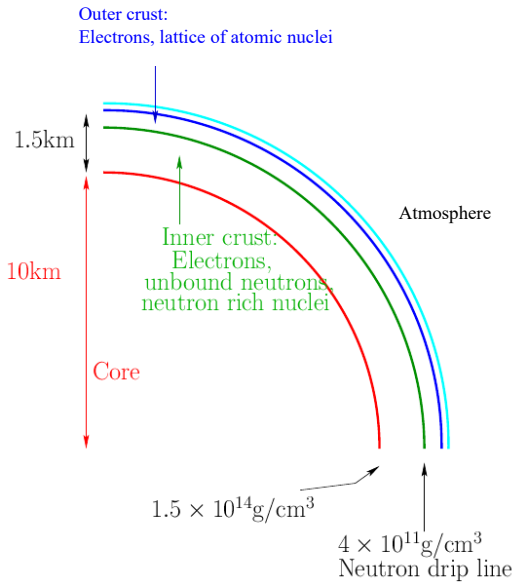

Figure 1.1: The schematic picture of the structure of a neutron star, taken from [Sharma, 2013].

The atmosphere is only a few centimeters thick and contributes very little to the total star mass, however it is very important in determining the spectrum and flux of the neutron star. It is essentially constituted by hydrogen and helium atoms.

The outer crust consists of a lattice of atomic nuclei, which are iron nuclei at the outer layer close to the atmosphere, immersed in an elec-

tron Fermi sea. From the top to the bottom layer of the outer crust, nuclei become more and more neutron rich, until neutrons drip out of the nuclei (free, unbound neutrons) at densities above the 4×10^{11} g cm^{-3}, and condense into a superfluid phase in some layers.

The region that starts at the onset of the neutron drip is called the inner crust, and it extends until the transition to the core occurs, at a density of $\sim 1.5 \times 10^{14}$ g cm^3. In this region, heavy clusters will form, embedded in a background gas of superfluid neutrons. These exotic shapes result from the competition between the short range nuclear force and the long range Coulomb force. These geometries will eventually melt, as the density increases towards the center of the star, and the transition to the core occurs.

The liquid core consists of a mixture of neutrons, protons and electrons. Due to the high Fermi pressure, muons and other exotic particles such as hyperons and pion and kaon mesons, or even deconfined quark matter, may appear.

1.1.2 The nuclear pasta phase

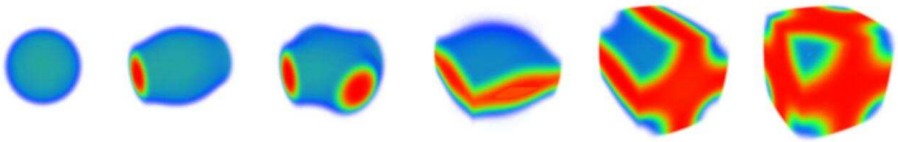

Figure 1.2: The nuclear pasta phases. From left to right: droplets, rods, cross-rods, slabs, tubes and bubbles. Figure taken from [Pais and Stone, 2012].

As the density increases in the crust, from ~ 0.001 up to ~ 0.1 fm^{-3}, [Sonoda et al., 2008, Sonoda et al., 2010, Avancini et al., 2008], and before an eventual transition to homogeneous matter occurs, heavy quasi-nuclei structures, immersed in a electron gas and neutron gas, will probably be formed.

Their geometry will be determined by the minimization of the free energy, and shapes such as droplets, rods, slabs, tubes, and bubbles, or others in between, could exist. An example of these exotic geometries is represented in Fig. 1.2, taken from [Pais and Stone, 2012], where it is shown the neutron density distribution at onset density of each phase. These heavy clusters, called the pasta phases, are constituted by protons and neutrons, and were first introduced by Ravenhall et

al. [Ravenhall et al., 1983] and Hashimoto et al. [Hashimoto et al., 1984].

These geometrical configurations have not only been predicted in nuclear matter, but they have also been observed in a variety of amorphous solids, crystals, and magnetic and biological materials [Watanabe and Sonoda, 2007, Moessner and Ramirez, 2006, Kuksenok et al., 2006].

The equilibrium structure of the pasta phases is a frustrated system that arises from the interplay between the surface energy of the nuclei, which is favoring large structures, and their Coulomb energy, which is favoring small structures, [Ravenhall et al., 1983, Horowitz et al., 2004b, Horowitz et al., 2005, Maruyama et al., 2005, Watanabe et al., 2005, Sonoda et al., 2008, Sonoda et al., 2010]. In fact, in neutron stars, where the pressure and densities are very high, the Coulomb energy becomes comparable in magnitude to the nuclear binding energy. Matter becomes frustrated and arranges itself in a regular periodic lattice of nonspherical clusters in order to minimize the Coulomb energy. The pasta phases are the ground-state of matter, if their free energy per particle is lower than the corresponding homogeneous matter state [Avancini et al., 2010].

Understanding nuclear matter under exotic conditions is still attracting the interest of the scientific community because the information that arrives to the surface of the star coming from the core has to go through the inner crust. Learning about the inner core is, therefore, only possible if the constitution of the outer and the inner crust are well understood. Besides, several properties of neutron stars, such as glitches, are attributed to the dynamics of the crust.

Recently, Pons et al [Pons et al., 2013] suggested that an indirect observation of the existence of a layer of pasta phases at the upper border of the inner crust is the fact that pulsars with periods above ~ 12 s have not been observed. They have shown that there seems to exist a direct correlation between the highly resistive layer in the inner crust of the stars, and the maximum observed spin period of isolated x-ray pulsars. This could be an evidence for the existence of the nuclear pasta phase.

Since the pioneer studies of Ravenhall et al [Ravenhall et al., 1983], the nuclear pasta phase has been studied, using either semiclassical liquid drop models or Thomas-Fermi methods [Lamb et al., 1983, Lattimer and Swesty, 1991, Lassaut et al., 1987]. Using the principle that the ground-state configuration of matter is the one that minimizes the free energy, the geometrical structures were obtained by calculating

the energy densities of each configuration in the range of densities and temperatures that they were expected to appear, and selecting the one that gave the lowest energy state.

Different formalisms have later been used to calculate these same geometrical structures, including classical and quantum molecular dynamics models [Horowitz et al., 2004c, Sonoda et al., 2008, Schneider et al., 2014], the Thomas-Fermi approximation within relativistic nuclear models [Shen et al., 1998, Maruyama et al., 2005, Avancini et al., 2008], and Hartree-Fock calculations with both non-relativistic and relativistic models [Gögelein and Müther, 2007, Newton and Stone, 2009, Pais and Stone, 2012].

Quantum molecular dynamics [Maruyama et al., 1998, Watanabe et al., 2001, Horowitz et al., 2004b, Horowitz et al., 2004a, Watanabe and Sonoda, 2005] simulations are another possible approach to model these exotic geometries. In this approach, a large number of nucleons is dynamically evolved in a cubic box with periodic boundary conditions. Here, the nuclear structures are not defined *a priori*, but one of the problems with this semiclassical microscopic treatment is that the effective nucleon-nucleon interaction is very schematic and the shell effects are missing.

The pasta phases have also been described within a classical molecular dynamics technique, based on the work of Pandharipande [Vicentini et al., 1985, Lenk and Pandharipande, 1986, Lenk et al., 1990] in Ref. [Dorso et al., 2012]. In this approach, the nucleons are treated as classical particles, which interact through a two-body potential. The coupled equations of motion of the many-body system need to be solved so that the time evolution of all particles are obtained. The microscopic structure of the nuclear medium is possible to obtain because the position and momentum for the particles is know at all times and for all particles [Dorso et al., 2012].

A fully self-consistent, non-relativistic 3D Skyrme-Hartree-Fock model of the nuclear pasta phase at finite temperature, that allows for a wide variety of possible nuclear formations, calculated self-consistently, has been used in Refs. [Newton and Stone, 2009, Newton, 2008, Pais, 2013, Pais and Stone, 2012] to study the nuclear pasta structures and the transition to the liquid uniform phase. In this approach, no predetermination of the shape is imposed, and the transition between the different shapes is self-consistent with no need to introduce different EoS.

The spherical Wigner-Seitz (WS) approximation, in which the generally nonspherical unit cell is replaced by a spherical one with the

same volume, has been used in several studies, like fully microscopic Hartree-Fock (HF) calculations of supernova matter [Bonche and Vautherin, 1981, Bonche and Vautherin, 1982], or in the relativistic Thomas-Fermi approximation [Avancini et al., 2008, Avancini et al., 2009, Avancini et al., 2010], within the framework of the non-linear Walecka model with a variety of effective Lagrangians. This approximation is good, as long as the nuclear structures, that form the lattice points, are sufficiently widely spaced. In these studies, the authors considered the formation of pasta structures both at zero and finite temperature.

Let us point out that when describing warm neutron star matter, besides these heavy clusters, light clusters, like e.g. deuterons, tritiums, heliums and $\alpha-$particles, can also form [Hempel et al., 2011, Avancini et al., 2012, Pais et al., 2015]. According to some estimates, the nuclear pasta phase may form up to 20% of the supernova matter at bounce [Sonoda et al., 2007]. This justifies the importance of considering these exotic geometries in the EoS used in core-collapse supernova simulations. However, at finite temperature, it becomes questionable whether the single heavy nucleus approximation, which has been applied in [Shen et al., 1998, Avancini et al., 2010] is still valid, or if it is in fact too schematic. Alternative EoS, appropriate for core-collapse supernova simulations, as the ones proposed in [Hempel and Schaffner-Bielich, 2010, Raduta and Gulminelli, 2010] were built, considering statistical methods that overcome the single nucleus approximation.

1.2 Liquid gas phase transition

Nuclear matter at subsaturation densities is characterized by a liquid-gas phase transition [Müller and Serot, 1995]. For a system of a liquid (phase 1) and a gas (phase 2) in equilibrium, the temperatures of both phases, T_1 and T_2, and the correspondent pressures, P_1, P_2, must be equal, since the forces exerted by the two phases on each other at their surface of contact must be equal and opposite [Landau and Lifshitz, 1980]. The same applies to the chemical potentials, $\mu_1 = \mu_2$. If the potentials are expressed as functions of the pressure and temperature, and $T_1 = T_2 = T$ and $P_1 = P_2 = P$, then $\mu_1(P,T) = \mu_2(P,T)$. These thermal, mechanical and chemical equilibrium relations are called the Gibbs conditions.

Since nuclear matter is formed by two different types of particles, protons and neutrons, mechanical and chemical instabilities may lead

both to the fragmentation of a nuclear system in heavy ion collisions and an isospin distillation effect [Colonna et al., 2002, Chomaz et al., 2004]. The distillation effect is defined as the tendency of the system to separate into two phases with a different isospin content from the average isospin content that the unstable homogeneous phase would have. Due to the symmetry energy contribution to the total energy of the system, the most favorable phase separation will correspond to an isospin-symmetric matter dense phase (liquid), and a neutron-rich gas, i.e. a highly isospin-asymmetric phase.

Dynamical and thermodynamical instabilities of nuclear and stellar matter at subsaturation densities are particularly important for the description of the inner crust of neutron stars [Providência et al., 2006a, Brito et al., 2006]. The thermodynamic spinodal is defined as the locus where the free energy curvature goes to zero, and the dynamic spinodal as the surface where the eigenmodes of matter go to zero. Both surfaces coincide if perturbations of infinite wave length are considered in the dynamical description. Spinodal decomposition has been applied to study the fragmentation of finite nuclear systems, within a self-consistent quantum approach, in Refs. [Colonna et al., 2002, Chomaz et al., 2004], and it was shown that the liquid-gas phase transition of asymmetric systems would induce a fractional distillation of the system.

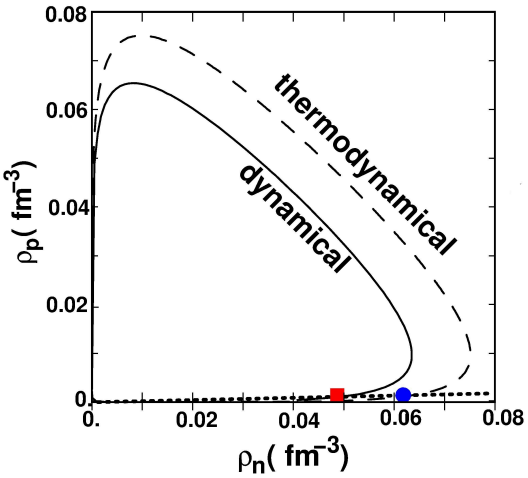

Figure 1.3: Dynamical and thermodynamical instabilities. The transition densities are shown for β-equilibrium matter by square and dot points.

From the spinodals of both neutron-proton (np) and neutron-proton-

electron (npe) matter, it is possible to make a relatively good prediction of the density and pressure at the crust-core phase transition, see Fig. 1.3 [Providência, 2007, Pais et al., 2009, Santos et al., 2008, Ducoin et al., 2008]. In Ref. [Link et al., 1999], quantities such as the transition pressure and density, which determine the extension of the crust, allowed the understanding of the formation of glitches, sudden changes in the star's rotation, and an important relation between the EoS and neutron star observations was established.

1.3 The crust-core transition

The crust-core transition is the transition from the clusterized matter in the inner crust to the homogeneous matter in the core. Different nuclear models have been used to study the properties of this transition in neutron stars, and to contribute to the interpretation of astrophysical observations.

For a given nuclear density, the proton fraction of homogeneous β-equilibrium neutron-star matter, transparent to neutrinos, is essentially determined by the symmetry energy, and it has been shown that the symmetry energy slope, L, correlates to the crust-core transition properties [Ducoin et al., 2010], see Fig. 1.4 taken from [Vidaña et al., 2009]: the larger the value of L, the smaller the transition density. It is, however, important to account for misleading relations when the study is limited to a restricted nuclear model or family of models. In Refs. [Vidaña et al., 2009, Ducoin et al., 2010, Ducoin et al., 2011], it is shown that an accurate determination of the symmetry energy and its slope and curvature at subsaturation densities allows a quite accurate prediction of the core-crust transition properties.

The correlation between L and the transition density was shown to be very robust, and it emerges from the following properties: a larger value of L means a smaller symmetry energy at subsaturation density, which implies a lower density ρ_t. On the other hand, no clear correlation was observed between L and the transition pressure when different kinds of models are used. The transition pressure depends on the nuclear models, and different models may even predict contradictory increasing or decreasing correlations of $P_{\rm t}$ with L [Ducoin et al., 2011].

The crust-core transition can be determined by the crossing between the dynamical spinodal and the EoS of β-equilibrium matter, with results very similar to the Thomas-Fermi prediction from pasta phase calculations [Avancini et al., 2010, Grill et al., 2012]. The transition

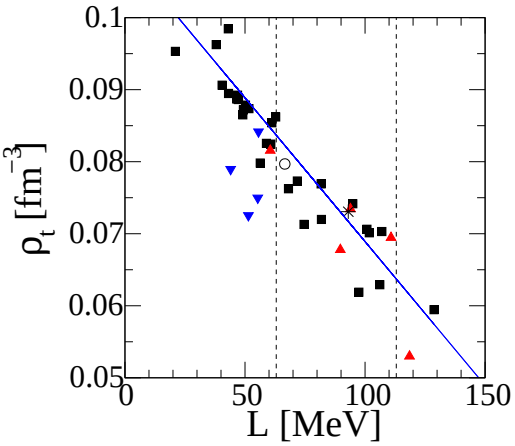

Figure 1.4: Correlation between the symmetry energy slope L and the crust-core transition density, ρ_t, taken from Ref. [Vidaña et al., 2009]. The transition density is shown for a wide number of nuclear models, in particular, phenomenological approaches: non-relativistic Skyrme forces (black squares), relativistic mean-field (RMF) models (blue triangles for NLWM and red triangles for DDH), QMC (stars), and the microscopic BHF calculation with Argonne V18 potential with a three-body force of the Urbana type (circle). The blue line is a linear fit.

point calculated on the basis of the thermodynamical spinodal is larger than the prediction coming from the dynamical spinodal [see Fig. 1.3] and Thomas-Fermi pasta calculation, however, it was confirmed that the correlations obtained within the thermodynamical approach are equivalent to the ones obtained from the dynamical spinodal approach [Ducoin et al., 2011]

1.4 Collective modes

Collective modes of nuclear matter have been studied with the help of different formalisms. A non-relativistic approach was applied in [Haensel, 1978] to calculate isospin and density waves in asymmetric nuclear matter. The relativistic Vlasov equation, a semi-classical approach to the quantum hydrodynamical (QHD) model was used [Nielsen et al., 1991, Nielsen et al., 1994, Nielsen et al., 1993]. The relativistic Vlasov equation based on QHD was also applied to the simulation of heavy-ion collisions [Ko et al., 1987, Jin et al., 1989], and its predictions are similar to the ones obtained from more time consuming calculation-

s, based on the time-dependent Dirac equations [Ko et al., 1987]. These results indicate that the relativistic Vlasov equation defines an alternative way to study relativistic systems.

In Ref. [Lim and Horowitz, 1989], the zero sound, and the longitudinal and transverse modes of symmetric nuclear matter were investigated within a relativistic Hartree calculation. Later, the authors of Ref. [Greco et al., 2003] calculated the eigenmodes of asymmetric nuclear matter within a relativistic approach to nuclear matter via the linear response equations. Matsui studied the collective modes in a Landau Fermi liquid formalism, applied to the relativistic mean field theory, see [Matsui, 1981], but the nuclear model considered did not include non-linear terms, missing, therefore, some of the properties of nuclear matter at saturation. In his work, only symmetric matter and neutron matter were discussed. Later, in Ref. [Avancini et al., 2005], the longitudinal collective modes of asymmetric nuclear matter were calculated, within the relativistic Vlasov equation. In this thesis, this is the formalism that we are going to generalize to magnetized nuclear matter. Recently, the authors of [Pais et al., 2016] have shown that the Relativistic Random Phase Approximation and the Vlasov equation predict similar transition densities for npe β-equilibrium stellar matter, showing again the equivalence between these two methods.

The collective modes of nuclear matter may influence in a drastic way the opacity of neutrinos formed during the supernova explosion for subsaturation densities. The presence of spin domains could give rise to coherent effects, which would increase the cross section of neutrinos with a typical energy of a few MeV. These effects are expected for densities of the order of $10 - 50\%$ of the saturation density, i.e., inside the inner crust [Avancini et al., 2005].

Actually, the transport properties of stellar matter depend on the modes which can be excited in the medium, either by its own free constituents (proton, neutron or electron scattering) or by escaping neutrinos. In the case of a nonhomogeneous medium, a possible interaction could consist in exciting a resonance mode inside a cluster. A nuclear nonuniform system is specific to the structure of the inner crust of neutron stars, and their collective modes may influence significantly the specific heat of baryonic inner crust matter of neutron stars [Khan et al., 2005].

Di Gallo et al. [Gallo et al., 2011] have studied the spectrum of collective excitations in the "lasagna" phase in the neutron star inner crust within a superfluid hydrodynamics approach. In particular, they have obtained very low-energy collective modes, and discussed their

contribution to the specific heat in comparison with other known contributions. The boundary conditions used were not totally justified. However, an improved model was discussed recently in [Urban and Oertel, 2015].

1.5 Constraints on the EoS

The EoS of nuclear matter must be constrained by experimental data and astrophysical observations. In this study, we consider models within the RMF approach. These are phenomenological models, whose parameters, as referred before, must be fitted to data, either experimental, observational, or even theoretical data, obtained from first principles. Some of the constraints to be considered are the astrophysical constraints on the maximum neutron star mass and the speed of sound in stellar matter: $M_{\rm max} \geq 2\,M_\odot$, a limit set by the mass of the pulsar PSR J0348+0432 ($2.01 \pm 0.04 M_\odot$) [Antoniadis et al., 2013], and $v_{\rm sound}(2\,M_\odot) < c$, i.e., causality. RMF models satisfy automatically the second one. We will consider the NL3 or NL3$\omega\rho$ models that also satisfy the first one.

Besides these two constraints, several much stronger nuclear constraints have been obtained during the last decade, either from experiments or from microscopic calculations.

The parameters of the models are usually obtained either by making a fit to the saturation properties of nuclear matter or by performing a multi-parameter fitting procedure to the properties of a set of spherical nuclei. The experimental inputs for finite nuclei are the charge radii, the total binding energies, the neutron radii or the surface thickness [Lalazissis et al., 1997].

Making the incompressibility K, the symmetry energy at saturation J and its slope L, consistent with the semi-empirical evaluations of these parameters obtained in the laboratory, yields constraints on the corresponding EoS of neutron star, and consequently, on neutron star models. In particular, the radius of the star has been shown to be correlated with L, especially for low mass stars [Carriere and C. J. Horowitz, 2003]. The correlation is still present for the more massive stars, but it becomes weaker with the mass.

In [Khan et al., 2012], it was shown that self-consistent microscopic calculations generate a reliable incompressibility constraint $K = 230 \pm 40$ MeV for infinite nuclear matter, where 40 MeV corresponds to the 17% uncertainty in the extrapolations from the average nuclear density

Table 1.1: Nuclear matter saturation properties of NL3 and NL3$\omega\rho$ models.

Model	ρ_0 (fm^{-3})	E_B (MeV)	K (MeV)	J (MeV)	L (MeV)
NL3	0.148	-16.240	269.937	37.344	118.320
NL3$\omega\rho$,$\Lambda_v = 0.01$	0.148	-16.240	269.937	34.929	87.638
NL3$\omega\rho$,$\Lambda_v = 0.02$	0.148	-16.240	269.937	33.121	68.147
NL3$\omega\rho$,$\Lambda_v = 0.03$	0.148	-16.240	269.937	31.660	55.227

to the saturation density. Both NL3 and NL3$\omega\rho$ models satisfy this constraint, if the uncertainty is considered to be 18%, instead of 17%.

Within the theoretical calculations, we refer the studies of neutron matter performed in [Gandolfi et al., 2012] and [Hebeler et al., 2013]. In Ref. [Gandolfi et al., 2012], the authors calculate the EoS of neutron matter with phenomenological NN interaction, which provides an accurate description of nucleon-nucleon scattering data at low energies and 3N interaction, using quantum Monte Carlo techniques. In [Hebeler et al., 2013], the equation of state of neutron-rich matter has been determined within a microscopic approach in the framework of chiral effective field theory. NL3 does not satisfy the constraints from the calculation of [Hebeler et al., 2013]. We will, however, consider it, because it is frequently used as a reference. On the other hand, the NL3$\omega\rho$ model only shows a 10% relative deviation from the results presented in [Hebeler et al., 2013], which we consider acceptable.

Two recent publications, [Tsang et al., 2009] and [Lattimer and Lim, 2013], have collected a set of experimental constraints on the $J - L$ plane. According to [Tsang et al., 2009] ([Lattimer and Lim, 2013]) these quantities satisfy $30 < J < 35$ MeV and $30 < L < 80$ MeV ($29.0 < J < 32.7$ MeV and $40.5 < L < 61.9$ MeV). The values of J and L for NL3$\omega\rho$ belong to these intervals, but NL3 does not satisfy these conditions.

Table 1.1 shows the nuclear matter properties at saturation density for these two models: the binding energy per nucleon E_B, the incompressibility coefficient K, the symmetry energy J, and the symmetry energy slope L.

1.6 Magnetars

More and more evidences are showing that there is a class of neutron stars with strong magnetic fields [Harding and Lai, 2006]. The discovery of radio pulsars [Hewish et al., 1968] with magnetic fields lying between 10^{11} and 10^{14} G is one evidence for such objects. The strongly magnetized neutron stars, which were discovered at x-ray and γ-ray energies, and have very strong surface magnetic fields of the order of $10^{14} - 10^{15}$ G, are other class of objects with very strong magnetic fields [Braithwaite and Spruit, 2006]. Such stars are known as magnetars [Duncan and Thompson, 1992]. These stars are bright pulsating isolated neutron stars with relatively long periods, usually lasting for several seconds [Condon and Ransom, 2016]. Soft γ-ray repeaters, which emit powerful bursts of γ- and x-rays at irregular intervals, and anomalous x-ray pulsars, are considered in the literature the two main types of magnetars [Turolla et al., 2015].

The strongest surface magnetic field observed up to now is as large as 2×10^{15} G [SGR Catalogue, 2009], and it was detected from a quite young star, SGR 1806-20 [Olausen and Kaspi, 2014, SGR Catalogue, 2009]. One believes that in the interior of the stars, the fields could be higher, reaching the order of 10^{18} G, according to the virial theorem [Lai and Shapiro, 1991], but these are only assumptions. The integration of the Einstein equations, taking into account the magnetic field, and performed in [Broderick et al., 2002], seems to indicate that, in fact, neutron stars become unstable for magnetic fields above $\sim 10^{18}$ G.

The equation of state of stellar matter under $\beta-$equilibrium, charge neutrality conditions, and strong magnetic fields, has been studied by several authors [Chakrabarty et al., 1997, Broderick et al., 2000]. It was shown that the nucleon anomalous magnetic moment (AMM) plays a significant role only for sufficiently strong fields, and may decrease the softening of the EoS caused by the Landau quantization. Other theoretical studies on the effects of strong magnetic fields on dense stellar matter, that forms neutron stars, have been carried out by many authors [Cardall et al., 2001, Yue and Shen, 2006].

One can determine the intensity of the magnetic fields of these stars from the period, P, and period derivative, $\dot{P}$, of the objects, which are measured from the arriving time of the pulses, and the assumption that the spin-down is due to the usual magnetic dipole radiation. The

surface field intensity can then be calculated from the expression

$$B = \left(\frac{3Ic^3 P\dot{P}}{2\pi R^6} \right)^{1/2}, \tag{1.1}$$

where I and R are the moment of inertia and radius of the star, respectively. Fig. 1.5 is a $P\dot{P}$ diagram, useful to track the lives of pulsars, playing a similar role to the Hertzsprung-Russell diagram for ordinary stars.

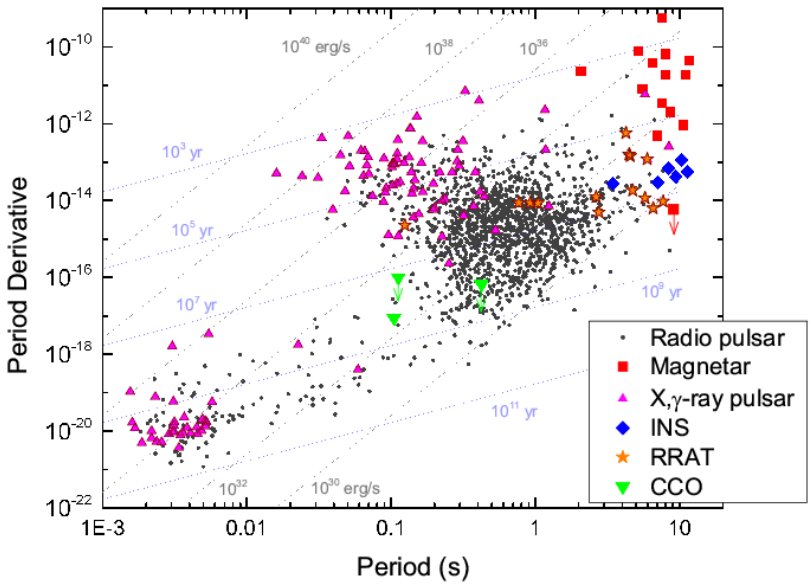

Figure 1.5: $P\dot{P}$ diagram for the known magnetars and other objects. Objects with a large magnetic field lie on the top right corner. Figure taken from [Harding, 2013].

Magnetic fields significantly affect the radiative spectral opacities and determine various observational manifestations of the neutron stars. They also directly affect other processes, such as the thermal evolution of the crust, since the temperature modifies the magnetic filed evolution. Some theoretical models of pulsar and magnetar magnetospheres depend on the properties of nuclear matter under strong magnetic fields. Moreover, strong magnetic fields will also greatly influence the transport properties and thermal structure of the neutron star crust. Even though the magnetic quantization effects are small in

the crust, the magnetic field still significantly modifies the transport coefficients (e.g. electric conductivity and heat conductivity).

Previously, there have already been studies that analyze the effect of the magnetic field on the thermodynamical spinodal [Rabhi et al., 2008], and the pasta phases in the inner crust [Lima et al., 2013]. Both studies, however, have been performed for magnetic fields more intense than the ones expected to exist in the crust of a magnetar. A more careful study, considering realistic magnetic field intensities, should be carried out.

The effect of the magnetic field on the outer crust was analyzed in Ref. [Chamel, 2012], within a Hartree-Fock-Bogoliubov calculation, and it was shown that the Landau quantization of the electron motion could affect the outer crust equation of state, giving rise to more massive outer crusts than the expected in usual neutron stars. Also, the neutron drip density and pressure are affected by a strong magnetic field, showing typical quantum oscillations, which shift the transition outer-inner crust to larger or smaller densities [Chamel et al., 2015], according to the field intensity.

Recently, the time evolution of the magnetic field of isolated x-ray pulsars has been studied by Pons et al. [Pons et al., 2013]. The authors have shown that a fast decay of the magnetic field could explain the non observation of stars with periods above 12 s. The decay of the magnetic field was attributed to a high electrical resistivity of the inner crust, possibly due to the existence of an amorphous and heterogeneous layer at the bottom of the inner crust. The lack of isolated x-ray pulsars with a period higher than 12 s, could, therefore, be a direct indication of the existence of an amorphous inner crust, possibly in the form of pasta phases.

However, very strong magnetic fields will influence the proton charge fluctuations, and correspondingly the transport properties. Molecular dynamics simulations of the nuclear pasta have shown that topological defects in the pasta could increase electron scattering and reduce the electrical and the thermal conductivities [Horowitz et al., 2015, Schneider et al., 2016]. However, electron conductivity in magnetized neutron star matter was also studied in [Yakovlev, 2015], and it was shown that the electron transport is strongly anisotropic, due to the presence of strong magnetic fields. The complexity introduced by the magnetic field suggests that both suppression and enhancement of the electron conduction in the presence of the pasta phases are possible. In the inner crust, the resistivity is determined by electron-impurity scattering at low temperatures.

1.7 Objectives

Our main objective is to study the effect of strong magnetic fields, as the ones that may occur inside magnetars, on the extension of the crust. Using the RMF framework and nuclear models with saturation properties in the range of values presently accepted as reasonable coming from laboratory experiments, theoretical calculations or observations, we will apply:

1) the semiclassical relativistic approach based on the Vlasov equation to study infinite symmetric and asymmetric nuclear matter at zero temperature, and determine the dispersion relation of the respective collective modes. Within the same approach the dynamical spinodal will be used to determine the effect of the magnetic field on the crust-core transition, on the average size of the clusters at $T = 0$ and on the ratio between the proton and neutron density fluctuations. We will restrict ourselves to the longitudinal modes arising from small oscillations around a stationary state in asymmetric nuclear matter at subsaturation densities [Nielsen et al., 1991, Providência et al., 2006a, Brito et al., 2006].

2) the thermodynamical approach to the description of instabilities to the discuss the joint effect of the magnetic field and the temperature on the crust-core transition. This will be carried out calculating the thermodynamical spinodal at zero and finite temperature under strong magnetic fields. At $T = 0$, the thermodynamic transition densities will be compared with the predictions obtained from the dynamical spinodal calculation, both excluding and including the anomalous magnetic moment of protons and neutrons. The finite temperature thermodynamical spinodal will be applied to study the evolution of the crust extension as the temperature increases, for different values of the magnetic field. Special attention will be given to the determination of the conditions that wash out the magnetic field effects.

Chapter 2

Relativistic mean field models

2.1 Mean field approximation

The nuclear force binds together the protons and neutrons in the nucleus. It favours the binding of nucleons with opposite spins, and it is a very short-range force, with range 1 fm$=10^{-15}$ m [Brown and Jackson, 1976, Machleidt and Slaus, 2001], much stronger than the electrical force. It has a particular property: a nucleon can only interact with the ones in its immediate vicinity. This is called saturation [Sakuragi, 2016], and leads to a nearly constant nuclear binding energy and density. Nowadays, the correct description of this force is still lacking. The nuclear many-body problem can not be solved exactly and the scientific community still relies on approximate approaches [Ring and Schuck, 1980]. A better understanding of neutron stars, as they can be considered giant nuclei, can bring some hints into this problem.

Phenomenological and microscopic approaches have been applied to the study of nuclear matter. A phenomenological approach [Li et al., 2008] introduces parameters that have to be fitted to observables of finite nuclei and should reproduce the saturation properties of symmetric nuclear matter. One problem with such a method is the fact that the parametrizations are not unique, leaving us with the need of finding constrains, e.g. from observations and from microscopic neutron matter calculations, to restrain these number of sets.

An example of such an approximation is given by the relativistic mean field models [Walecka, 1974]. In these type of models, the mesons are responsible for mediating the nuclear force between the nucleons. It is based on field-theoretical techniques, where the nucleons are treated as Dirac particles (relativistic) moving in meson fields.

The meson masses and the couplings constants between the mesons and the nucleons are the model parameters, and are fitted to finite nuclei properties, see the recent compilation [Dutra et al., 2014]. However, the pioneer phenomenological nuclear models were the non-relativistic models, based on the Skyrme force [Skyrme, 1956, Köhler, 1965a, Köhler, 1965b, Brink and Boeker, 1967]. Presently, there are several non-relativistic phenomenological nuclear models, appropriate to describe nuclear stellar matter, including the Lyon parametrizations, such as SLy4 [Chabanat et al., 1998], and the Bruxelles parametrizations [Goriely et al., 2010, Goriely et al., 2013]. When these parametrizations are used, it is important to verify that the EoS does not become acausal within the range of densities of interest, see [Dutra et al., 2012] for a recent review.

2.2 The equation of state

The EoS of stellar matter is the starting point to discuss the instabilities that occur at subsaturation densities. We will work within the RMF framework, and, in the following, we briefly review the formalism.

2.2.1 The $\sigma - \omega$ model

In order to determine the EoS of our research system, we start from the σ-ω model, known as Walecka model [Serot and Walecka, 1995, Ring, 1996]. In this model, the nucleons interact through the exchange of mesons σ and ω. The σ meson has a strong attractive force at intermediate range, and the ω meson has a strong repulsive force at short range. The Lagrangian density is written by

$$\begin{aligned}\mathcal{L} &= \sum_{i=p,n} \bar{\psi}_i \left[\gamma_\mu i(\partial^\mu + i g_v V^\mu) - M_i^*\right] \psi_i + \frac{1}{2}\left(\partial_\mu\phi\partial^\mu\phi - m_s^2\phi^2\right) - \frac{1}{4}\Omega_{\mu\nu}\Omega^{\mu\nu} \\ &+ \frac{1}{2}m_v^2 V_\mu V^\mu, \end{aligned} \tag{2.1}$$

where $M_i^* = m - g_s\phi$, $\Omega_{\mu\nu} = \partial_\mu V_\nu - \partial_\nu V_\mu$.

The equations of motion for the protons, neutrons, and meson fields are derived from the Euler-Lagrange equations [Providência, 2007]:

$$\left[\gamma_\mu(i\partial^\mu - g_v V^\mu) - (m - g_s\phi)\right]\psi_i = 0, \tag{2.2}$$

$$(\Box + m_s^2)\phi = g_s\rho_s, \tag{2.3}$$

$$(\Box + m_v^2)V^\nu = g_v j^\nu, \tag{2.4}$$

where $\rho_s = \sum \bar{\psi}_i\psi_i$ is the scalar density, and $j^\nu = \sum \bar{\psi}_i\gamma_\mu\psi_i$ is the baryonic current density.

Using the RMF approximation, the meson fields are replaced by their mean expected values, and the three nonlinear differential equations above are solvable [Glendenning, 2000]. The energy spectra for nucleons can be worked out, and is given by

$$\varepsilon(\mathbf{p}) = \sqrt{(\mathbf{p} - g_v\mathbf{V})^2 + (m - g_s\phi)^2} + g_v V_0. \tag{2.5}$$

For static homogeneous nuclear matter, the energy density has the expression

$$\varepsilon = \int \frac{d^3p}{2\pi^3} h(\mathbf{p},t) f(\mathbf{p},t) + \frac{1}{2}(m_s^2\phi^2 - m_v^2 V_0^2), \tag{2.6}$$

where $h(\mathbf{p},t) = \sqrt{(\mathbf{p})^2 + (m - g_s\phi)^2} + g_v V_0$, is the one-particle hamiltonian.

Within the Thomas-Fermi approximation, the ground-state property is calculated by minimizing the free energy density [Providência, 2007],

$$\delta F = \delta(\varepsilon - \mu\rho)\,. \tag{2.7}$$

In this way, we get the energy density of nuclear matter

$$\varepsilon = \frac{1}{\pi^2}\int_0^{P_f} \sqrt{\mathbf{p}^2 + (m - g_s\phi)^2}\, p^2 dp + \frac{1}{2}m_s^2\phi^2 + \frac{1}{2}m_v^2 V_0^2. \tag{2.8}$$

The expression for the pressure is given by [Lay, 2012]

$$P = \frac{1}{3\pi^2}\int_0^{P_f} \frac{p^4}{\sqrt{\mathbf{p}^2 + (m - g_s\phi)^2}} dp - \frac{1}{2}m_s^2\phi^2 + \frac{1}{2}m_v^2 V_0^2. \tag{2.9}$$

This quantities define the EoS of nuclear matter within the $\sigma - \omega$ model, which, although describing the main features of the nuclear force, fails to reproduce some of the main properties of symmetric nuclear matter at saturation.

2.2.2 Generalizing the $\sigma - \omega$ model

In the original σ-ω model, the meson masses and coupling constants are adjusted to nuclear matter and properties of nuclei. The energy

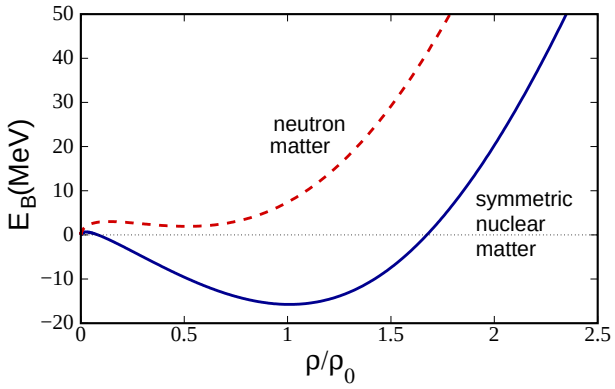

Figure 2.1: Energy per particle for symmetric nuclear matter and neutron matter. The EoS of neutron matter presents a minimum at $\sim 0.6\rho_0$ that is considered unphysical.

per nucleon is -15.75 MeV and the Fermi momentum at saturation is $P_F = 1.42$ fm^{-1}. The model is appropriate to describe dense stellar matter, and the ratio between the pressure and the energy density is always less than 1, i.e. the EoS is always causal. Furthermore, it automatically includes a strong spin-orbit contribution for the nuclear force [Ring, 1996]. However, the model has several limitations, namely, a very low effective mass $M^* = 0.54m$, the existence of a minimum at finite density in the neutron matter EoS, a too large incompressibility $K = 540$ MeV, and a too small symmetry energy $J = 22.1$ MeV.

Several improvements were implemented to the σ-ω model in the last three decades, in order to better describe the nuclei and nuclear matter, see [Boguta and Bodmer, 1977,Lalazissis et al., 1997,Sumiyoshi et al., 1995]. One of the main problems was the wrong description of asymmetric nuclear matter, with neutron matter presenting a finite saturation density, see Fig. 2.1. This is overcome by including the vector-isovector ρ meson in the Lagrangian density to describe the isospin channel [Serot and Walecka, 1995],

$$\mathcal{L}_\rho = -\frac{1}{4}\mathbf{B}_{\mu\nu}\cdot\mathbf{B}^{\mu\nu} + \frac{1}{2}m_\rho^2\mathbf{b}_\mu\cdot\mathbf{b}^\mu\,, \tag{2.10}$$

with

$$\mathbf{B}^{\mu\nu} = \partial_\mu\mathbf{b}^\nu - \partial_\nu\mathbf{b}^\mu - g_\rho(\mathbf{b}^\mu\times\mathbf{b}^\nu).$$

In order to get a better description for the ground-state of stable and unstable nuclei, the self-interaction terms for the scalar meson

proposed in [Boguta and Bodmer, 1977] have been included in the NL3 parametrization [Lalazissis et al., 1997],

$$\mathcal{L}_{NL3} = \frac{1}{3!}\kappa\phi^3 + \frac{1}{4!}\lambda\phi^4. \tag{2.11}$$

Another improvement is achieved by including the nonlinear ω-ρ term [Horowitz and Piekarewicz, 2001a], as in the NL3$\omega\rho$ model, which mixes the ω and ρ mesons, allowing to soften the density dependence of the symmetry energy above saturation density,

$$\mathcal{L}_{\omega\rho} = \Lambda_v g_v^2 g_\rho^2 V_\mu V^\mu \mathbf{b}_\mu \cdot \mathbf{b}^\mu. \tag{2.12}$$

Changing the magnitude of the nonlinear ω-ρ term has a direct effect on the neutron skin thickness of nuclei, and on the radius of neutron stars. If the scheduled experiments PREX and CREX [Horowitz et al., 2001, Kumar et al.,], to measure the neutron skins of ^{208}Pb and ^{48}Ca with high precision, will be successful, important constraints on the EoS will be obtained.

To describe stellar matter, it is necessary to include the contributions of electrons and the electromagnetic interaction [Providência, 2007],

$$\mathcal{L}_e = \bar{\psi}_e \left[\gamma_\mu \left(i\partial^\mu + eA^\mu\right) - m_e\right] \psi_e, \tag{2.13}$$

$$\mathcal{L}_A = -\frac{1}{4} F_{\mu\nu} F^{\mu\nu}. \tag{2.14}$$

Now, the complete Lagrangian density in Eq. (2.1) becomes:

$$\mathcal{L} = \sum_{i=p,n} \mathcal{L}_i + \mathcal{L}_e + \mathcal{L}_\sigma + \mathcal{L}_\omega + \mathcal{L}_\rho + \mathcal{L}_{\omega\rho} + \mathcal{L}_A, \tag{2.15}$$

where,

$$\mathcal{L}_i = \bar{\psi}_i \left[\gamma_\mu i D^\mu - M_i^*\right] \psi_i, \tag{2.16}$$

with

$$iD^\mu = i\partial^\mu - g_v V^\mu - \frac{g_\rho}{2}\boldsymbol{\tau}\cdot\mathbf{b}^\mu - eA^\mu \frac{1+\tau_3}{2}, \tag{2.17}$$

and

$$\mathcal{L}_\sigma = \frac{1}{2}\left(\partial_\mu\phi\partial^\mu\phi - m_s^2\phi^2 - \frac{1}{3}\kappa\phi^3 - \frac{1}{12}\lambda\phi^4\right), \tag{2.18}$$

$$\mathcal{L}_\omega = -\frac{1}{4}\Omega_{\mu\nu}\Omega^{\mu\nu} + \frac{1}{2}m_v^2 V_\mu V^\mu. \tag{2.19}$$

In this system, nucleons with mass M interact with and through an isoscalar-scalar field ϕ with mass m_s, an isoscalar-vector field V^μ with mass m_v, and an isovector-vector field $\mathbf{b}^\mu$ with mass m_ρ. Besides nucleons, electrons with mass m_e is included in the Lagrangian density. Protons and electrons interact through the electromagnetic field A^μ.

2.2.3 Adjusting the parameters

We will be using the NL3 and NL3$\omega\rho$ models in the present study.

The NL3 model has been fitted to reproduce the ground state of a wide number of stable and unstable nuclei, and it is still used very frequently [Lalazissis et al., 1997]. We can take it as a representation of the models with a hard EoS in both the isoscalar and the isovector channels, although we are aware of its limitations: it reproduces nuclear properties with a minimum of non-linear meson terms in the Lagrangian; it has a large symmetry energy slope and incompressibility at saturation. The symmetry energy slope of NL3 at saturation is 118 MeV, slightly larger than the limit obtained from the experimental constraints with isospin diffusion $63 < L < 113$ MeV, and larger than other constraints from heavy-ion collisions [Centelles et al., 2009]; the EoS obtained within NL3 is quite hard, and larger than the limits that collective flow data [Danielewicz et al., 2002] impose to the EoS of symmetric matter.

NL3$\omega\rho$, on the other hand, includes a mixed isoscalar-isovector term, which is varied to change the density dependence of the symmetry energy [Horowitz and Piekarewicz, 2001a], and it shows a softer behavior of the symmetry energy, which becomes softer when the coupling Λ_v increases.

The energy per particle is written as a function of the nucleon density ρ and the asymmetry parameter $\delta = (\rho_p - \rho_n)/\rho$,

$$E_B(\rho, \delta) = E_B(\rho, 0) + J\delta^2 \tag{2.20}$$

where $E_B(\rho, 0)$ is the energy per particle of symmetric matter and J is the bulk symmetry energy, which is given by

$$J = \frac{1}{2}\frac{\partial^2 E_B(\rho, \delta)}{\partial \delta^2}|_{\delta=0}. \tag{2.21}$$

In the RMF approximation, the symmetry energy becomes

$$J = \frac{P_F^2}{6\epsilon_F} + \frac{\rho}{2}\frac{g_\rho^2}{4m_\rho^{*2}}, \tag{2.22}$$

with $\epsilon_F = \sqrt{P_F^2 + M^{*2}}$, and $m_\rho^* = \sqrt{m_\rho^2 + 2g_\rho^2\Lambda_v V_0^2}$ is the effective ρ-meson mass. The inclusion of the non-linear term $\omega - \rho$ affects the symmetry energy.

Both NL3 and NL3$\omega\rho$ show a decrease in the transition density when L increases. This is due to the decrease of the transition proton fraction. A larger L corresponds to a smaller symmetry energy at

subsaturation densities, and allows a larger asymmetry. Choosing a model with a softer symmetry energy, namely a smaller slope L at saturation, would shift the crust-core transition to a larger density and increase the proton fraction [Ducoin et al., 2011].

Above the critical temperature, where the models do not present instabilities [Brito et al., 2006], no clusters are expected, and there is a smooth transition from a gas to a liquid phase in this region. Both NL3 and NL3$\omega\rho$ have the same isoscalar description. The critical temperature is totally determined by the isoscalar properties of the models, not the isovector properties. Therefore, the critical temperatures for NL3 and NL3 $\omega\rho$ are the same [Alam et al., 2017].

2.3 Equation of state of magnetized nuclear matter

In our work, stellar matter is described within the nuclear RMF formalism under the effect of strong magnetic fields [Broderick et al., 2000, Rabhi et al., 2008], including the effect of the AMM. The static electromagnetic field $A^{\mu}_{stat} = (0, 0, Bx, 0)$ is included, so that $\mathbf{B}{=}B\,\hat{\mathbf{z}}$ and $\nabla{\cdot}\mathbf{A} = 0$. It is assumed to be externally generated, and only frozen-field configurations are considered for this component.

The Lagrangian density, with $c = \hbar = 1$, reads

$$\mathcal{L} = \sum_{i=p,n} \mathcal{L}_i + \mathcal{L}_e + \mathcal{L}_\sigma + \mathcal{L}_\omega + \mathcal{L}_\rho + \mathcal{L}_{\omega\rho} + \mathcal{L}_{\mathcal{A}}, \tag{2.23}$$

where $\mathcal{L}_i$ is the nucleon Lagrangian density, given by

$$\mathcal{L}_i = \bar{\psi}_i \left[\gamma_\mu i D^\mu - M_i^* - \frac{1}{2}\mu_N \kappa_b \sigma_{\mu\nu} F^{\mu\nu} \right] \psi_i, \tag{2.24}$$

with

$$iD^\mu = i\partial^\mu - g_v V^\mu - \frac{g_\rho}{2}\boldsymbol{\tau}\cdot\mathbf{b}^\mu - eA^\mu\frac{1+\tau_3}{2},$$

and

$$\mathcal{L}_e = \bar{\psi}_e \left[\gamma_\mu \left(i\partial^\mu + eA^\mu\right) - m_e\right] \psi_e, \tag{2.25}$$

$$\mathcal{L}_\sigma = \frac{1}{2}\left(\partial_\mu\phi\partial^\mu\phi - m_s^2\phi^2 - \frac{1}{3}\kappa\phi^3 - \frac{1}{12}\lambda\phi^4\right), \tag{2.26}$$

$$\mathcal{L}_\omega = -\frac{1}{4}\Omega_{\mu\nu}\Omega^{\mu\nu} + \frac{1}{2}m_v^2 V_\mu V^\mu, \tag{2.27}$$

$$\mathcal{L}_\rho = -\frac{1}{4}\mathbf{B}_{\mu\nu}\cdot\mathbf{B}^{\mu\nu} + \frac{1}{2}m_\rho^2\mathbf{b}_\mu\cdot\mathbf{b}^\mu, \tag{2.28}$$

$$\mathcal{L}_{\omega\rho} = \Lambda_v g_v^2 g_\rho^2 V_\mu V^\mu \mathbf{b}_\mu\cdot\mathbf{b}^\mu, \tag{2.29}$$

$$\mathcal{L}_A = -\frac{1}{4}F_{\mu\nu}F^{\mu\nu}, \tag{2.30}$$

where $\Omega_{\mu\nu} = \partial_\mu V_\nu - \partial_\nu V_\mu, \mathbf{B}_{\mu\nu} = \partial_\mu\mathbf{b}_\nu - \partial_\nu\mathbf{b}_\mu - g_\rho(\mathbf{b}_\mu\times\mathbf{b}_\nu)$ and $F_{\mu\nu} = \partial_\mu A_\nu - \partial_\nu A_\mu$.

We use the NL3 [Lalazissis et al., 1997], and NL3$\omega\rho$ [Horowitz and Piekarewicz, 2001b, Horowitz and Piekarewicz, 2001a] parametrizations, which describe two solar mass stars [Fortin et al., 2016]. For the NL3 model, we need the following parameters: the nucleon mass M, the electrons mass m_e, the masses of the mesons m_s, m_v, m_ρ, three coupling constants g_s, g_v and g_ρ of the mesons to the nucleons, the electromagnetic coupling constant $e = \sqrt{4\pi/137}$, the self-interacting coupling constants κ and λ, the isospin projection $\tau_3 = \pm 1$ for the protons and neutrons, respectively. For NL3$\omega\rho$ model, we also have $\omega\rho$ coupling Λ_v besides these.

Some of the saturation properties of NL3$\omega\rho$ are: the binding energy, $E_B = -16.2$ MeV, the saturation density, $\rho_0 = 0.148$ fm^{-3}, the incompressibility, $K = 272$ MeV, the symmetry energy, $J = 31.7$ MeV, and its slope, $L = 55.5$ MeV. The model satisfies the constraints imposed by microscopic calculations of neutron matter [Hebeler et al., 2013, Gandolfi et al., 2012], and it predicts stars with masses above $2M_\odot$, even when hyperonic degrees of freedom are considered [Fortin et al., 2016]. The nucleon AMM are introduced via the coupling of the baryons to the electromagnetic field tensor with $\sigma_{\mu\nu} = \frac{i}{2}\left[\gamma_\mu,\gamma_\nu\right]$, and strength κ_b, with $\kappa_n = -1.91315$ for the neutron, and $\kappa_p = 1.79285$ for the proton, and μ_N is the nuclear magneton. The value of electron AMM is tiny when compared to the hadronic part, and its contribution will be negligible for the magnetic fields we are interested [Duncan, 2000].

According to the standard procedure of RMF theory [Yuan and Zhang, 1999, Rabhi et al., 2008, Rabhi et al., 2009a], the energy density of neu-

tron star matter can be calculated by

$$\varepsilon = \sum_{b=p,n} \varepsilon_b + \varepsilon_e + \frac{1}{2} m_s^2 \phi^2 + \frac{1}{2} m_v^2 V_0^2 + \frac{1}{2} m_\rho^2 b_0^2 \tag{2.31}$$

where the energy densities of nucleons and electrons at $T = 0$ read as following

$$\varepsilon_p = \frac{eB}{4\pi^2} \sum_\nu \sum_s \left[P_F^p \epsilon_F^p + \bar{m}_p^2 \ln \left| \frac{P_F^p + \epsilon_F^p}{\bar{m}_p} \right| \right], \tag{2.32}$$

$$\begin{aligned} \varepsilon_n &= \frac{1}{4\pi^2} \sum_s \left[\frac{1}{2} P_F^n \epsilon_F^{n3} - \frac{2}{3} s \mu_N \kappa_n B \epsilon_F^{n3} \left(\arcsin \left(\frac{\bar{m}_n}{\epsilon_F^n} \right) - \frac{\pi}{2} \right) \right. \\ &- \left. \left(\frac{1}{3} s \mu_N \kappa_n B + \frac{1}{4} \bar{m}_n \right) \left(\bar{m}_n P_F^n \epsilon_F^n + \bar{m}_n^3 \ln \left| \frac{P_F^n + \epsilon_F^n}{\bar{m}_n} \right| \right) \right], \end{aligned} \tag{2.33}$$

$$\varepsilon_e = \frac{eB}{4\pi^2} \sum_\nu \sum_s \left[P_F^e \epsilon_F^e + \left(m_e^2 + 2\nu eB \right) \ln \left| \frac{P_F^e + \epsilon_F^e}{\sqrt{m_e^2 + 2\nu eB}} \right| \right], \tag{2.34}$$

with $\bar{m}_p = \sqrt{M^{*2} + 2\nu eB} - s\mu_N \kappa_p B$, $\bar{m}_n = M^* - s\mu_N \kappa_n B$. The summation in ν in the above expressions terminates at $\nu_{max}^i (i = p, e)$, which is the largest value of ν for which the square of the Fermi momenta of the particle is still positive, and which corresponds to the closest integer from below, defined by the ratio

$$\nu_{max}^p = \frac{(\epsilon_F^p + s\mu_N \kappa_p B)^2 - M^{*2}}{2eB}, \tag{2.35}$$

$$\nu_{max}^e = \frac{{\epsilon_F^e}^2 - m_e^2}{2eB}, \tag{2.36}$$

where ϵ_F^p and ϵ_F^e are the Fermi energies of protons and electrons, respectively.

The pressure can be obtained from the following expression

$$P = \sum_i \mu_i \rho_v^i - \varepsilon = \mu_n \rho_b - \varepsilon \,, \tag{2.37}$$

where the charge neutrality and β-equilibrium conditions are used.

2.4 Neutron star structure

The properties of the EoS direct affect the structure of compact stars. The structure, in particular, the mass and radius, is obtained from the

integration of the Tolmann-Oppenheimer-Volkov (TOV) equations for spherically symmetric and static stars, which reads

$$\frac{dP}{dr}(r) = -\frac{P(r)+\varepsilon(r)}{r\left[r-2M(r)\right]}\left\{M(r)+4\pi r^3 P(r)\right\}, \tag{2.38}$$

$$M(r) = 4\pi\int_0^r \varepsilon(r) r^2 dr \tag{2.39}$$

where $\varepsilon(r)$, $P(r)$ and $M(r)$ are the energy density, pressure and mass of radius r, respectively.

In order to obtain these equations, we need to input the β-equilibrium EoS of stellar matter, which is a particular case of npe neutral matter. The chemical equilibrium of npe can be established by neutron beta decay

$$n \rightarrow p + e^- + \overline{\nu}_e. \tag{2.40}$$

Since the mean-free path of neutrinos is larger than the size of the star, we assume that neutrinos can escape freely, i.e. no neutrino trapping [Prakash et al., 1997]. Under these conditions, the neutrino chemical potential is zero and the equilibrium equation (2.40) relates the chemical potential of the protons, neutrons and electrons according to

$$\mu_p = \mu_n - \mu_e. \tag{2.41}$$

In addition, muons usually appear at a density $0.85\ \rho_0$ [C. Wen, 2006], and when the magnetic fields increase, this density value gets larger [C. Wen, 2006]. Since we are only interested in the structure of the crust, and the muon onset occurs in the core, they will not be considered in our present study. Besides β-equilibrium the charge neutrality $\rho_p = \rho_e$ must be imposed in order to obtain the EoS .

In practice, for a given baryonic density we solve self-consistently the following equations:
i) chemical equilibrium conditions;
ii) charge neutrality condition;
iii) meson equations of motion.

2.5 The moment of inertia

In the slow-rotation approximation, first studied by Hartle and Thorne [Hartle, 1967, Hartle and Thorne, 1968], the stellar moment of inertia is only sensitive to the equation of state. We will assume that the neutron star is rotating uniformly with a stellar frequency Ω, that is far smaller than the Kepler frequency at the equator.

The moment of inertia of a uniformly rotating, axisymmetric neutron star in hydrostatic equilibrium is given by the expression [Fattoyev and Piekarewicz, 2010]:

$$I = \frac{J}{\Omega} = \frac{8\pi}{3}\int_0^R r^4 e^{-\nu(r)}\frac{\bar{\omega}(r)}{\Omega}\frac{\Big(\varepsilon(r)+P(r)\Big)}{\sqrt{1-2GM(r)/r}}dr\ , \tag{2.42}$$

where J is the angular momentum, $\nu(r)$ and $\bar{\omega}(r)$ are radially-dependent metric functions and $M(r)$, $\varepsilon(r)$, and $P(r)$ are the stellar mass, energy density, and pressure, respectively. In the slow-rotation approximation, all the quantities appearing in Eq. (2.42) remain spherically symmetric, and, therefore, the stellar profiles may be determined by integrating the TOV equations.

The pulsar glitches may set some constraints on the EoS [Link et al., 1999, Lattimer and Prakash, 2001]. In particular, from the long time observation of glitches of the Vela pulsar, it has been suggested that at least 1.4% of the total moment of inertia must reside in the non-uniform crust [Link et al., 1999, Lattimer and Prakash, 2001]. The crustal moment of inertia is sensitive to the transition pressure at the crust-core interface. Although in some works, a correlation between this observable and the density-dependence of the symmetry energy was proposed [Worley et al., 2008, Xu et al., 2008, Xu et al., 2009], it was afterwards shown that no correlation seems to exist [Ducoin et al., 2010, Ducoin et al., 2011].

The crustal moment of inertia is defined in terms of Eq. (2.42), but with the range of integration limited from the crust-core transition radius, R_t, to the star radius, R, i.e.,

$$\Delta I_{cr} = \frac{8\pi}{3}\int_{R_t}^R r^4 e^{-\nu(r)}\widetilde{\omega}(r)\frac{\Big(\varepsilon(r)+P(r)\Big)}{\sqrt{1-2GM(r)/r}}dr\ . \tag{2.43}$$

Since the crust is thin and its density low, several approximations may be used to evaluate the integral in Eq. (2.43), [Lorenz et al., 1993, Ravenhall and Pethick, 1994, Link et al., 1999, Lattimer and Prakash, 2001, Lattimer and Prakash, 2007]. Taking these approximations, the crustal moment of inertia expression may be written in the form

$$\Delta I_{cr} \approx \frac{16\pi}{3}\frac{R_t^6 P_t}{R_s}\left[1-\left(\frac{R_s}{R}\right)\left(\frac{I}{MR^2}\right)\right]\left[1+\frac{48}{5}(R_t/R_s-1)(P_t/\varepsilon_t)+\ldots\right]\ , \tag{2.44}$$

where $R_s = 2GM$ is the Schwarzschild radius of the star, and $P_t = P(R_t)$ and $\varepsilon_t = \varepsilon(R_t)$ are the pressure and energy density at the core-crust interface. Using the relationship proposed in Ref. [Ravenhall and Pethick, 1994], namely,

$$\frac{I}{MR^2} = \frac{0.21}{1 - R_s/R}\,, \tag{2.45}$$

we obtain

$$\Delta I_{cr} \approx \frac{16\pi}{3}\frac{R_t^6 P_t}{R_s}\left[1 - \frac{0.21}{(R/R_s - 1)}\right]\left[1 + \frac{48}{5}(R_t/R_s - 1)(P_t/\varepsilon_t) + \ldots\right]\,. \tag{2.46}$$

It has been shown that this expression remains very accurate [Fattoyev and Piekarewicz, 2010]. According to this expression, the crustal moment of inertia of a neutron star with mass M and radius R depends only on R_t, P_t, and ε_t, and, therefore can give information on the equation of state. For completeness, an expression of the crustal mass is given by,

$$\Delta M_{cr} \approx 8\pi R_t^3 P_t (R_t/R_s - 1)\left[1 + \frac{32}{5}(R_t/R_s - 3/4)(P_t/\varepsilon_t) + \ldots\right]\,. \tag{2.47}$$

In the study of pulsar glitches, many models associate the glitch size to the fraction of the moment of inertia which resides in the crust of a neutron star where dripped neutrons coexist with nuclei. The high-density crust boundary is defined by the boundary between clusterized and uniform matter, where the pressure is P_t and the density is ρ_t. The low-density boundary is the neutron drip density. Instead of using the radius at the neutron drip density in the calculation, the star radius is generally taken because the amount of mass between the neutron drip point and the surface is negligible [Lattimer and Prakash, 2000].

The fractional moments of inertia in the present study will be calculated from the approximate expression given in [Worley et al., 2008, Lattimer and Prakash, 2000]:

$$\begin{aligned}\frac{\Delta I_{cr}}{I} &\simeq \frac{28\pi P_t R^3}{3M}\frac{(1 - 1.67\beta - 0.6\beta^2)}{\beta} \\ &\times \left[1 + \frac{2P_t(1 + 5\beta - 14\beta^2)}{\rho_t m \beta^2}\right]^{-1}\,,\end{aligned} \tag{2.48}$$

where P_t and ρ_t are the crust-core transition pressure and density, respectively, M and R are the gravitational mass and radius of the star,

$\beta = GM/R$ is the compactness parameter, and m is the nucleon mass. The dependence on the EoS arises from the values of P_t and ρ_t, but there is no explicit dependence on the higher-density EoS.

Chapter 3

Collective modes and instability region

In this section, we will first determine the dispersion relation of the normal modes of nuclear np matter and stellar npe matter. The Vlasov formalism [Nielsen et al., 1991, Nielsen et al., 1993], a semi-classical method that corresponds to the $\hbar \to 0$ limit of the time dependent Hartree-Fock method [Ring and Schuck, 1980] will be used.

A relativistic Vlasov equation, deduced from the Walecka model, was first proposed by Ko et al. [Ko et al., 1987, Ko and Li, 1988], and applied to the simulation of relativistic heavy-ion collisions. In Ref. [Ko and Li, 1988], the authors already included a collision term, and considered meson self-interaction terms as in the model proposed by Bodmer and Boguta [Boguta and Bodmer, 1977]. In the early nineties, zero sound modes in infinite symmetric nuclear matter were determined within the relativistic Vlasov equation at zero [Nielsen et al., 1991] and finite temperature [Nielsen et al., 1993]. In particular, at finite temperature, it was shown that the zero-sound mode merges in the continuum of particle-hole excitations. This formalism gives similar results to the ones obtained using the mean-field approximation for the ground-state, and calculating the meson propagators in the one-loop approximation [Lim and Horowitz, 1989].

The zero sound modes correspond to the eigenmodes of np and npe matter obtained, taking the linearization of the equations of motion of the mesons, and the Vlasov equation for the fermions, neutrons, protons and electrons. The asymmetric nuclear matter modes were first calculated within relativistic mean field models in Ref. [Avancini et al., 2005]. At subsaturation densities, nuclear matter presents imaginary modes, indicating the existence of a region of instabilities, as discussed

in [Providência et al., 2006b, Providência et al., 2006a]. In these references, the surface that defines the unstable region, denominated dynamical spinodal, was obtained, and the modes with the largest growth rates, the modulus of the imaginary mode, calculated. These modes allow the determination of some interesting properties, such as the average size of the clusters in non-homogeneous subsaturation matter.

In Section 3.1, we generalize the formalism presented in Refs. [Avancini et al., 2005, Providência et al., 2006b, Providência et al., 2006a] to magnetized nuclear matter, taking into account the anomalous magnetic moment of protons and neutrons. The dispersion relation of magnetized matter is calculated, and the dynamical spinodal determined. In the limit of low momentum, $k \to 0$, and excluding the Coulomb field, the dynamical spinodal converges to the thermodynamic spinodal. In Section 3.2, we study the simultaneous effects of the magnetic field and temperature on the instability region of magnetized nuclear matter. The finite temperature thermodynamical spinodal will be calculated.

3.1 Dynamical spinodal under strong magnetic fields

In the following, we determine the collective modes and the dynamical spinodal of magnetized nuclear matter within the Vlasov formalism discussed in [Nielsen et al., 1991, Providência et al., 2006a]. We are interested in stellar matter, therefore, besides neutrons and protons, we also include electrons. The Coulomb field is also taken explicitly into account.

In order to describe simultaneously the three particle species, neutrons, protons and electrons, we introduce a distribution function that includes these three degrees of freedom. In particular, the distribution function for npe matter at position $\mathbf{r}$, instant t, and momentum $\mathbf{p}$ is given by

$$f(\mathbf{r}, \mathbf{p}, t) = \mathrm{diag}(f_p,\ f_n,\ f_e)\,, \tag{3.1}$$

and its time evolution is described in the Vlasov equation:

$$\frac{\partial f_i}{\partial t} + \{f_i, h_i\} = 0,\ i = p,\ n,\ e. \tag{3.2}$$

$\{,\}$ denotes the Poisson brackets. The one-body hamiltonian,

$h = \mathrm{diag}\,(h_p, h_n, h_e)$, is given by

$$h_i = \epsilon_i + \mathcal{V}_0^i, \quad \epsilon_i = \sqrt{(\bar{\boldsymbol{p}}_z^i)^2 + \bar{m}_i^2}, \quad i = p, e \tag{3.3}$$

$$h_n = \epsilon_n + \mathcal{V}_0^n, \ \epsilon_n = \sqrt{\left(\bar{\boldsymbol{p}}_z^n\right)^2 + \left(\epsilon_\perp^n - s\mu_N\kappa_n B\right)^2}, \tag{3.4}$$

with

$$\bar{\boldsymbol{p}}^i = \boldsymbol{p} - \boldsymbol{\mathcal{V}}^i, \tag{3.5}$$

and

$$\bar{m}_p = \sqrt{M^{*2} + 2\nu eB} - s\mu_N\kappa_p B, \tag{3.6}$$

$$\bar{m}_e = \sqrt{m_e^{*2} + 2\nu eB}, \tag{3.7}$$

$$\epsilon_\perp^n = \sqrt{M^{*2} + \left(\bar{\boldsymbol{p}}_\perp^n\right)^2}, \tag{3.8}$$

$$\mathcal{V}_\mu^n = g_v V_\mu - \frac{g_\rho}{2}\, b_\mu, \tag{3.9}$$

$$\mathcal{V}_\mu^p = g_v V_\mu + \frac{g_\rho}{2}\, b_\mu + e\, A_\mu, \tag{3.10}$$

$$\mathcal{V}_\mu^e = -e\, A_\mu. \tag{3.11}$$

$\nu = n + \frac{1}{2} - \mathrm{sgn}(q)\frac{s}{2} = 0, 1, 2, \ldots$ enumerates the Landau levels of the fermions with electric charge q, the quantum number s is $+1$ (-1) for spin parallel (anti-parallel) to the magnetic field direction, taken in the z-direction. We define the vectors $(\boldsymbol{p},\, \boldsymbol{V}, ...)$ along directions parallel $(\boldsymbol{p}_z,\, \boldsymbol{V}_z, ...)$ and perpendicular $(\boldsymbol{p}_\perp,\, \boldsymbol{V}_\perp, ...)$ to the magnetic field.

We obtain the time evolution equations from the Euler-Lagrange formalism for the fields ϕ, V^μ, A^μ, and the third component of the ρ-field $b_3^\mu = (b_0, \mathbf{b})$. These equations are given in Appendix A.

At zero temperature, the ground state of the system is characterized by the neutron, proton and electron Fermi momenta, $P_F^i\,(i = p, n, e)$, and is described by the equilibrium distribution function

$$f_0(\mathbf{r}, \mathbf{p}) = \mathrm{diag}[\Theta(P_F^{p2} - p^2), \Theta(P_F^{n2} - p^2), \Theta(P_F^{e2} - p^2)], \tag{3.12}$$

where

$$P_F^p = \sqrt{\epsilon_F^p - \bar{m}_p^2}, \tag{3.13}$$

$$P_F^n = \sqrt{\gamma - \sqrt{\gamma^2 - \beta}}, \tag{3.14}$$

$$P_F^e = \sqrt{\epsilon_F^e - \bar{m}_e^2}, \tag{3.15}$$

are the Fermi momenta of protons, neutrons and electrons, respectively, and

$$\gamma = \alpha + 2\left(s\mu_N\kappa_n B\right)^2\left(1-x^2\right), \tag{3.16}$$

$$\alpha = \epsilon_F^{n2} - M^{*2} - \left(s\mu_N\kappa_n B\right)^2, \tag{3.17}$$

$$\beta = \alpha^2 - 4\left(s\mu_N\kappa_n B\right)^2 M^{*2}, \tag{3.18}$$

with $x = \cos\theta'$, θ' being the polar angle.

The equilibrium state is also defined by the constant mesonic fields, that are given by the following equations

$$m_s^2\phi_0 + \frac{\kappa}{2}\phi_0^2 + \frac{\lambda}{6}\phi_0^3 = g_s\rho_s^{(0)}, \tag{3.19}$$

$$m_v^2\, V_0^{(0)} + 2\Lambda_v g_v^2 g_\rho^2 V_0^{(0)} b_0^{(0)2} = g_v j_0^{(0)}, \tag{3.20}$$

$$m_\rho^2\, b_0^{(0)} + 2\Lambda_v g_v^2 g_\rho^2 V_0^{(0)2} b_0^{(0)} = \frac{g_\rho}{2} j_{3,0}^{(0)}, \tag{3.21}$$

$$V_i^{(0)} = b_i^{(0)} = A_0^{(0)} = A_i^{(0)} = 0, \tag{3.22}$$

where $\rho_s^{(0)}$, $j_0^{(0)}$, $j_{3,0}^{(0)}$ are the equilibrium scalar density, the nuclear density, and the isospin density, respectively. The spatial components of V^μ, b^μ and A^μ are zero because there are no currents in the system.

The Fermi momentum of the neutron, P_F^n, is derived from the following equation:

$$\epsilon_F^n = \sqrt{P_{Fz}^{n2} + \left(\sqrt{M_n^{*2} + P_{F\perp}^{n2}} - s\mu_N\kappa_n B\right)^2}, \tag{3.23}$$

with $P_{Fz}^n = P_F^n\cos\theta' = P_F^n x$, and $P_{F\perp}^n = P_F^n\sin\theta' = P_F^n\sqrt{1-x^2}$.

The collective modes, which are obtained by considering small oscillations around the equilibrium state, are given by the solutions of the linearized equations of motion. The deviations from equilibrium are described by

$$f_i = f_{0i} + \delta f_i\ , \tag{3.24}$$

$$\phi = \phi_0 + \delta\phi\ , \tag{3.25}$$

$$V_0 = V_0^{(0)} + \delta V_0\ , \quad V_i = \delta V_i\ , \tag{3.26}$$

$$b_0 = b_0^{(0)} + \delta b_0\ , \quad b_i = \delta b_i\ , \tag{3.27}$$

$$A_0 = \delta A_0\ , A_i = \delta A_i. \tag{3.28}$$

We use a generating function

$$S(\mathbf{r},\mathbf{p}) = \begin{pmatrix} S_p & 0 & 0 \\ 0 & S_n & 0 \\ 0 & 0 & S_e \end{pmatrix}, \tag{3.29}$$

which contains the isospin space defined by protons and neutrons, and the electron degree of freedom, such that the fluctuations are given by

$$\delta f_i \;=\; \{S_i, f_{0i}\} \;=\; -\{S_i, p^2\}\delta(P_F^{i2} - p^2)\;. \tag{3.30}$$

The linearized Vlasov equations for δf_i written as,

$$\frac{d\delta f_i}{dt} + \{\delta f_i, h_{0i}\} + \{f_{0i}, \delta h_i\} = 0, \tag{3.31}$$

are equivalent to the following time evolution equations:

$$\frac{\partial S_i}{\partial t} + \{S_i, h_{0i}\} = \delta h_i,\; i = p,\, n,\, e, \tag{3.32}$$

where

$$\delta h_p = -\frac{\mathbf{p_z}\cdot\delta\boldsymbol{\mathcal{V}}_z^p}{\epsilon^p_{static}} - \frac{g_s\, M^*\bar{m}_p}{\epsilon^p_{static}(\bar{m}_p + s\mu_N\kappa_p B)}\delta\phi + \delta\mathcal{V}_{0p}, \tag{3.33}$$

$$\delta h_n = -\frac{\mathbf{p_z}\cdot\delta\boldsymbol{\mathcal{V}}_z^n}{\epsilon^n_{static}} - \frac{g_s\, M^*}{\epsilon^n_{static}}\left(1 - \frac{s\mu_N\kappa_n B}{\sqrt{M^{*2} + {\mathbf{p}_\perp}^2}}\right)\delta\phi + \delta\mathcal{V}_{0n}, \tag{3.34}$$

$$\delta h_e = e\left[\frac{\mathbf{p_z}\cdot\delta\mathbf{A}_z}{\epsilon^e_{static}} - \delta A_0\right], \tag{3.35}$$

with

$$\epsilon^p_{static} = \sqrt{p_z^2 + \bar{m}_p^2}, \tag{3.36}$$

$$\epsilon^n_{static} = \sqrt{p_z^2 + \left(\sqrt{M_n^{*2} + p_\perp^2} - s\mu_N\kappa_n B\right)^2}, \tag{3.37}$$

$$\epsilon^e_{static} = \sqrt{p_z^2 + \bar{m}_e^2}. \tag{3.38}$$

The linearized equations of the fields are given by

$$\frac{\partial^2\delta\phi}{\partial t^2} - \nabla^2\delta\phi + (m_s^2 + \kappa\phi_0 + \frac{\lambda}{2}\phi_0^2)\delta\phi \;=\; g_s\left[\delta\rho_{sp}(\mathbf{r},t) + \delta\rho_{sn}(\mathbf{r},t)\right]\,, \tag{3.39}$$

$$\frac{\partial^2\delta V_\mu}{\partial t^2} - \nabla^2\delta V_\mu + m_v^2\delta V_\mu \;+ 2\Lambda_v g_v^2 g_\rho^2 b_{3\mu}\cdot b^{3\mu}\delta V_\mu = \; g_v[\delta j_\mu^p + \delta j_\mu^n]\,, \tag{3.40}$$

$$\frac{\partial^2\delta b_{3\mu}}{\partial t^2} - \nabla^2\delta b_{3\mu} + m_\rho^2\delta b_{3\mu} \;+ 2\Lambda_v g_v^2 g_\rho^2 V_\mu V^\mu\delta b_{3\mu} = \; \frac{g_\rho}{2}[\delta j_\mu^p - \delta j_\mu^n]\,, \tag{3.41}$$

$$\frac{\partial^2\delta A_\mu}{\partial t^2} - \nabla^2\delta A_\mu \;=\; e[\delta j_\mu^p - \delta j_\mu^e]\;. \tag{3.42}$$

In the present work, only the longitudinal modes are considered, with momentum $\boldsymbol{k}$ in the direction of the magnetic field, and a frequency ω. They are described by the following ansatz

$$\begin{pmatrix} S_j(\mathbf{r},\mathbf{p},t) \\ \delta\phi \\ \delta B_0 \\ \delta B_i \end{pmatrix} = \begin{pmatrix} \mathcal{S}^j_\omega(p,\cos\theta) \\ \delta\phi_\omega \\ \delta B^0_\omega \\ \delta B^i_\omega \end{pmatrix} \mathrm{e}^{i(\omega t - \mathbf{k}_z\cdot\mathbf{r})} \ , \tag{3.43}$$

where $j = p,\, n\,, e,\, B = V,\, b, A$ represents the vector fields, and θ is the angle between $\mathbf{p}$ and $\mathbf{k}_z$.

For these modes, we get $\delta V^x_\omega = \delta V^y_\omega = 0$, $\delta b^x_\omega = \delta b^y_\omega = 0$ and $\delta A^x_\omega = \delta A^y_\omega = 0$. Calling $\delta V^z_\omega = \delta V_\omega$, $\delta b^z_\omega = \delta b_\omega$ and $\delta A^z_\omega = \delta A_\omega$, we have $\delta\mathcal{V}_{i,z} = \delta\mathcal{V}^i_\omega \mathrm{e}^{i(\omega t - \mathbf{k}_z\cdot\mathbf{r})}$, $\quad \delta\mathcal{V}_{0i} = \delta\mathcal{V}^{0i}_\omega \mathrm{e}^{i(\omega t - \mathbf{k}_z\cdot\mathbf{r})}$.

Replacing the ansatz (3.43) in Eqs. (3.32), we get

$$i(\omega - \omega_{0p}\xi)\mathcal{S}^p_\omega(\xi) = -g_s\frac{M^*}{\epsilon^p_F}\left(\frac{\bar{m}_p}{\bar{m}_p + s\mu_N\kappa_p B}\right)\delta\phi_\omega - V^p_F\xi\delta\mathcal{V}^p_\omega + \delta\mathcal{V}^{0p}_\omega \ , \tag{3.44}$$

$$\begin{aligned} i(\omega - \omega_{0n}x)\mathcal{S}^n_\omega(x) &= -g_s\frac{M^*}{\epsilon^n_F}\left(1 - \frac{s\mu_N\kappa_n B}{\sqrt{M^{*2} + P^{n2}_F(1-x^2)}}\right)\delta\phi_\omega \\ &\quad -V^n_F x\delta\mathcal{V}^n_\omega + \delta\mathcal{V}^{0n}_\omega \ , \end{aligned} \tag{3.45}$$

$$i(\omega - \omega_{0e}\xi)\mathcal{S}^e_\omega(\xi) = e\left(V^e_F\xi\delta A_\omega - \delta A^0_\omega\right) \ , \tag{3.46}$$

$$\begin{aligned} \left(\omega^2 - k^2 - m^2_{s,eff}\right)\delta\phi_\omega &= -\frac{ig_s M^*}{(2\pi)^2}\left[\sum_{\nu,s,\xi}\frac{eBk_z}{\epsilon^p_F}\frac{\bar{m}_p\xi\mathcal{S}^p_\omega(\xi)}{(\bar{m}_p + s\mu_N\kappa_p B)}\right. \\ &\quad + \left. P^n_F\omega_{0n}\sum_s\int_{-1}^{1} x\mathcal{S}^n_\omega(x)\left(1 - \frac{s\mu_N\kappa_n B}{\sqrt{M^{*2} + P^{n2}_F(1-x^2)}}\right)dx\right] , \end{aligned} \tag{3.47}$$

$$\begin{aligned} \left(\omega^2 - k^2 - m^2_{v,eff}\right)\delta V^0_\omega &= \chi\delta b^0_\omega - \frac{ig_v}{(2\pi)^2}\left(\sum_{\nu,s,\xi} eBk_z\xi\mathcal{S}^p_\omega(\xi)\right. \\ &\quad \left. + P^n_F\epsilon^n_F\omega_{on}\int_{-1}^{1} x\mathcal{S}^n_\omega(x)dx\right) \ , \end{aligned} \tag{3.48}$$

$$\begin{aligned} \left(\omega^2 - k^2 - m^2_{\rho,eff}\right)\delta b^0_\omega &= \chi\delta V^0_\omega - \frac{ig_\rho}{2(2\pi)^2}\left(\sum_{\nu,s,\xi} eBk_z\xi\mathcal{S}^p_\omega(\xi)\right. \\ &\quad \left. - P^n_F\epsilon^n_F\omega_{on}\int_{-1}^{1} x\mathcal{S}^n_\omega(x)dx\right) \ , \end{aligned} \tag{3.49}$$

$$\left(\omega^2 - k^2\right)\delta A^0_\omega = -\frac{e^2 B}{(2\pi)^2}ik_z\sum_{\nu,s,\xi}\xi(\mathcal{S}^p_\omega(\xi) - \mathcal{S}^e_\omega(\xi)) \ , \tag{3.50}$$

where

$$\omega_{0i} = k_z V_F^i = k_z P_F^i/\epsilon_F^i,\ i = p, n, e, \tag{3.51}$$

$$m_{s,eff}^2 = m_s^2 + \kappa\phi_0 + \frac{\lambda}{2}\phi_0^2 + g_s^2\frac{d\rho_s}{dM^*}, \tag{3.52}$$

$$m_{v,eff}^2 = m_v^2 + 2\Lambda_v g_v^2 g_\rho^2 b_0^{(0)2}, \tag{3.53}$$

$$m_{\rho,eff}^2 = m_\rho^2 + 2\Lambda_v g_v^2 g_\rho^2 V_0^{(0)2}, \tag{3.54}$$

with $\xi = \pm 1, x = \cos\theta$, and $\chi = 4\Lambda_v g_v^2 g_\rho^2 V_0^{(0)} b_0^{(0)}$.

From the continuity equation for the density currents, we get for the components of the vector fields

$$k_z\,\delta V_\omega = \omega\delta V_\omega^0 - \frac{\omega}{\omega_v^2}\chi\delta b_\omega^0 \tag{3.55}$$

$$k_z\,\delta b_\omega = \omega\delta b_\omega^0 - \frac{\omega}{\omega_\rho^2}\chi\delta V_\omega^0 \tag{3.56}$$

$$k_z\,\delta A_\omega = \omega\delta A_\omega^0 \tag{3.57}$$

with $\omega_v^2 = \omega^2 - k^2 - m_{v,eff}^2$ and $\omega_\rho^2 = \omega^2 - k^2 - m_{\rho,eff}^2$.

Substituting the set of equations (3.47)-(3.50) into Eqs. (3.44)-(3.46), we get a set of five independent equations of motion in terms of the amplitudes of the proton and neutron scalar density fluctuations, $A_{\omega,\nu,s}^{ps}$, $A_{\omega,s}^{ns}$, respectively, and in terms of the amplitudes of the proton, neutron and electron vector density fluctuations, $A_{\omega,\nu,s}^{p}$, $A_{\omega,s}^{n}$, $A_{\omega,\nu,s}^{e}$ given by

$$A_{\omega,\nu,s}^{ps} = \sum_\xi \xi \frac{\bar{m}_p}{(\bar{m}_p + s\mu_N\kappa_p B)} S_{\omega,\nu,s}^p(\xi), \tag{3.58}$$

$$A_{\omega,s}^{ns} = \int_{-1}^{1} P_F^{n2} x \left(1 - \frac{s\mu_N\kappa_n B}{\sqrt{M_n^{*2} + P_F^{n2}(1-x^2)}}\right) S_{\omega,s}^n dx, \tag{3.59}$$

$$A_{\omega,\nu,s}^{p} = \sum_\xi \xi S_{\omega,\nu,s}^p(\xi), \tag{3.60}$$

$$A_{\omega,s}^{n} = \int_{-1}^{1} P_F^{n2} x S_{\omega,s}^n dx, \tag{3.61}$$

$$A_{\omega,\nu,s}^{e} = \sum_\xi \xi S_{\omega,\nu,s}^e(\xi). \tag{3.62}$$

The equations for the unknowns A_ω^i are written in the matrix form as

$$\begin{pmatrix} a_{11} & a_{12} & a_{13} & a_{14} & a_{15} \\ a_{21} & a_{22} & a_{23} & a_{24} & a_{25} \\ a_{31} & a_{32} & a_{33} & a_{34} & 0 \\ a_{41} & a_{42} & a_{43} & a_{44} & 0 \\ 0 & a_{52} & 0 & 0 & a_{55} \end{pmatrix} \begin{pmatrix} \sum_{\nu,s} A_{\omega,\nu,s}^{ps} \\ \sum_{\nu,s} A_{\omega,\nu,s}^{p} \\ \sum_{s} A_{\omega,s}^{ns} \\ \sum_{s} A_{\omega,s}^{n} \\ \sum_{\nu,s} A_{\omega,\nu,s}^{e} \end{pmatrix} = 0. \tag{3.63}$$

where the matrix elements a_{ij} are defined in Appendix B. The dispersion relation for the collective modes in magnetized nuclear matter is obtained by equating the determinant of the matrix of the coefficients of the above equation to zero, namely

$$\begin{vmatrix} a_{11} & a_{12} & a_{13} & a_{14} & a_{15} \\ a_{21} & a_{22} & a_{23} & a_{24} & a_{25} \\ a_{31} & a_{32} & a_{33} & a_{34} & 0 \\ a_{41} & a_{42} & a_{43} & a_{44} & 0 \\ 0 & a_{52} & 0 & 0 & a_{55} \end{vmatrix} = 0. \tag{3.64}$$

The eigenmodes ω of the system correspond to the solutions of the dispersion relation (3.64).

The density fluctuations of neutrons and electrons can be written in terms of the proton density fluctuations as

$$\delta\rho_n/\delta\rho_p = \frac{A^n_{\omega,s}}{eBA^p_{\omega,\nu,s}}, \tag{3.65}$$

$$\delta\rho_e/\delta\rho_p = \frac{A^e_{\omega,\nu,s}}{A^p_{\omega,\nu,s}}. \tag{3.66}$$

The first ratio $\delta\rho_n/\delta\rho_p$ allows us to define how strong is the distillation effect, e. g. how efficient is the separation of matter into a neutron rich low density gas and a more isospin symmetric cluster. The second ratio $\delta\rho_e/\delta\rho_p$ indicates under which conditions the electrons and protons move independently.

At low densities, the system has unstable modes characterized by an imaginary frequency, ω. The dynamical spinodal surface in the (ρ_p, ρ_n) space, for a given wave vector k, is obtained by imposing $\omega = 0$. Inside this unstable region, we also calculate the mode with the largest growth rate, Γ, defined as $\omega = i\Gamma$. This mode is the one that drives the system into a non-homogeneous system formed by clusters immersed in a background neutron-rich gas. By taking its half-wavelength, we can get a good estimation of the size of the clusters (liquid) that appear in the mixed (liquid-gas) phase, i.e. in the inner crust of the stars [Brito et al., 2006].

In the next chapter, we will concentrate on the unstable modes, in particular, we will calculate the dynamical spinodal and identify the modes with the largest growth rates.

3.2 Thermodynamical spinodal under strong magnetic fields

The thermodynamical spinodal gives a good estimation of the lower limit of the pasta phase extension [Avancini et al., 2010]. In Refs. [Rabhi et al., 2009a, Rabhi et al., 2009b], the authors show that the bands of instability and wider unstable regions can be produced under strong magnetic fields, using the thermodynamical instabilities at $T = 0$. However, most of the results are focused on the magnetic fields of the order of $10^{18} - 10^{19}$ G, which are far larger than the current astronomical observation of magnetars. Recently, smaller magnetic fields, between 10^{16} and 5×10^{17} G, have been considered in a very similar analysis done at $T = 0$ in Ref. [Chen, 2017]. There, the author has essentially discussed the effect of the symmetry energy on the extension of the thermodynamical spinodal and the behaviour of the proton and neutron fluctuation ratio.

In the following, we present the formalism of the thermodynamical spinodal, and discuss the thermodynamical instabilities at low densities for np matter under magnetic fields of the order of $10^{15} - 10^{17}$ G. We will consider the calculation of the thermodynamical spinodal at finite temperature, and a special interest will be set on the discussion of the effect of the magnetic field on the crust-core transition, which was not done before for the low magnetic fields that we are considering. Moreover, a comparison with the results obtained within a dynamical spinodal calculation will also be carried out in Chapter 5.

Below, we give a detailed calculation of the thermodynamical spinodal and relative quantities. Denoting by

$$f(\mathbf{r}, \mathbf{p}, t)_{\pm} = \mathrm{diag}(f_{p\pm},\ f_{n\pm},\ f_{e\pm}) \tag{3.67}$$

the distribution functions of particles (+) at position $\mathbf{r}$, instant t and momentum $\mathbf{p}$, and of antiparticles (-) at position $\mathbf{r}$, instant t and momentum $-\mathbf{p}$, the scalar and vector densities are written as

$$\rho_{sp} = \frac{eB}{(2\pi)^2} \sum_{\nu,s} \int (f_{p+} + f_{p-}) \frac{\bar{m}_p M^*}{(\bar{m}_p + s\mu_N \kappa_p B)\, \epsilon_p} dp\ , \tag{3.68}$$

$$\rho_{sn} = \frac{1}{(2\pi)^3} \sum_{s} \int (f_{n+} + f_{n-}) \left(1 - \frac{s\mu_N \kappa_n B}{\sqrt{M_n^{*2} + p_\perp^2}}\right) \frac{M^*}{\epsilon_n} d^3p\ , \tag{3.69}$$

$$\rho_i = \frac{eB}{(2\pi)^2} \sum_{\nu,s} \int (f_{i+} - f_{i-}) dp, \quad i = p, e\ , \tag{3.70}$$

$$\rho_n = \frac{1}{(2\pi)^3}\sum_s \int (f_{n+} - f_{n-}) d^3p \,, \tag{3.71}$$

where

$$\epsilon_p = \sqrt{(\bar{\boldsymbol{p}}_z^p)^2 + \bar{m}_p^2}\,, \tag{3.72}$$

$$\epsilon_n = \sqrt{(\bar{\boldsymbol{p}}_z^n)^2 + (\epsilon_\perp^n - s\mu_N\kappa_n B)^2}\,, \tag{3.73}$$

$$\epsilon_\perp^n = \sqrt{M^{*2} + (\bar{\boldsymbol{p}}_\perp^n)^2}\,, \tag{3.74}$$

with

$$\bar{\boldsymbol{p}} = \boldsymbol{p} - \boldsymbol{\mathcal{V}}, \tag{3.75}$$

and

$$\bar{m}_p = \sqrt{M^{*2} + 2\nu eB} - s\mu_N\kappa_p B, \tag{3.76}$$

$$\mathcal{V}_\mu^n = g_v V_\mu - \frac{g_\rho}{2}\, b_\mu, \tag{3.77}$$

$$\mathcal{V}_\mu^p = g_v V_\mu + \frac{g_\rho}{2}\, b_\mu + e\, A_\mu. \tag{3.78}$$

$\nu = n + \frac{1}{2} - \mathrm{sgn}(q)\frac{s}{2} = 0, 1, 2, \ldots$ enumerates the Landau levels of the fermions with electric charge q, and s is the quantum number spin, with $+1$ for spin up, and -1 for spin down. The vectors ($\boldsymbol{p}$, $\boldsymbol{V}, ...$) are defined along parallel ($\boldsymbol{p}_z$, $\boldsymbol{V}_z, ...$) and perpendicular ($\boldsymbol{p}_\perp$, $\boldsymbol{V}_\perp, ...$) directions, since the magnetic field is taken in the z-direction.

The state which minimizes the energy of asymmetric npe matter is characterized by the distribution functions

$$f_{0i\pm} = \frac{1}{1 + e^{(\epsilon_{0i} \mp \nu_i)/T}}, \tag{3.79}$$

with $\nu_i = \mu_i - g_v V_0 - \frac{g_\rho}{2}\tau_i b_0 - e\, A_0 \frac{1+\tau_i}{2}$, for $i = p, n$, and $\nu_e = \mu_e$ for the electrons, and by the constant mesonic fields which obey the following equations

$$m_s^2\phi_0 + \frac{\kappa}{2}\phi_0^2 + \frac{\lambda}{6}\phi_0^3 = g_s(\rho_{sp} + \rho_{sn}), \tag{3.80}$$

$$m_v^2\, V_0 + 2\Lambda_v g_v^2 g_\rho^2 V_0 b_0^2 = g_v(\rho_p + \rho_n), \tag{3.81}$$

$$m_\rho^2\, b_0 + 2\Lambda_v g_v^2 g_\rho^2 V_0^2 b_0 = \frac{g_\rho}{2}(\rho_p - \rho_n), \tag{3.82}$$

with all the spatial components of the vector fields being zero, and for homogeneous matter, A_0 is also zero. Notice that for $T = 0$ MeV, the distribution functions $f_{0i\pm}$ become $f_{0i+} = \theta(P_{Fi}^2 - p^2)$, $f_{0i-} = 0$ [Brito et al., 2006].

Nuclear matter at subsaturation densities has a liquid-gas phase transition. Homogeneous matter is unstable if the free energy curvature is negative.

In infinite matter, the free energy can be reduced to a free energy density [Müller and Serot, 1995, Margueron and Chomaz, 2003], which is written as

$$F(T,\rho_i) = -p(T,\mu_i) + \sum_{i=p,n} \mu_i \rho_i, \tag{3.83}$$

with the chemical potentials $\mu_n = \frac{\partial F}{\partial \rho_n}$ and $\mu_p = \frac{\partial F}{\partial \rho_p}$. The stability conditions for asymmetric nuclear matter are obtained from the free energy density, by imposing that the function is convex on the densities ρ_p and ρ_n, keeping the volume and temperature constant [Margueron and Chomaz, 2003]. For stable homogeneous matter, the stability matrix is given by

$$\mathcal{F}_{ij} = \left(\frac{\partial^2 F}{\partial \rho_i \partial \rho_j} \right)_T . \tag{3.84}$$

Then, the thermodynamical spinodal is the surface in the (ρ_n, ρ_p, T) space where the determinant of the free energy curvature matrix

$$\mathcal{F} = \begin{pmatrix} \frac{\partial \mu_n}{\partial \rho_n} & \frac{\partial \mu_n}{\partial \rho_p} \\ \frac{\partial \mu_p}{\partial \rho_n} & \frac{\partial \mu_p}{\partial \rho_p}, \end{pmatrix} , \tag{3.85}$$

is zero, i.e. the smallest eigenvalue is zero since the largest one is always positive. Inside this surface, nuclear matter is unstable. Fig. 3.1, taken from Ref. [Müller and Serot, 1995], shows an example of such situation for symmetric nuclear matter at $T = 11$ MeV: in the range of densities, limited by $\rho(A')$ and $\rho(B')$, the free energy density curvature is negative, which corresponds to the thermodynamic spinodal region.

We define

$$\mathbf{Tr}(\mathcal{F}) = \frac{\partial \mu_n}{\partial \rho_n} + \frac{\partial \mu_p}{\partial \rho_p} \tag{3.86}$$

and

$$\mathbf{Det}(\mathcal{F}) = \frac{\partial \mu_n}{\partial \rho_n}\frac{\partial \mu_p}{\partial \rho_p} - \frac{\partial \mu_p}{\partial \rho_n}\frac{\partial \mu_n}{\partial \rho_p}. \tag{3.87}$$

For a given temperature T, the eigenvalues of the stability matrix are given by

$$\lambda_\pm = \frac{1}{2}\left(\mathbf{Tr}(\mathcal{F}) \pm \sqrt{\mathbf{Tr}(\mathcal{F})^2 - 4\mathbf{Det}(\mathcal{F})} \right). \tag{3.88}$$

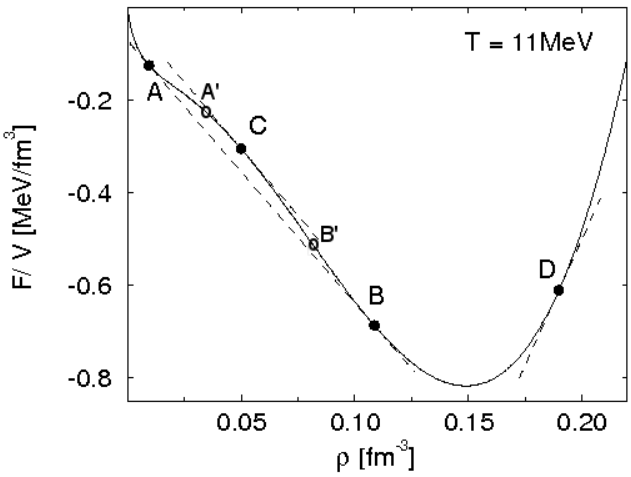

Figure 3.1: Free energy density minus $E_{B0}\rho$, where E_{B0} is the energy per particle at saturation, and ρ is the baryonic density. Points A and B belong to the binodal, A' and B' are spinodal points, and in C the free energy density is concave, therefore, the system is unstable. Figure taken from [Müller and Serot, 1995].

The ratios obtained from the eigenvectors $\delta\rho_\pm$ of the stability matrix, given by

$$\frac{\delta\rho_i^\pm}{\delta\rho_j^\pm} = \frac{\lambda_\pm - \mathcal{F}_{jj}}{\mathcal{F}_{ji}},\ i,j = p,n, \tag{3.89}$$

are quantities that give information on how matter will separate into two phases, in particular, a neutron-rich low density phase and a more isospin symmetric high density phase. In Chapter 5, these quantities will be calculated and the effect of the magnetic field on the isospin content in the low and high density phases, known as isospin distillation effect, will be discussed.

Although not so important, we show, for completeness, the expression that allows the calculation of the thermodynamical spinodal of stellar matter, i.e. taking electrons explicitly into account. Since stellar matter is charge neutral, the fraction of electrons is not free but it is determined by the proton density

$$\rho_e = \rho_p. \tag{3.90}$$

Building the free energy density that includes the contribution of neutrons, protons and electrons, and taking the derivative with respect to

the proton density gives

$$\frac{\partial F}{\partial \rho_p} = \mu_p + \mu_e, \tag{3.91}$$

so that the stability matrix (3.85) for npe matter reads

$$\mathcal{F} = \begin{pmatrix} \dfrac{\partial \mu_n}{\partial \rho_n} & \dfrac{\partial \mu_n}{\partial \rho_p} \\ \dfrac{\partial \mu_p}{\partial \rho_n} & \dfrac{\partial \left(\mu_p + \mu_e\right)}{\partial \rho_p} \end{pmatrix}. \tag{3.92}$$

The stability conditions are the same as the ones indicated for np matter: the trace and the determinant of $\mathcal{F}$ must be positive [Avancini et al., 2006, Rabhi et al., 2009a]. It was shown that in the absence of an external magnetic field, and depending on the models, due to the large incompressibility of the gas of electrons, the instability region predicted in this case could disappear completely, or be reduced to a very small region in phase space.

The big difference with respect to the dynamical spinodal is that, in the calculation of the thermodynamical spinodal, the electrons are completely tied to the protons, while in the dynamical spinodal, this only occurs in the limit of a very large wavelength: in general, the fluctuations of protons and electrons are independent.

Chapter 4

Dynamical spinodal

In the present and next chapters, we display the main results of this thesis, which were obtained using the formalism that has been discussed in the previous chapter. In this chapter, the instability region of cold magnetized nuclear matter is discussed within a dynamical spinodal calculation. In the first section, we discuss the properties of the spinodal surface, and in the second section, the behaviour of the maximum growth rate, which is the mode that drives the system into a nonhomogeneous structure, is examined.

4.1 Spinodal section

In this section, we apply the formalism presented in Section 3.1 to calculate the dynamical spinodals for the NL3 and NL3$\omega\rho$ models, taking different intensities for the external magnetic field. As discussed in Chapter 2, one of the reasons that justifies our choice of models is the fact that they present a quite different behaviour of the symmetry energy with density, and will also allow us to refer to the symmetry energy behavior when analyzing the results.

As already said in the previous chapter, the spinodal surfaces in the (ρ_p,ρ_n) space are characterized by a zero frequency solution of the dispersion relation, Eq. (3.64). For each proton fraction, we determine numerically the pair (ρ_p,ρ_n) that corresponds to a solution with $\omega = 0$.

We have written a code to determine the dynamical spinodal, where we first determine the ground-state configuration of npe matter, solving self-consistently the set of equations of motion for the mesons in the ground-state configuration, for a given proton fraction, Eqs. (3.19)–

(3.21). The electron configuration is determined by imposing electrical charge neutrality. Next, we calculate the eigenmode frequencies looking for the zeros of the dispersion relation (3.64). For each eigenmode, the neutron, proton and electron density fluctuations are determined from equations (3.63). To calculate the spinodal, we look for the values in the plane (ρ_n,ρ_p), that satisfy the dispersion relation (3.64) for a zero frequency. For each proton fraction, we get several solutions for densities below 0.2 fm^{-3} for NL3, and below 0.12 fm^{-3} for NL3$\omega\rho$, represented by points in the (ρ_n,ρ_p) plane. Each point is a solution of the dispersion relation obtained for a fixed proton fraction, which varies between 0 and 1. Due to this numerical limitation, the spinodal sections are made of points, which, however, define closed regions.

In Fig. 4.1, we show the dynamical spinodal regions composed by several irregular regions, which were obtained with different values of the momentum transfer k, corresponding to perturbations with different wave lengths, for a magnetic field $B^* = 5 \times 10^3$, which corresponds to $B = B^* B_{ce} = 2.2 \times 10^{17}$ G, where $B_{ce} = 4.41 \times 10^{13}$ G, being the electron critical magnetic field, and taking the NL3 model without AMM. We start to consider a small value, $k = 5$ MeV, and find that the influence of the electrons is very strong, and the spinodal section has almost disappeared when $B = 0$. Taking a finite magnetic field, the spinodal presents, besides the central component with a similar size, a very difuse distribution of disconnected regions, that extend to quite large densities. Increasing k, the spinodal section increases, until k is in the range $50-90$ MeV, a behavior similar to what happens in magnetic field free matter. It is mainly the Coulomb contribution that varies with the inverse of k^2 that explains this behaviour. However, the inclusion of the proton-electron infinite range coupling forces the proton and electron fluctuations to be in phase at the infinite wave length limit, e. g. k small. For a finite k density modulation, the local electroneutrality is not anymore needed, electrons and protons fluctuate independently and this leads to a larger instability region. Above the range $50 - 90$ MeV, the instability region gets smaller again. The finite range of the nuclear interaction reduces the binding of matter with k^2, and reduces the spinodal region at large k. The finite B spinodal follows always the $B = 0$ behaviour with the extra contribution of the bands and disconnected regions due to the filling of the Landau levels.

In Fig. 4.2, we show the spinodal sections in the (ρ_p,ρ_n) space obtained with the NL3 parametrization for the magnetic fields $B^* = 2.5 \times 10^2$, $B^* = 2 \times 10^3$, and $B^* = 10^4$, calculated for a wave number $k = 50$ MeV, which gives a spinodal section close to the envelope of

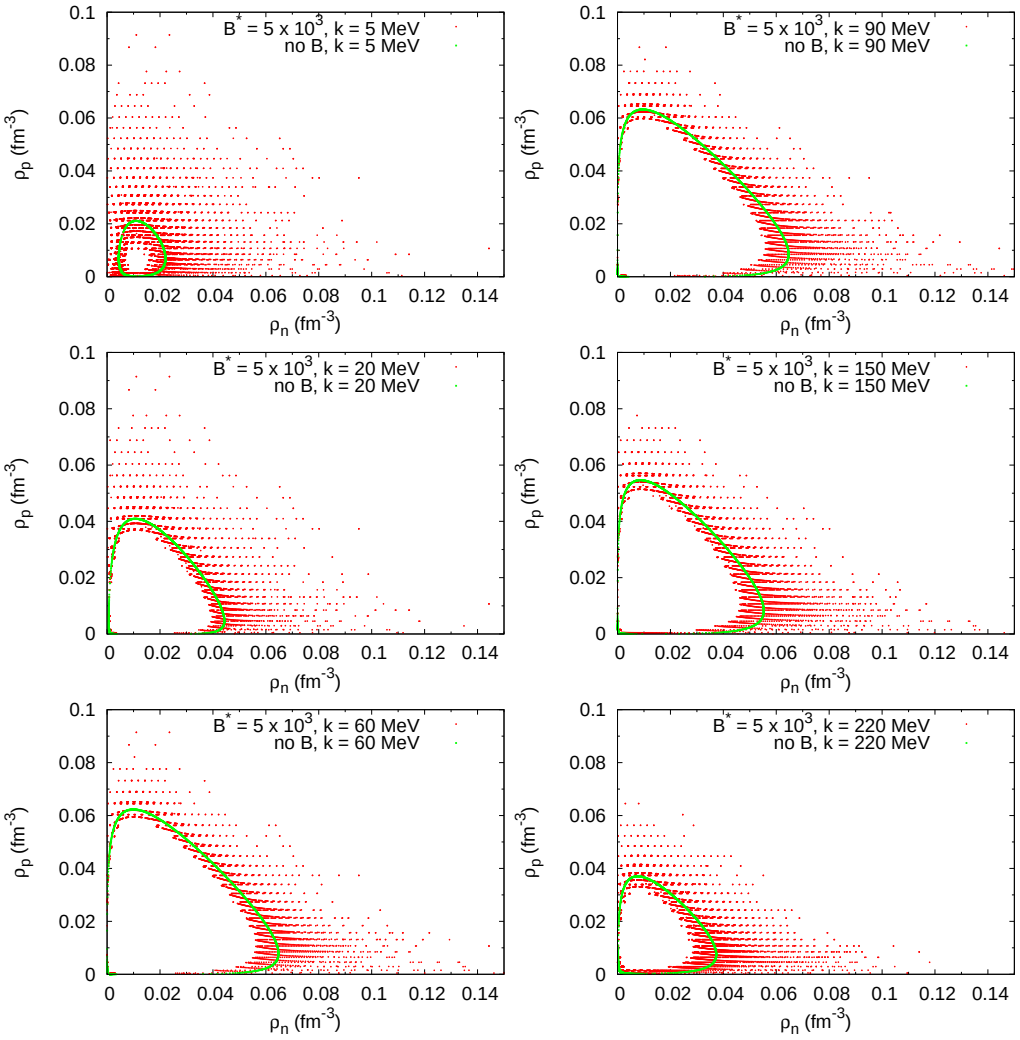

Figure 4.1: Dynamical spinodals attained for different momentum transfers k, for $B^* = 5 \times 10^3$, without AMM, and considering the N-L3 model. The green line represents the corresponding $B = 0$ spinodal section.

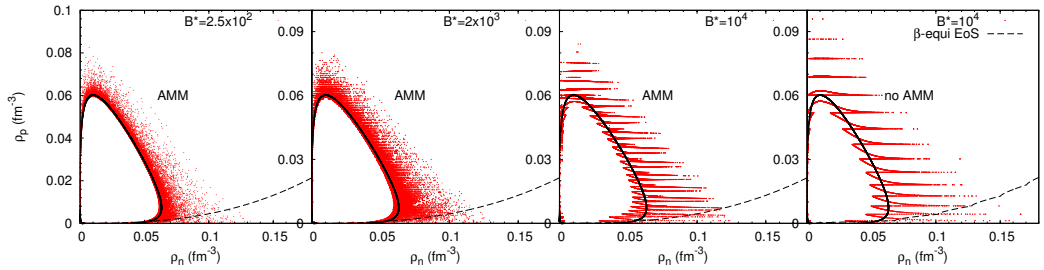

Figure 4.2: Dynamical spinodals for the NL3 parametrization, for different magnetic field intensities and momentum transfer $k = 50$ MeV. The three panels of the right have been obtained including the AMM, while the last panel gives the spinodal not taking into account the AMM of both protons and neutrons.

all spinodal sections, as it was discussed above. In fact, the most intense fields detected on the surface of a magnetar are not larger than 2×10^{15} G, i.e. one or two orders of magnitude smaller than the two more intense fields considered in this study. However, in Refs. [Kiuchi and Yoshida, 2008, Frieben and Rezzolla, 2012], the authors obtained toroidal fields more intense than 10^{17} G in stable configurations, meaning that in the interior of the stars, stronger fields may be expected than the fields measured on the surface.

The calculations were carried out including AMM, except for the largest field, for which we also show the spinodal without AMM, for reference. The thick black line represents the spinodal section for a zero magnetic field.

We have included in this Figure the EoS of β-equilibrium matter represented by a dashed line: the line shows for each neutron density, ρ_n, the respective proton density that satisfies the β-equilibrium condition in neutral matter with electrons, e.g. where $\mu_n = \mu_p + \mu_e$. The intersection between the EoS of β-equilibrium matter and the spinodal section gives a very good estimation of the crust-core transition according to [Avancini et al., 2010].

In the right panel of Fig. 4.2, we can see that a magnetic field $B^* = 10^4$ is strong enough to create bands of instability at densities above 0.05 fm^{-3}, associated with the filling of the different Landau levels. In [Rabhi et al., 2009b], the thermodynamical spinodal section, which corresponds to the $k = 0$ limit of the dynamical spinodal, excluding electrons and the Coulomb field, was studied for magnetic fields equal or above 5×10^{18} G. Spinodal bands are also present, although

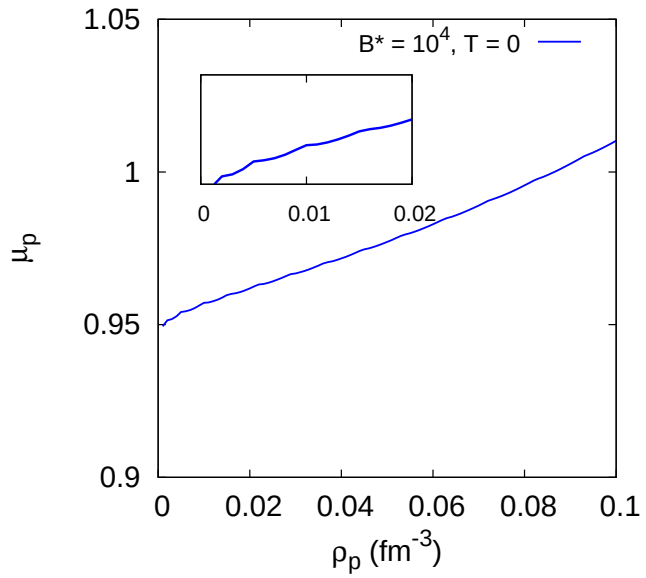

Figure 4.3: The proton chemical potential as a function of the proton density for $B^* = 10^4$, and $T = 0$, with the neutron density fixed at $\rho_n = 0.05$ fm^{-3}.

the stronger the field, the smaller the number of bands. The appearance of bands was attributed to the behavior of the proton chemical potential with density within each Landau band: at the bottom of the band it has a very soft behavior, however, at the top of the Landau level it hardens and a cusp occurs when a new Landau level opens, followed by a softening of the chemical potential.

In order to investigate this process clearly, we plot in Fig. 4.3 the proton chemical potential for $B^* = 10^4$ and $T = 0$ without AMM. It is seen that the proton chemical potential shows many cusps corresponding to the end of a Landau level and the beginning of the following one.

The proton and neutron AMM give rise to extra bands characterized by different spin orientations. The magnetic fields lift the degeneracy between spin up and spin down levels and the level with lower energy is first filled up.

We identify two different contributions for the spinodal section: a) a closed region that contains the $B = 0$ spinodal and extra regions that form spike-like structures, associated with the filling of Landau levels; b) disconnected regions that appear with the opening of new Landau levels at densities well above the $B = 0$ crust-core transition density

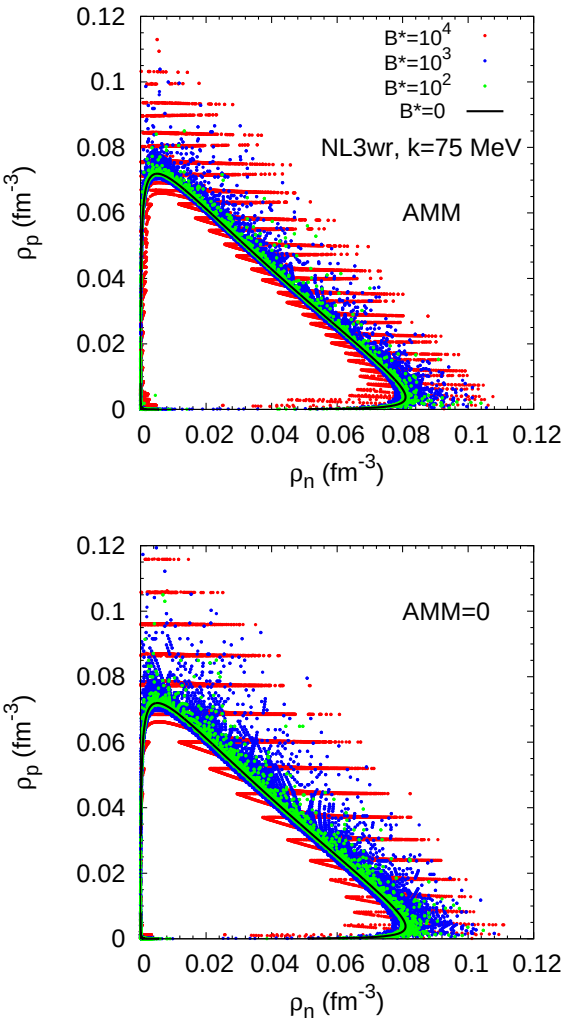

Figure 4.4: Dynamical spinodal for NL3$\omega\rho$, a momentum transfer of $k = 75$ MeV, and $B^* = 10^4$ (red), $B^* = 10^3$ (blue), and $B^* = 10^2$ (green) with (top) and without AMM (bottom). A comparison with the $B = 0$ (black lines) results is also made.

and which do not occur at $B = 0$. The point-like appearance of the sections is a numerical limitation. A higher resolution in (ρ_p,ρ_n) would complete the gaps.

In order to understand the effect of the density dependence of the symmetry energy, we show, in Fig. 4.4, the dynamical spinodal sections obtained with NL3$\omega\rho$, which has the symmetry energy slope at saturation $L = 55$ MeV. In the top panel, the calculations include the AMM,

while in the bottom panel we took AMM$= 0$.

The spinodal sections are plotted for three different values of the magnetic field: $B^* = 10^2$, $B^* = 10^3$, and $B^* = 10^4$. The black lines represent the spinodal section when the magnetic field is zero. The calculations were performed with $k = 75$ MeV, which is a value of the transferred momentum that gives a spinodal section very close to the envelope of the spinodal sections. As above, these sections have been obtained numerically by solving the dispersion relation (3.64) for $\omega = 0$.

First we compare the results obtained omitting the AMM contribution (bottom panel). The structure of the spinodal section obtained for the strongest field considered, $B^* = 10^4$, clearly shows the effect of the Landau quantization: there are instability regions that extend to much larger densities than the $B = 0$ spinodal section, while there are also stable regions that at $B = 0$ would be unstable. This is due to the fact that the energy density becomes softer, just after the opening of a new Landau level, and harder when the Landau level is most filled. The spinodal section has a large connected section at the lower densities and extra disconnected regions. If smaller fields are considered, the structure found for $B^* = 10^4$ is still present, but at a much smaller scale due to the increase of the number of Landau levels, see detail in the inset of the middle panel of Fig. 4.5, for $B^* = 10^3$. It is clear that the spinodal section tends to the $B = 0$ one, as the magnetic field intensity is reduced.

In the top panel of Fig. 4.4, we show the same three spinodal sections, but with the inclusion of the AMM for the protons and neutrons. The overall conclusions taken for the spinodals without the AMM are still valid, although the section acquires more structure when the AMM is included since, for each Landau level, the proton spin up and spin down levels have different energies. This difference originates a doubling of the bands, which are easily identified for $B^* = 10^4$. Besides, these bands are also affected by the neutron AMM. The spinodal sections obtained with AMM are smaller, as it is seen from Fig. 4.5, where, for each field intensity, $B^* = 10^4$ (top), 10^3 (middle), and 10^2 (bottom), the spinodal section without (red) and with (green) AMM are plotted. Although the inclusion of the AMM does not have a very strong effect because the proton and neutron anomalous magnetic moments are small, these effects are not negligible, and, in fact, they reduce the instability sections. In the three panels of Fig. 4.5, we include an inset panel where we have zoomed in the spinodal with AMM in a small range of densities to show that, although in a smaller scale, the structure is similar to the one shown for $B^* = 10^4$.

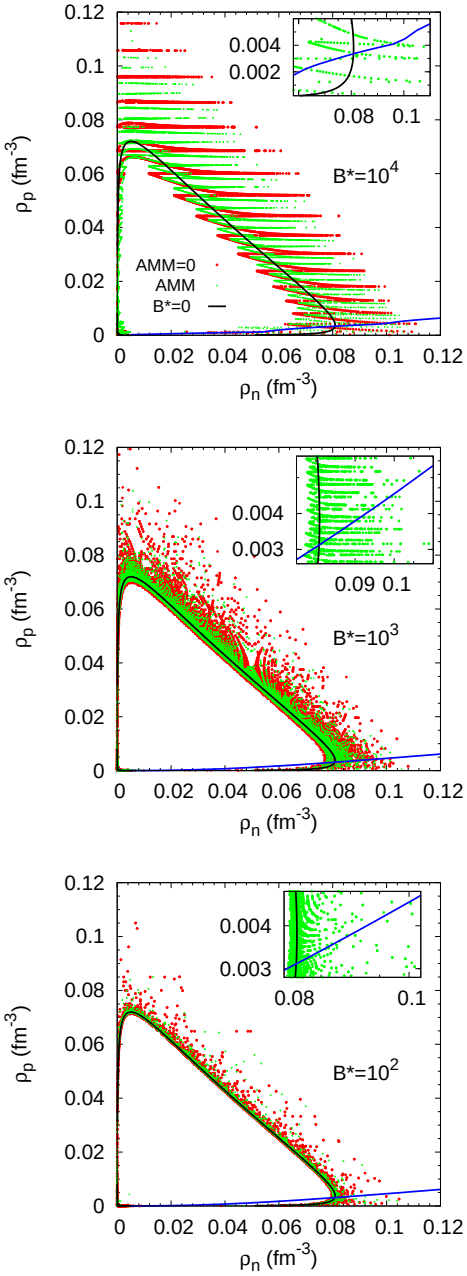

Figure 4.5: Dynamical spinodal for NL3$\omega\rho$, a momentum transfer of $k = 75$ MeV, with AMM (green) and without AMM (red), for $B^* = 10^4$ (top), $B^* = 10^3$ (middle), and $B^* = 10^2$ (bottom). A comparison with the $B = 0$ (black lines) results is also made. The EoS for $\beta-$equilibrium matter is also shown.

For neutron-rich matter, as the one occurring in neutron stars, the instability regions extend to densities almost 40% larger than the crust-core transition density for $B = 0$. The effect of the magnetic field is larger precisely when the proton fraction is smaller. We have included in the three panels of Fig. 4.5 a curve that represents the densities (ρ_p, ρ_n) at β-equilibrium, including the contribution of the AMM. The curves cross an alternation of stable and unstable regions, indicating the existence of a complex crust-core transition, see the insets for detail. The beginning of an homogeneous matter is shifted to larger densities, 0.100 fm^{-3} for $B^* = 10^4$, 0.103 fm^{-3} for $B^* = 10^3$, and 0.105 fm^{-3} for $B^* = 10^2$, corresponding to the pressures 0.818 MeV/ fm^3, 0.833 MeV/ fm^3, and 0.863 MeV/ fm^3, respectively. This complex transition region with a thickness of $\sim$0.02 fm^{-3}, even for the weaker fields, will have strong implications in the structure of the inner crust of magnetars.

4.2 Growth rates

The solution of the dispersion relation inside the spinodal section gives pure imaginary frequencies, indicating that the system is unstable to the propagation of a perturbation with the corresponding wave number in the density range where this occurs. The modulus of the frequency, designated as growth rate, indicates how the system evolves into a two-phase configuration. The evolution will be dictated by the largest growth rate [Chomaz et al., 2004, Providência et al., 2006a].

As an example, in Fig. 4.6, we show the growth rates, $|\omega|$, as a function of the transferred momentum k, for fixed values of the baryonic density: $\rho = 0.04$ fm^3 (top), $\rho = 0.08$ fm^3 (middle), and $\rho = 0.09$ fm^3 (bottom panels), and for the NL3$\omega\rho$ model. We consider a fixed proton fraction of 0.035, which is an average value found for NL3$\omega\rho$ within a Thomas-Fermi calculation of the inner crust [Grill et al., 2012], and we choose the same values for the magnetic field as in the previous figures. The growth rates with (solid) and without (dashed) AMM are plotted together with the growth rate at $B = 0$ (black line).

We first consider $\rho = 0.04$ fm^{-3}, far from the transition to homogeneous matter. The smaller the field, the smaller the effect of the AMM, and for $B^* = 10^2$, the two curves superimpose, and are almost coincident with the $B = 0$ result. The effect of the AMM for the two larger fields is non-negligible, and may go in opposite direction because its behavior is closely related with the filling of the Landau levels. The

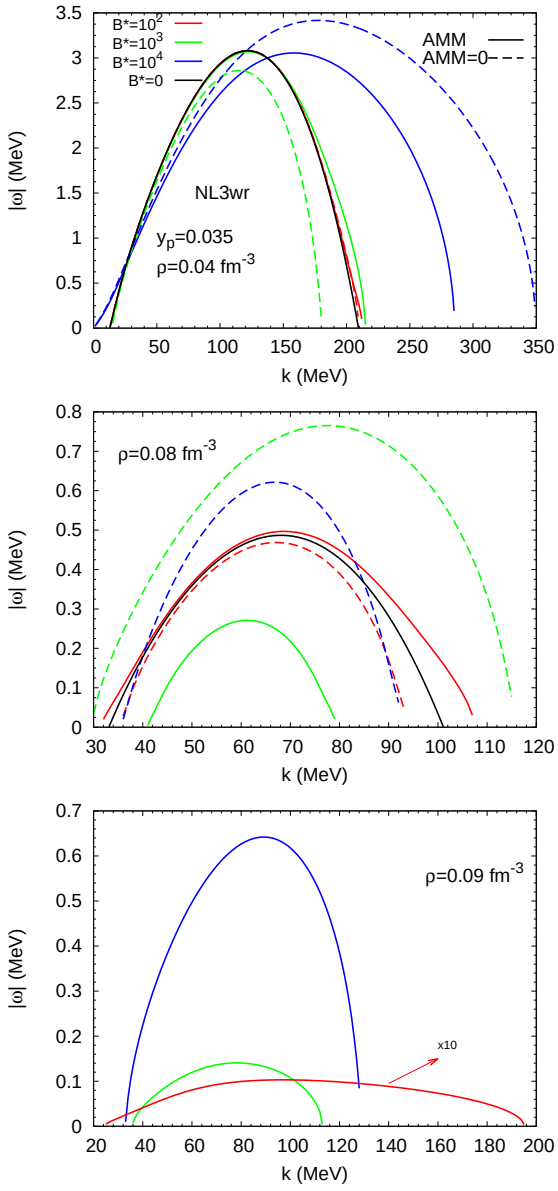

Figure 4.6: Growth rates, $|\omega|$, as a function of the momentum, k, for NL3$\omega\rho$, a proton fraction of $y_p = 0.035$, and $B^* = 10^2$ (red), $B^* = 10^3$ (black), and $B^* = 10^4$ (blue) with AMM (solid) and without AMM (dashed lines), for a fixed baryonic density of $\rho = 0.04$ fm^{-3} (top), $\rho = 0.08$ fm^{-3} (middle), and $\rho = 0.09$ fm^{-3} (bottom). The growth rates for $B^* = 10^2$ in the bottom panel are multiplied by a factor of 10 and are obtained for $\rho = 0.0903$ fm^{-3}.

instability does not exist for the two smaller fields at k close to zero. This is the behavior discussed in Ref. [Providência et al., 2006a] and is directly related to the $1/k^2$ divergence of the Coulomb field. However, for $B^* = 10^4$, and since the electron and proton densities are small, the attractive nuclear interaction is strong enough to drag the electrons, keeping the instability until $k = 0$. This is not anymore the case for the two larger densities considered, because in these two cases, the nuclear interaction is not able to compensate for the larger densities of the charged particles. The stronger nuclear attraction for $B^* = 10^4$ is also observed for the large values of k: the instability is still present for $k > 300$ MeV, well above the maximum k attained for $B = 0$, indicating that the attractiveness of the nuclear force is stronger at short ranges.

The two larger densities have been chosen because they are at the $B = 0$ crust-core transition or above, and this is the most sensitive region to the presence of a strong magnetic field. Due to the alternation between stable and unstable regions, it is highly probable that for one of the field intensities, no instability is present for the particular density value considered. This explains the non appearance of the curve with AMM for $B^* = 10^4$ and $\rho = 0.08$ fm^{-3}. It also explains why the behaviors with and without AMM are so different for $B^* = 10^3$: the value of the density considered picks up the instability region more or less close to the limit of the instability region. In this case, also the maximum growth rates occur for different wave numbers. For $B^* = 10^2$, the results with and without AMM differ, and are not anymore coincident with the $B = 0$ result, as seen for $\rho = 0.04$ fm^{-3}. However, the maximum growth rate occurs at similar wave numbers in the three cases.

Finally, we consider the larger density, $\rho \sim 0.09$ fm^{-3}, approximately 10% above the crust-core transition density $\rho_t = 0.0843$ fm^{-3}, when no field is considered. For $B = 0$, this density belongs to the core, and corresponds to homogeneous matter. However, for the three intensities of the magnetic field we have been considering, $B^* = 10^2, 10^3, 10^4$, this is inside or close to a region of instability. For $B^* = 10^2$, we have taken $\rho = 0.0903$ fm^{-3}, and multiplied the growth rate by a factor of 10 in the figure. We conclude that the growth rates decrease with the magnetic field, showing a convergence to the $B = 0$ result when no instability exists.

4.3 Maximum growth rates

In the present section, we obtain the maximum growth rates, the mode that drives the system into an inhomogeneous phase, for NL3 and NL3$\omega\rho$ models. The determination of the wave length associated with these modes allows an estimation of the size of the clusters formed in the phase transition. On the other hand, the ratio between the corresponding proton and neutron fluctuations indicate how strong is the distillation effect.

To determine the maximum growth rates, we have looked for a given density inside the spinodal section for all eigenmodes with a pure imaginary ω and different wave numbers, and identified the one with the largest $|\omega|$. In this way, we get the mode with the largest growth rate, which is the one that drives the system into a non-homogeneous system formed by clusters immersed in a background neutron-rich gas.

In Fig. 4.7, we show the largest growth rate, the corresponding estimated size of the clusters, and $\delta\rho_p/\delta\rho_n$ changing with the density, for different proton fractions, $y_p = 0.02$, 0.05, and 0.08, and $B^* = 10^3$, with and without AMM. When the proton fraction gets larger, both the number of Landau levels and the maximum of the largest growth rate increase. However, the size of the clusters decreases with an increasing proton fraction. $\delta\rho_p/\delta\rho_n$ increases when the proton fraction gets larger and it is always larger than ρ_p/ρ_n. In this case, the dense phase (clusters) is more symmetric.

In [Avancini et al., 2008], it was also shown that for NL3 the average proton fraction in the inner crust, for densities above 0.01 fm^{-3}, is $y_p \sim 0.02$, while for NL3$\omega\rho$ is $y_p = 0.035$. In the following, we will, therefore, determine the most unstable modes for magnetized matter for both parametrizations at fixed proton fraction, taking these proton fractions, and will estimate the size and separation of charge content of the clusters formed in the inner crust, originated by the clusterization. As in Ref. [Providência et al., 2006a], we will consider that half wavelength of the maximum growth rate mode is a good estimation of the order of magnitude of the size of the clusters which are formed. In fact, in Ref. [Avancini et al., 2008] it was shown that the size of the clusters obtained within a Thomas-Fermi calculation compare well with the half-wave length associated with the most unstable mode. These quantities are plotted in Figs. 4.8, 4.10, and 4.11.

In Fig. 4.8, the largest growth rates (top panels), the corresponding half-wave length (middle panels), and the ratio $\delta\rho_p/\delta\rho_n$ between the proton and neutron density fluctuations (bottom panels) are shown for

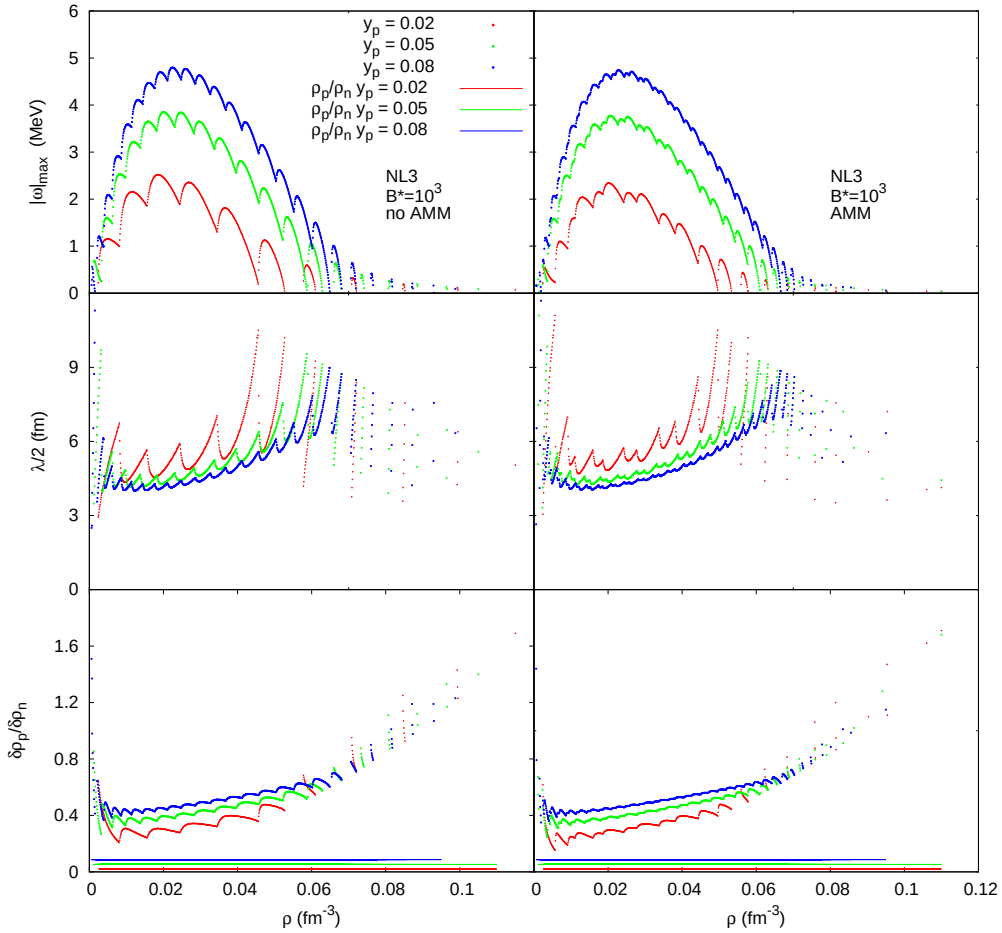

Figure 4.7: Largest growth rate (top), the corresponding estimated size of the clusters (middle), and the density fluctuation ratio $\delta\rho_p/\delta\rho_n$ (bottom) versus density, for different proton fractions y_p, and $B^* = 10^3$, with (right) and without (left) AMM, for the NL3 model.

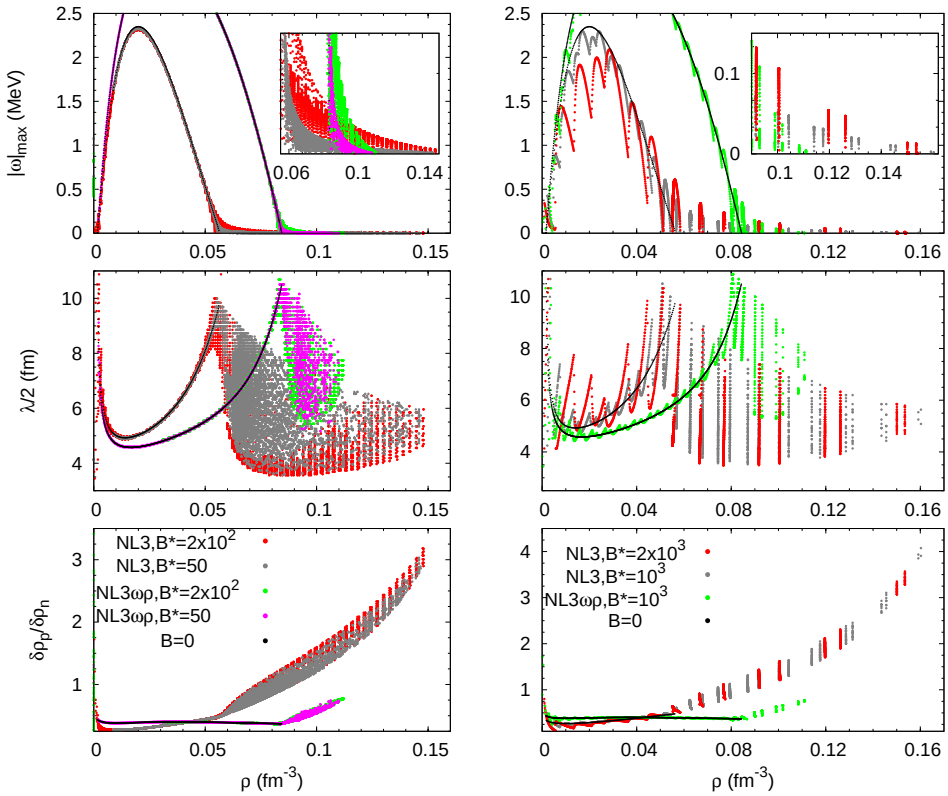

Figure 4.8: Largest growth rate $\Gamma = |\omega|$ (top panels), the corresponding half-wavelength (middle panels) and the proton-neutron density fluctuation ratio (bottom panels) versus density, for different magnetic field intensities and matter with $y_p = 0.02$ for NL3 and $y_p = 0.035$ for NL3$\omega\rho$. The black curve corresponds to the $B = 0$ results.

fields between $B^* = 50$ and $B^* = 2\times10^3$ for NL3 and NL3$\omega\rho$, at constant proton fraction. In all panels, the $B = 0$ results are represented by a black curve. In the top panels, we can see very clearly that there is a closed region that, although with some fluctuations, follows the $B = 0$ curve, followed by separate regions, whose density width decreases continuously until homogeneous matter sets in. These disconnected regions appear when a new Landau level starts being filled.

Let us first consider the strongest field, represented by red dots in the right panel of Fig. 4.8, obtained only for NL3. In this case, there are several well defined regions of clusterized matter separated by regions of homogeneous matter. This is a consequence of the bands of instability, due to the filling of the Landau levels. Also, the size of the clusters

is affected. In the first region of instability, the size of the clusters oscillates around the results for $B = 0$, and fast size changes occur in a very small density interval. After the first instability region, several others appear, although the larger the density, the smaller the density width of each region. Considering weaker fields, all these features are repeated with a denser appearance of unstable regions but with smaller widths each. The transition density to homogeneous matter is changing slowly with the magnetic field intensity, but considering sufficiently small fields, the finite B spinodal converges to the $B = 0$ one, as discussed before.

This convergence is reflected on the decrease of the magnitude of the growth rate at a density 10% larger than the $B = 0$ crust-core transition density with a decrease of the magnetic field: for NL3 (NL3$\omega\rho$), it goes from 0.3855 (0.1481) MeV at $B^* = 10^3$, to 0.0921 (0.0378) MeV for $B^* = 2 \times 10^2$, and 0.0068 (0.0020) MeV for $B^* = 10$.

The extension of the region with disconnected unstable regions is strongly dependent on the density dependence of the symmetry energy: for the NL3$\omega\rho$ parametrization with $L = 55$ MeV, the unstable region extends only until $\rho = 0.113$ fm^{-3}. This increases to $\rho \sim 0.12, 0.13, 0.16$ fm^{-3} for $L = 68, 88, 118$ MeV, respectively , and stellar matter conditions. Taking a larger proton fraction, $y_p = 0.1$, which may be more realistic at larger densities, there will still appear unstable regions for $\rho \leq 0.11$ fm^{-3} for NL3$\omega\rho$, with $L = 55$ MeV, and $\rho \leq 0.135$ fm^{-3} for NL3, with $L = 118$ MeV.

The proton-neutron density fluctuation ratio was also calculated. Although $y_p = 0.02$ corresponds to $\rho_p/\rho_n = 1/49$, the fluctuations give rise to clusterized matter with a much larger proton content: above the $B = 0$ crust-core transition density, the fluctuations $\delta\rho_p/\delta\rho_n$ increase from ~ 0.35 to more than the double for NL3$\omega\rho$, and a factor of 5 for NL3, see both panels of Fig. 4.8.

The joint effect of B and L on the thickness of the crust is summarized in the following: a) the larger the L, the larger the effect of B, mainly due to the proton fraction associated with each model, since a larger L is associated with a smaller proton fraction; b) compared to $B = 0$, the effect can be as large as a 100% for $L = 118$ MeV. However, experimental contraints [Tsang et al., 2012], and microscopic neutron matter calculations [Hebeler et al., 2013, Gandolfi et al., 2012], indicate that the models with $L = 30 - 80$ MeV are more realistic. For $L = 55$ MeV, the effect corresponds to an increase of $\sim 20\%$; c) taking $L = 55$ MeV and decreasing the magnetic field by an order of magnitude from $B^* = 10^3$ to $B^* = 10^2$, the transition density suffers a reduction of

$\sim 3-5\%$, but is still larger than the corresponding value at $B=0$.

In [Rabhi et al., 2009a], an interesting feature related to the extension of the thermodynamical spinodal for zero proton fraction with magnetic field in the absence of the AMM was discussed. For $\rho_p = 0$, and in the absence of the magnetic field, there is no instability, e.g. pure neutron matter does not present liquid-gas like instabilities. However, the inclusion of the magnetic field changes this behavior: the instability region at $\rho_p = 0$ extends until a finite ρ_n value, independent of B. This value is ~ 0.213 fm^{-3} for NL3, shown in Fig. 4.9. On the other hand, the inclusion of AMM will change this feature: ρ_n is still finite for $\rho_p = 0$, but the value depends on the magnetic field.

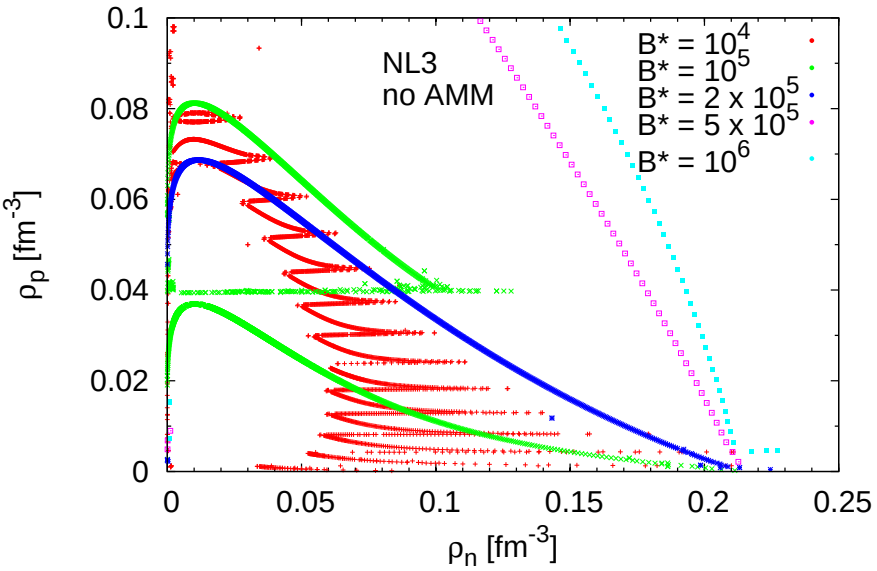

Figure 4.9: Thermodynamical spinodals for different values of magnetic fields in the absence of the AMM for the NL3 model. All sections extend to the same point at $\rho_p = 0$.

To understand this feature, we consider the determinant of the energy curvature matrix Det($\mathcal{F}$), which is related with the presence of the instability region, and consider $\rho_p = 0$ matter. In this extreme case, Det($\mathcal{F}$) increases monotonically with the density, and the equation Det($\mathcal{F}$) $= 0$ indicates the end of the instability region. The neutron densities, where Det($\mathcal{F}$) $= 0$ in this extreme case, are the limit of the instability region, theoretically. We obtain the corresponding finite val-

ue of $\rho = \rho_n = \dfrac{P_F^{n3}}{3\pi^2}$ from the Fermi neutron momenta P_F^n solution of the equation $\mathrm{Det}(\mathcal{F}) = 0$ with $\rho_p = 0$. Explicitly, the latter equation can be written as follows

$$\left(\mathcal{A}_+ - \frac{\mathcal{C}}{M^{*2}}\right)\left(\frac{\pi^2}{\epsilon_F^n P_F^n} + \mathcal{A}_+ - \frac{\mathcal{C}}{\epsilon_F^{n2}}\right) - \left(\mathcal{A}_- - \frac{\mathcal{C}}{M^*\epsilon_F^n}\right)^2 = 0, \tag{4.1}$$

where

$$\mathcal{A}_\pm = \left(\frac{g_v}{m_v}\right)^2 \pm \frac{1}{4}\left(\frac{g_\rho}{m_\rho}\right)^2, \tag{4.2}$$

$$\epsilon_F^n = \sqrt{P_F^{n2} + M^{*2}}, \tag{4.3}$$

$$\mathcal{C} = \left(\frac{g_s}{m_s}\right)^2 \frac{M^{*2}}{\mathcal{K}}, \tag{4.4}$$

with

$$\mathcal{K} = 1 + \left(\frac{g_s}{m_s}\right)^2 \left[\frac{\kappa}{g_s^2}\phi + \frac{\lambda}{2g_s^2}\phi^2 + \frac{1}{2\pi^2\epsilon_F^n}\left(P_F^{n3} + 3M^{*2}P_F^n - 3M^{*2}\epsilon_F^n \log\left|\frac{P_F^n + \epsilon_F^n}{M^*}\right|\right)\right]. \tag{4.5}$$

This equation is independent of the magnetic field and, therefore, all the spinodal regions for different magnetic fields without AMM have the same value of ρ_n for $\rho_p = 0$.

The border to homogeneous matter at $\rho_n^{NL3} = 0.213$ fm^{-3} sets an upper limit of the extension of the dynamical spinodal, which in fact is too high, because matter in the stars has a finite proton fraction: for NL3 (NL3$\omega\rho$) and the proton fraction at the crust-core transition, $y_p^{NL3} = 0.02$ ($y_p^{NL3\omega\rho} = 0.035$), the dynamical spinodal extension is reduced to $\rho \sim 0.16$ (0.115) fm^{-3} for $B = 4.4 \times 10^{16}$ G. Decreasing further the magnetic field to 2.2×10^{14} G, the extension of the spinodal decreases to 0.105 fm^{-3} for NL3, and 0.102 fm^{-3} for NL3$\omega\rho$, showing a convergence to the $B = 0$ result, 0.056 and 0.084 fm^{-3}, respectively.

There are several questions that can be raised with the previous calculation: 1) how important is the inclusion of the AMM? 2) does it make sense to consider the whole calculation of the maximum growth rates at a constant proton fraction, or should this restriction be taken only until the $B = 0$ crust-core transition density, and above this density, the β-equilibrium fraction should be chosen? In order to answer the first question, in the following, we will compare two calculations done under the same conditions, except for the AMM. An exact answer to the second question demands a calculation of the EoS of clusterized

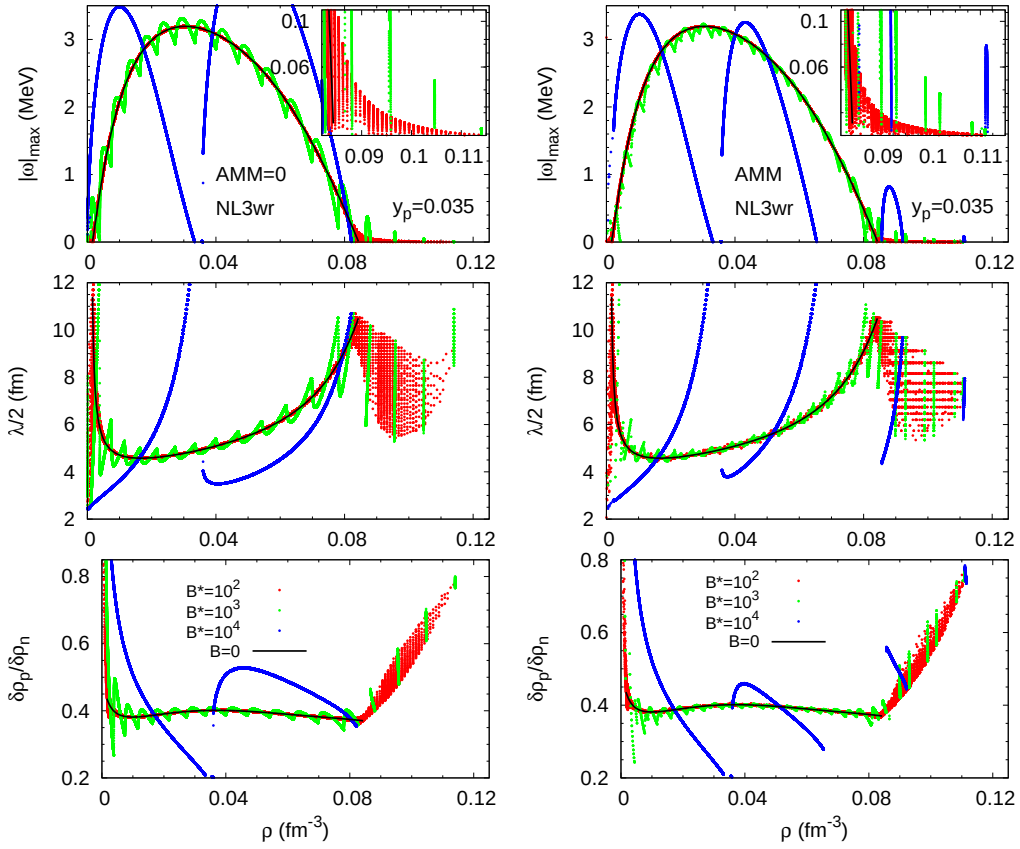

Figure 4.10: Largest growth rate (top panels), the corresponding half-wavelength (middle panels), and the proton-neutron density fluctuation ration (bottom panels) versus density for NL3$\omega\rho$, with a proton fraction of $y_p = 0.035$ for the whole density range, without (left panels) and with (right panels) AMM. Three different values of B are considered: $B^* = 10^2$ (red), $B^* = 10^3$ (green), and $B^* = 10^4$ (blue). A comparison with the $B = 0$ (black lines) results is also made.

matter under a strong magnetic field. Since this is not the objective of the present study, we will consider an alternative scenario: the constant proton fraction is taken only until the $B = 0$ crust-core transition density, and, above this density, the β-equilibrium fraction is considered. This is the behavior of the EoS of stellar matter obtained from an unified inner crust-core calculation [Grill et al., 2012].

In Fig. 4.10, the largest growth rates (top panels), the corresponding half-wave length (middle panels), and the $\delta\rho_p/\delta\rho_n$ ratio are shown for three different magnetic field intensities, $B^* = 10^2, 10^3$, and 10^4. In this figure, all results were obtained with a fixed proton fraction, $y_p = 0.035$. The calculation including the AMM of protons and neutrons presents twice as much unstable regions, as compared with the AMM$= 0$ case, due to the separation of each proton Landau level in two, with a different spin polarization. Only the first region, occuring at the lowest densities, does not suffer a doubling, because it is associated with totally polarized (spin up) protons. For the two lowest magnetic field intensities, the extension of the transition to the core decreases. However, for $B^* = 10^4$, the AMM extends the instability region to a larger density, just because the third Landau level was pushed to a lower density. It should be stressed that although the differences originated by the AMM decrease when the magnetic field intensity decreases, the effect is still visible for $B^* = 10^2$, a field below 10^{16} G.

More information on the properties of this range of densities is obtained from the middle and bottom panels. In the middle panel, the half-wave length of the perturbation is plotted, and it gives an estimation of the size of the cluster that will be formed. Within each of these independent unstable regions, the cluster size changes from about 9 fm to about 4 fm in a very narrow density range. Finally, the bottom panel gives some information on the proton content of the dense phase: the clusters will be quite proton rich with a proton-neutron density fluctuation ratio well above the 0.04 ratio of the homogeneous matter, and more proton rich than clusters formed in non-magnetized matter.

The effect of considering above the $B = 0$ crust-core transition the proton fraction dictated by the β-equilibrium condition imposed to magnetized matter is illustrated in Fig. 4.11, which shows the same quantities plotted in the previous figure. In grey, we show the results with a fixed proton fraction of 0.035 for the whole range of densities, and in blue we take, above the $B = 0$ crust-core transition density, the proton fraction as the one found in $\beta-$equilibrium matter, and below a fixed proton fraction of 0.035. Taking the β-equilibrium proton fraction, instead of the fixed 0.035 above the crust-core $B = 0$ transition, has a

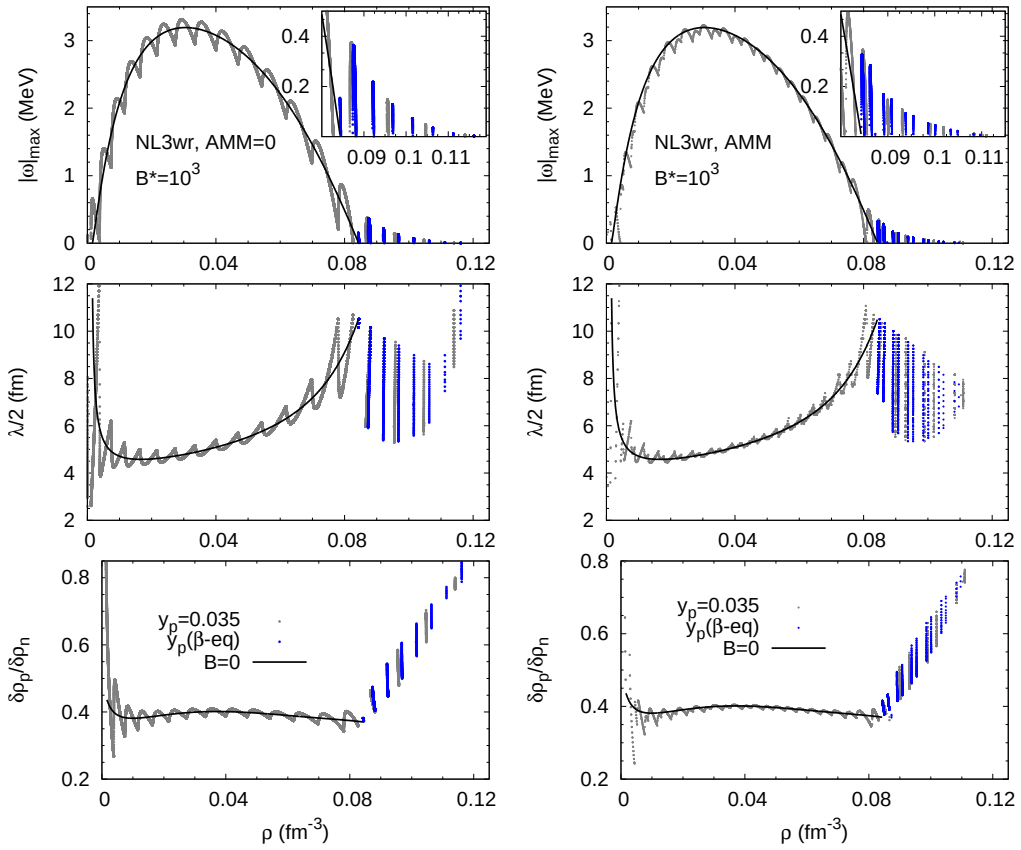

Figure 4.11: Largest growth rate (top panels), the corresponding half-wavelength (middle panels), and the proton-neutron density fluctuation ratio (bottom panels) versus density for NL3$\omega\rho$, and a magnetic field of $B^* = 10^3$, without (left panels) and with (right panels) AMM. Results with the $B = 0$ (black solid lines) calculation are also shown for comparison. The blue points correspond to a calculation with a proton fraction equal to the one found in $\beta-$equilibrium matter, above $\rho_t = 0.0843$ fm^{-3}, the $B = 0$ crust-core transition density. The grey points correspond to a fixed proton fraction of 0.035 in the whole density range.

non-negligible effect, and, in fact, reduces the instability region, because the β-equilibrium condition predicts larger proton fractions, and the larger the proton densities, the smaller the effects due to the magnetic field. In particular, for $B^* = 10^4$, ρ_2 is ~ 0.01 fm^{-3} smaller, taking $y_p^{\beta-eq}$ instead of $y_p = 0.035$. This difference is ~ 0.005 fm^{-3} for $B^* = 10^2$, and ~ 0.002 fm^{-3} for $B^* = 10^3$. The discrete feature of the Landau levels results in a non-monotonic behavior of this quantity for the larger values of B.

4.3.1 Thickness of the crust

The effect that was already identified with the spinodal sections is clearly shown in Fig. 4.10 and 4.11: the unstable regions occur well beyond the $B = 0$ crust-core transition at 0.0843 fm^{-3}, and extend until $\rho_t = 0.11$ fm^{-3}, 40% larger than the $B = 0$ transition density. However, above 0.082 fm^{-3}, the unstable regions alternate with stable ones. The transition densities that define the limits of the region of alternating stable and unstable regions have been labelled ρ_1 and ρ_2, and are shown in Table 4.1. The transition density ρ_1 defines the first time $|\omega|$ goes to zero, and the density ρ_2 defines the onset of the homogeneous matter, meaning that we have a range of densities between ρ_1 and ρ_2 where unstable and stable regions alternate. At $B = 0$, both densities coincide, i.e. $\rho_1 = \rho_2$.

Since it makes a difference the way we choose the proton fraction, to determine the density ρ_2 we have considered the $\beta-$equilibrium matter proton fraction above the $B = 0$ crust-core transition, and ρ_1 is calculated with the fixed $y_p = 0.035$ proton fraction, obtained from the $B = 0$ calculations of the pasta phases, since ρ_1 is a density that lies at or below the $B = 0$ crust-core transition.

Besides ρ_1 and ρ_2, in Table 4.1, we also give the pressure at these two densities and the fractional moment of inertia of the crust, a quantity that depends directly on the pressure and density at the crust-core transition, and that has an important impact in explaining pulsar glitches. In Table 4.1, the crust thickness, $\Delta R = R(0) - R(\rho_2)$, the thickness of the region between ρ_1 and ρ_2, $\Delta R' = R(\rho_1) - R(\rho_2)$, and the difference between the crust thicknesses at $B = 0$ and $B \neq 0$, $\Delta R_B = \Delta R - \Delta R(B = 0)$, are also displayed. These results take into account the AMM, and they have been calculated for a star with $M = 1.4$ M$_\odot$, and a radius of $R = 13.734$ km for the NL3$\omega\rho$ model. For the calculation of the fractional moment of inertia of the crust, we took for P_t and ρ_t the values of P_2 and ρ_2, given in the Table for each magnetic field.

Table 4.1: Transition densities and pressures for the magnetic fields considered in this study, together with the correspondent fractional moment of inertia of the neutron star crust, for NL3$\omega\rho$, with $L = 55$ MeV, for a star of $M = 1.4$ $M_\odot$ and $R = 13.734$ km. Also shown are the crust thicknesses, ΔR, the thickness due to the inhomogeneous region found when $B \neq 0$, $\Delta R' = R(\rho_1) - R(\rho_2)$, and the difference to the $B = 0$ result, $\Delta R_B = \Delta R - \Delta R(B = 0)$. The results shown take into account the AMM. The transition densities are calculated when $|\omega| = 0$ (see top panels of Figs. 4.10 and 4.11, and the text for more details). The values for ρ_2 correspond to the calculations with a $\beta-$equilibrium matter proton fraction.

B^*	ρ_1 (fm^{-3})	ρ_2 (fm^{-3})	P_1 $\left(\frac{\mathrm{MeV}}{\mathrm{fm}^3}\right)$	P_2 $\left(\frac{\mathrm{MeV}}{\mathrm{fm}^3}\right)$	ΔR (m)	$\Delta R'$ (m)	ΔR_B (m)	$\frac{\Delta I_{cr}}{I}$
0	0.0843	0.0843	0.5196	0.5196	1368	0	0	0.0676
10^2	0.0837	0.1044	0.5119	0.8541	1551	185	182	0.0968
10^3	0.0808	0.1096	0.4758	0.9743	1609	257	240	0.1056
10^4	0.0654	0.0998	0.3274	0.8095	1503	260	134	0.0922

Our results for $B = 0$ agree with the transition densities and pressures and the moment of inertia of the crust obtained in Ref. [Fattoyev and Piekarewicz, 2010], see tables I and IV. This is expectable, since the same expression for the crustal moment of inertia has been used, as in Refs. [Worley et al., 2008, Lattimer and Prakash, 2000].

The magnetic field gives rise to larger values of the crust-core transition pressure and density, and these affect directly $\Delta I_{cr}/I$. These values are much higher than the prediction in Ref. [Link et al., 1999, Andersson et al., 2012] for the Vela pulsar, 0.016, when no entrainment effects are considered, and they would be high enough for the crust to completely describe the glitch mechanism, even taking into account the effect of entrainment [Andersson et al., 2012, Chamel et al., 2013]. In fact, in this case, the "effective" moment of inertia associated with the fluid is lowered, and the constraint inferred from glitches requires that the crustal moment of inertia is $\langle m_n^* \rangle / m_n \sim 4 - 6$ larger [Andersson et al., 2012], where m_n^* is the effective neutron mass including entrainment, and m_n the bare neutron mass. To explain the Vela glitches, this constraint would be equivalent to requiring a fractional crustal moment of inertia $\sim 0.064 - 0.096$.

4.3.2 Final comments

The properties discussed above indicate that at the crust-core transition, matter is very complex, and that the magnetic field favors a large charge concentration in the clusters. Even considering matter below the $B = 0$ crust-core transition, the present calculation indicates that there is a fast change of the cluster size. This change will probably cause the cluster size and structure to change more strongly with density than it would be expected for $B = 0$, giving rise to more heterogeneous matter.

Simulations of the time evolution of the magnetic field at the crust have shown that the existence of amorphous and heterogeneous matter deep in the inner crust, with a high impurity parameter and, therefore, highly resistive, favors a fast decay of the magnetic fields. This has been proposed as an explanation for the non-observation of x-ray pulsars with a period above 12 s [Pons et al., 2013].

In summary, we have studied the effect of strong magnetic fields, of the order of $10^{15} - 10^{17}$ G, on the extension of the crust of magnetized neutron stars. It was shown that a strong magnetic field has a large effect on the instability region, defining the crust-core transition as a succession of stable and unstable regions due to the opening of new Landau levels. The effect of the anomalous magnetic moment is non-negligible for fields larger than 10^{15} G. The complexity of the crust at the transition to the core, and the increase of the crust thickness, may have direct impact on the properties of neutrons stars related with the crust, in particular, the glitch mechanism and the non-existence of pulsars with a period above 12 s.

Chapter 5

Thermodynamical spinodal

In this chapter, we first compare the predictions obtained from the dynamical and the thermodynamical spinodals, and, then, we analyze the effect of the temperature on the thermodynamical spinodal section, and draw some comments on the effect of the temperature on the extension of the crust. Most of the discussion is performed for NL3$\omega\rho$, since the value of L of this model is more compatible with the present experimental data than NL3.

5.1 Thermodynamical versus dynamical spinodal

In the present section, we briefly compare the thermodynamical and dynamical spinodals of strongly magnetized nuclear matter. In Ref. [Avancini et al., 2006], it has been shown that due to the large incompressibility of the electron gas, most models that describe npe matter do not present thermodynamical instabilities, or present only a very reduced region of instabilities. However, thermodynamical stability does not necessary mean that the npe system is stable to small density fluctuations, as shown in [Pethick et al., 1995, Providência et al., 2006a, Brito et al., 2006]. The calculation of the dynamical spinodal allows a quite good prediction of the instability region taking into account the independent fluctuations of the neutron, proton and electron densities.

According to [Avancini et al., 2010, Ducoin et al., 2011], the np matter thermodynamical spinodal gives a good prediction of the crust-core transition density, just slightly above the prediction from a Thomas-Fermi calculation or a dynamical spinodal for npe matter.

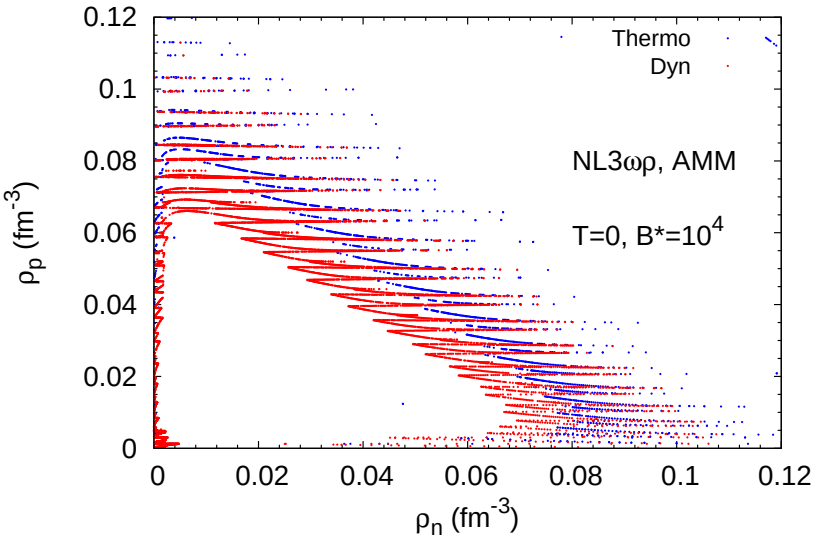

Figure 5.1: The dynamical and thermodynamical spinodals for $B^* = 10^4$ and $T = 0$ MeV for the NL3$\omega\rho$ model with AMM.

In order to understand which are the limitations of this procedure, in Fig. 5.1, we compare the results obtained for the crust-core transition at $T = 0$ and $B^* = 10^4$ with the npe dynamical spinodal, and the np thermodynamical spinodals, both calculations taking into account the AMM. The values predicted from the thermodynamical spinodal are always $\sim 15\%$ larger than the ones from the dynamical spinodal. Having this property of the thermodynamical spinodal in mind, in the following, we will use the finite temperature np thermodynamical spinodal to study the possible effect of temperature on the crust-core transition in the presence of a strong magnetic field.

5.2 Thickness of the crust within the thermodynamical spinodal

Before discussing the effect of the temperature on the crust, we determine the size of the crust at $T = 0$ using the thermodynamical spinodal. We will also show the effect of the density dependence of the symmetry energy, and, in particular, calculate the thickness difference obtained with the thermodynamical and the dynamical spinodal sections.

In order to get the thickness of the crust and of the transition region

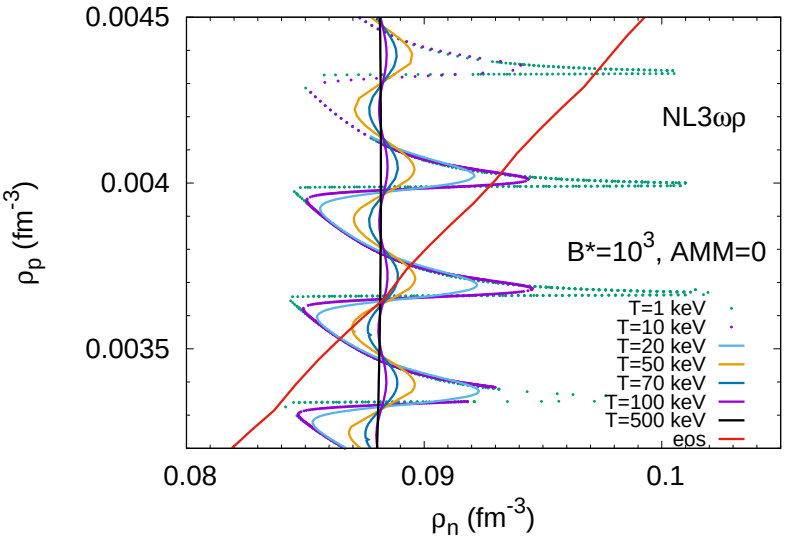

Figure 5.2: Details of the crossing of the thermodynamical spinodal with the EoS (red solid line) for NL3$\omega\rho$ with $B^* = 10^3$, considering different temperatures, and taking AMM$= 0$.

we determine the lower and upper transition densities from the crossing of the β-equilibrium EoS and the spinodal section. This is illustrated in Fig. 5.2: the lower (upper) density ρ_1 (ρ_2) corresponds to the density where the β-equilibrium EoS first (last) crosses the spinodal. In this figure, the thermodynamical spinodal, calculated at $B^* = 10^3$ and several temperatures, has been used to determine the crust-core transition. Below $T = 10$ keV, the effect of temperature is almost negligible, but at $T = 100$ keV, the temperature has washed out most of the effect of the magnetic field. In the next subsection, we will come back to this point.

We first compare the dynamical and thermodynamical approaches at $T = B = 0$. In Table 5.1, we show the results obtained within both formalisms at $B = 0$, and for $T = 0$, for models from the NL3 family, with $L = 55, 68, 88,$ and 118 MeV, which are obtained by choosing adequately the couplings of the ρ-meson and the non-linear $\omega\rho$ term.

For $L = 55$ MeV, we observe that the effect of using the thermodynamical, instead of the dynamical, spinodal is an increase of 7 m in the crust thickness, together with an increase of 18% of the pressure at the crust-core transition, which gives rise to a 13% larger fractional crustal moment of inertia. For $L = 118$ MeV, on the other hand, the crust gets

142 m larger, and the fractional crustal moment of inertia almost 30% larger. In the following, we will always consider $L = 55$ MeV.

Table 5.1: Transition densities and pressures calculated within the thermodynamical and dynamical spinodals formalism at $B = T = 0$, and considering four different values of L, with the correspondent fractional moment of inertia of the neutron star crust, for a star of $M = 1.4$ $M_\odot$. Also shown are the crust thicknesses, ΔR, and the radius of a 1.4 solar mass star, $R_{1.4}$.

L (MeV)	ρ $\left(\frac{1}{\text{fm}^3}\right)$	P $\left(\frac{\text{MeV}}{\text{fm}^3}\right)$	$R_{1.4}$ (km)	ΔR (m)	$\frac{\Delta I_{cr}}{I}$
Thermodynamical					
118	0.0647	0.423	14.631	1467	0.067
88	0.0749	0.592	14.256	1586	0.077
68	0.0856	0.704	13.927	1603	0.083
55	0.0919	0.628	13.734	1432	0.078
Dynamical					
118	0.056	0.258	14.631	1325	0.048
88	0.063	0.355	14.256	1395	0.055
68	0.074	0.503	13.927	1450	0.066
55	0.084	0.520	13.734	1368	0.068

We now compare the predictions of both methods for a finite magnetic field.

In Table 5.2, we give the the transition densities, ρ_1 and ρ_2, and respective pressures, the crust thickness ΔR, the thickness of the transition region $\Delta R'$, given by $R' = R(\rho_1) - R(\rho_2)$, and the crust fractional momentum of inertia calculated with (ρ_2, P_2), considering the $L = 55$ MeV model at $T = 0$ for several values of B^* using the thermodynamical spinodal formalism without and with AMM. The quantities (ρ_1, ρ_2), the total crust thickness ΔR, and the fraction of momentum of inertia of the neutron star crust $\Delta I_{cr}/I$ are plotted in Fig. 5.3 as a function of B^*.

The main conclusions that can be drawn for the field intensities considered are: a) the dynamical and thermodynamical spinodals with AMM predict the same trends for the transition densities, though the dynamical spinodal predicts smaller values of ρ_1, in accordance with the results from [Avancini et al., 2010, Ducoin et al., 2011]. However,

Table 5.2: Transition densities and pressures calculated at $T = 0$ within the formalism of the thermodynamical spinodal with and without AMM, for $50 < B^* < 10^4$ and $L = 55$ MeV, together with the correspondent fractional moment of inertia of the neutron star crust, for a star of $M = 1.4$ $M_\odot$ and $R = 13.734$ km. Also shown are the crust thicknesses, ΔR, the thickness due to the inhomogeneous region found when $B \neq 0$, $\Delta R' = R(\rho_1) - R(\rho_2)$, and the difference to the $B = 0$ result, $\Delta R_B = \Delta R - \Delta R(B = 0)$.

B^*	ρ_1 $(\frac{1}{\text{fm}^3})$	ρ_2 $(\frac{1}{\text{fm}^3})$	P_1 $(\frac{\text{MeV}}{\text{fm}^3})$	P_2 $(\frac{\text{MeV}}{\text{fm}^3})$	ΔR (m)	$\Delta R'$ (m)	ΔR_B (m)	$\frac{\Delta I_{cr}}{I}$
				AMM				
10^2	0.0909	0.0967	0.613	0.708	1474	51	105	0.085
10^3	0.0886	0.1145	0.580	1.101	1665	262	297	0.114
10^4	0.0688	0.1369	0.357	1.952	1981	713	612	0.159
				AMM=0				
50	0.0908	0.0967	0.610	0.706	1473	52	105	0.085
100	0.0907	0.1009	0.610	0.785	1514	93	145	0.091
200	0.0893	0.1065	0.589	0.9015	1574	165	206	0.100
500	0.0874	0.1163	0.562	1.150	1693	299	325	0.118
10^3	0.0900	0.1162	0.599	1.1481	1686	271	317	0.118
10^4	0.0839	0.1075	0.521	0.9484	1584	218	216	0.103

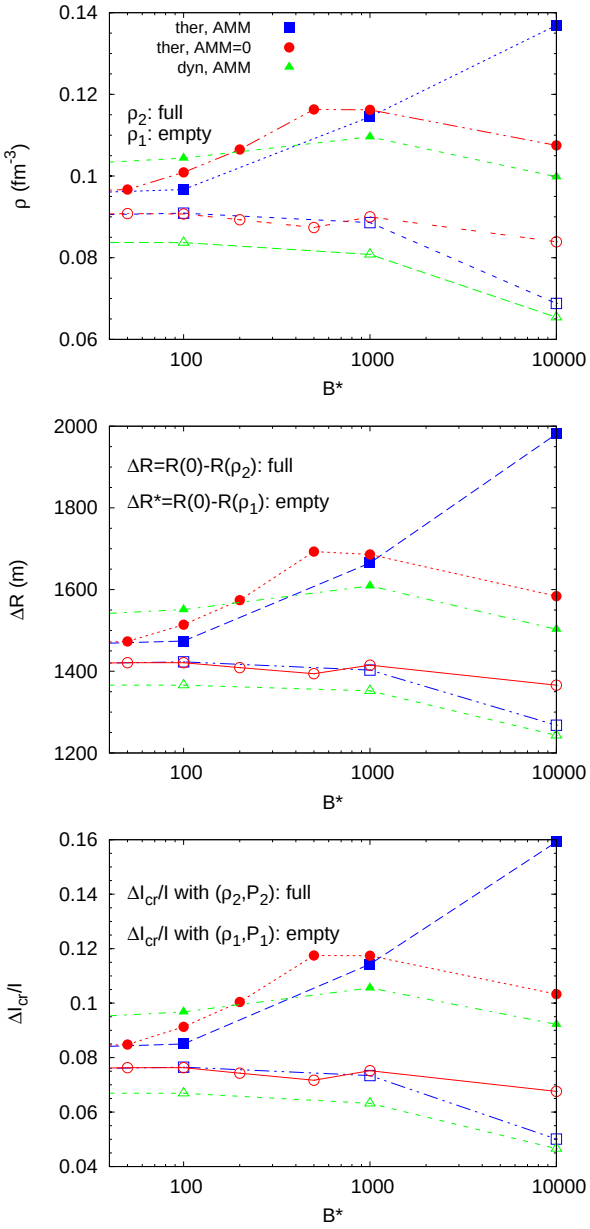

Figure 5.3: The transition densities, ρ_1 (empty) and ρ_2 (full), (top), the crust thickness, ΔR (full) and $\Delta R^* = R(0) - R(\rho_1)$ (empty), (middle), and the crust fractional momentum of inertia (bottom), calculated with (ρ_1, P_1) (empty) and with (ρ_2, P_2) (full), obtained with the $L = 55$ MeV model, at $T = 0$, for several values of B^*, and using the thermodynamical spinodal formalism with (squares) and without AMM (circles), and the dynamical spinodal with AMM (triangles).

for the upper limit of the transition region, there is a dependence on B, and the dynamical ρ_2 is larger (smaller) than the thermodynamical one for $B^* < 10^2$ ($B^* > 10^2$). It should be stressed that, for $B = 0$, the dynamical spinodal predicts a smaller transition density, so the details between $B^* = 50$ and $B = 0$ cannot be seen from the figure, and need to be determined specifically; b) AMM does not affect much the results obtained with $B^* < 10^3$. However, the AMM reduces in a non-negligible way the instability region for the larger fields, giving rise to smaller crust thicknesses and momentum of inertial crustal fractions.

5.3 Joint effect of temperature and magnetic field on the thermodynamical spinodal section

Our main objective is to determine for which temperatures is the effect of the magnetic field washed out on the extension of the crust. This will be done with a thermodynamical spinodal approach, and excluding the AMM.

In the last section it was shown that at $T = 0$, the effect of the AMM is negligible for $B^* < 10^3$. The effect of the AMM at finite temperature should also be analyzed, but we will postpone this study for a future investigation. At the end of the section, we will draw some comments concerning this point.

The temperature of the crust decreases as the star cools. While a very young star, less than one year old, may have an inner crust temperature above 10^9 K, it will drop below 10^9 K or even 10^8 K after 1 year, depending on the EoS considered and the mass of the star [Chamel and Haensel, 2008, Yakovlev et al., 2001]. It is, therefore, reasonable to ask whether the strong effect of the magnetic field on the crust-core transition calculated at $T = 0$, with the appearance of a transition region where stable and unstable regions alternate, still persists at finite temperature. Moreover, the time evolution of both the magnetic field and temperature inside the star are strongly coupled, and, therefore, it is important to understand which is the effect of the temperature on the transition region created by a magnetic field.

In Fig. 5.4, we show the spinodal sections for $B^* = 10^5$ and $B^* = 10^4$ at different temperatures for the NL3 model. Except for $T = 200$ keV, all the other temperatures are above 1 MeV. The spinodal sections get smaller and smaller, and shrink to a region that is quite isospin

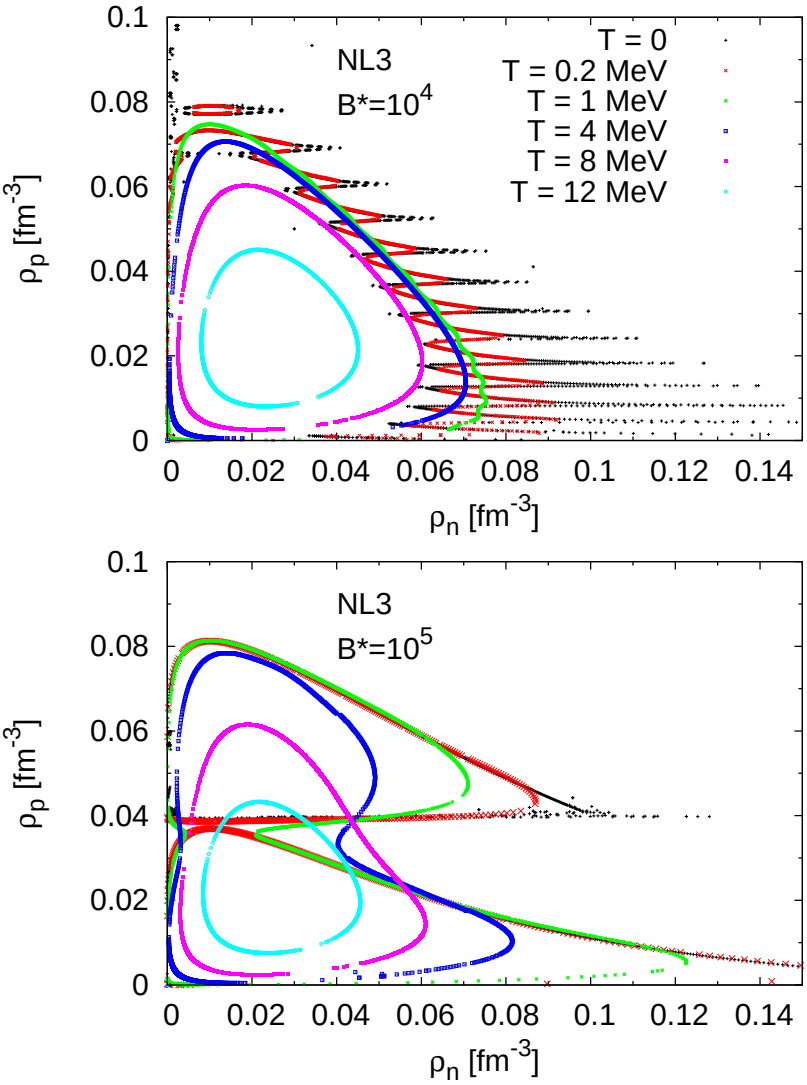

Figure 5.4: Thermodynamical spinodals for different temperatures, and taking $B^* = 10^4$ (top) and $B^* = 10^5$ (bottom) for the NL3 model without AMM. The lack of definition for the smaller fields at low proton density is a numerical constraint that would be overcome with longer CPU time.

symmetric, when the temperature increases, for both magnetic fields. There are two separated regions for $B^* = 10^5$ at $T = 0$ MeV, corresponding to the filling of the two Landau levels. These regions combine to one, and the curve gets smoother at $T = 4$ MeV, although there are still two clear gaps on the curve. When the temperature increases further, the gaps exist until $T = 10$ MeV. We also find that the shape of the spinodals change fast when the temperature increases from $T = 0$ MeV to $T = 4$ MeV. These results also hold for $B^* = 10^4$, but, in this case, already at $T \gtrsim 1$ MeV, the shape of the spinodals has lost most of the spike-like structures, although it is still seen a certain "wiggling" at the smaller proton densities.

The Landau quantization will be completely washed out by temperatures of the order of the energy separation between consecutive Landau levels, i.e. $T \gtrsim eB/M^* = m_e^2 B^*/M^*$. For $B^* = 10^3$ ($B^* = 10^4$), and taking $M^* \sim 700$MeV for $\rho \sim 0.09$ fm^{-3}, this corresponds to $T \gtrsim 0.3$ MeV ($T \gtrsim 3$ MeV). The effects become important already for 10% of this value in the regions of larger isospin asymmetry, i.e. larger ρ_n.

5.4 Effect of temperature on the crust-core transition under a strong magnetic field

In the following, we calculate the crust-core transition density/region at finite temperature. Temperatures in the range 1 keV$< T < 1$ MeV ($10^7 < T < 10^{10}$ K) will be considered. We will carry this study by calculating the thermodynamical spinodal without AMM. We have seen that above $B^* \sim 10^3$ ($B \sim 5 \times 10^{16}$ G), the AMM has a non-negligible effect and, therefore, we will essentially restrict ourselves to values below that number.

Fig. 5.5 shows the effect of temperature on the spinodal for temperatures below 4 MeV for NL3$\omega\rho$ model (top panel) and NL3 model (lower panel). For $B = 0$ (top panel), a temperature $T \leq 1$ MeV has practically no effect on the spinodal, except in a small region for very asymmetric matter. The crust-core transition density, obtained from the intersection of the β-equilibrium EoS with the spinodal, is only affected by temperatures above 1 MeV.

To illustrate the simultaneous effect of temperature and the magnetic field on the crust-core transition, we have plotted in the lower panel of Fig. 5.5 the spinodal surfaces for $0 \leq T \leq 4$ MeV and $B^* = 10^4$, together with the β-equilibrium EoS for NL3 model. As before, the ef-

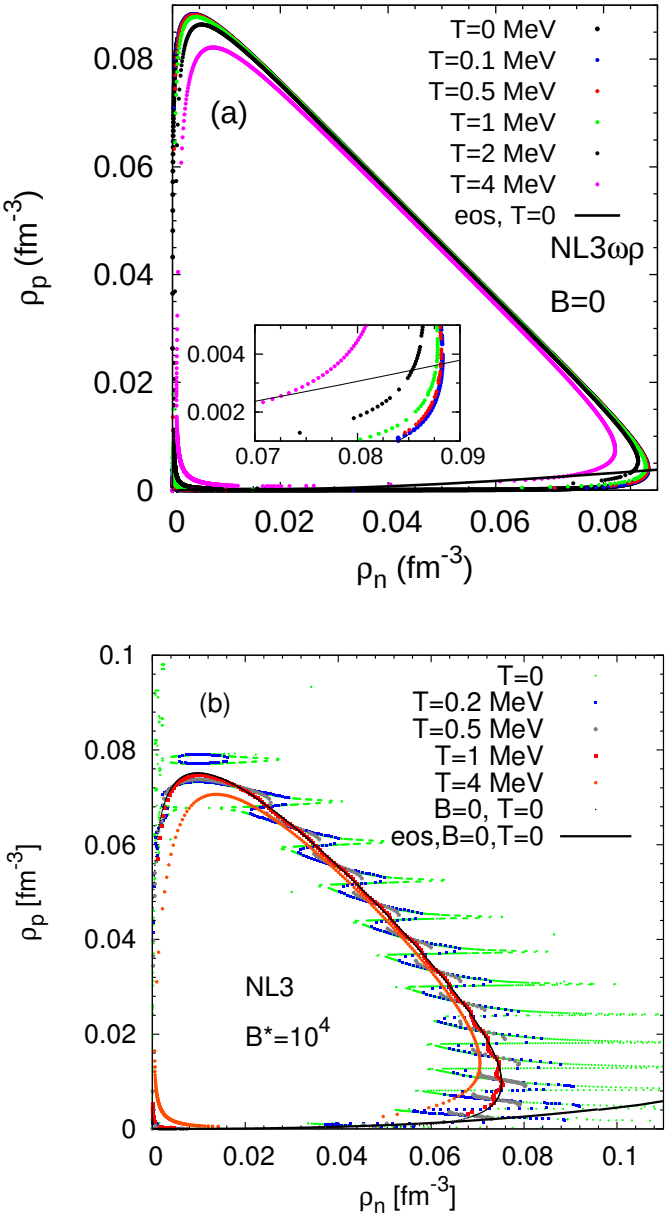

Figure 5.5: Thermodynamical spinodals for several temperatures for (a) NL3$\omega\rho$ with $B = 0$, and (b) NL3 with $B^* = 10^4$ without AMM. The black solid line is the β-equilibrium equation of state at $B = T = 0$.

fect of the temperature is very clear: it washes out the bands, and, for $T = 1$ MeV, the effect of the magnetic field resumes to a slight oscillation of the spinodal section along the $B = 0$ one. We may expect that for lower magnetic field intensities, the bands will be washed out at lower temperatures, as we will see in the following. For low temperatures, the β-equilibrium EoS crosses the spinodal section several times, defining the region of instability referred in the previous sections. In Fig. 5.2, we saw that the transition region for $T = 10$ keV is smaller than the one obtained for $T = 1$ keV, because the EoS is not crossing anymore the last band shown in the plot. The transition region becomes smaller and smaller as T increases, until the crossing occurs at a well defined density, as for $T \geq 100$ keV in Fig. 5.2.

In Table 5.3, we give the transition densities and pressures for $B^* \leq 10^4$ and $0 \leq T \leq 1$ MeV for NL3$\omega\rho$ model. In order to get results for these range of temperatures, we have implemented in our finite temperature codes the method proposed in [Aparicio, 1998]. In Appendix C, we present the different integrals in terms of the Fermi-Dirac functions used in the calculations.

The densities ρ_1 and ρ_2 are determined from the first and last crossing between the spinodal section and β-equilibrium EoS, as referred in the previous section, and illustrated in Fig. 5.2. It is seen that, as the temperature increases, the extension of the bands becomes smaller, and the number of crossings diminishes, until it occurs at a single point. Besides the transition densities and pressures, we also include the crust thickness ΔR, the thickness of the transition region for $B \neq 0$, $\Delta R' = R(\rho_1) - R(\rho_2)$, and the correspondent fractional moment of inertia of the neutron star crust, determined using eq. (2.48). These quantities were obtained with a model with $L = 55$ MeV from the thermodynamical spinodal without the inclusion of the AMM, and for a star of $M = 1.4\ \mathrm{M}_\odot$ and $R = 13.734$ km. The crust thicknesses were estimated from the integration of the TOV equations at $B = 0$. The magnetic field $B^* = 10^4$ could already be too strong for this approximation, and, therefore, we will concentrate our discussion on the weaker fields, i.e. $B^* \leq 10^3$.

In order to help the discussion, we have plotted in Fig. 5.6 the transition densities, ρ_1 and ρ_2 (top panel), the crust thickness, ΔR (middle panel), and the momentum of inertial crustal fration (bottom panel) for $B^* \leq 10^3$. The densities ρ_2 come closer to the lower limit, ρ_1, of the transition region as the temperature increases, and it is interesting to see that for magnetic field intensities considered at $T = 100$ keV, all magnetic field effects have been washed out, and the $B = 0$ transi-

Table 5.3: Transition densities and pressures for the magnetic fields considered in this study and several temperatures, together with the crust thicknesses, ΔR, the thickness due to the inhomogeneous region found when $B \neq 0$, $\Delta R' = R(\rho_1) - R(\rho_2)$, and the correspondent fractional moment of inertia of the neutron star crust, obtained from the thermodynamical spinodal without AMM and with $L = 55$ MeV, for a star of $M = 1.4\ \mathrm{M}_\odot$ and $R = 13.734$ km.

T (KeV)	ρ_1 (fm^{-3})	ρ_2 (fm^{-3})	P_1 $\left(\frac{\mathrm{MeV}}{\mathrm{fm}^3}\right)$	P_2 $\left(\frac{\mathrm{MeV}}{\mathrm{fm}^3}\right)$	ΔR (m)	$\Delta R'$ (m)	$\frac{\Delta I_{cr}}{I}$
			$B^* = 50$				
0	0.0908	0.0967	0.6100	0.7058	1473	52	0.0848
0.1	0.0912	0.0955	0.6160	0.6860	1463	38	0.0831
1.	0.0914	0.0929	0.6204	0.6437	1440	13	0.0794
10.	-	0.0919	-	0.6279	1431	0	0.0779
100.	-	0.0919	-	0.6278	1431	0	0.0779
1000.	-	0.0906	-	0.6076	1420	0	0.0761
			$B^* = 100$				
0	0.0907	0.1009	0.6101	0.7849	1514	93	0.0913
1.	0.0911	0.0941	0.6145	0.6619	1450	26	0.0810
10.	-	0.0920	-	0.6284	1431	0	0.0780
100.	-	0.0919	-	0.6278	1431	0	0.0779
1000.	-	0.0913	-	0.6173	1425	0	0.0770
			$B^* = 200$				
0.	0.0893	0.1065	0.5888	0.9013	1574	165	0.1004
1.	0.0908	0.0960	0.6114	0.6947	1467	45	0.0838
10.	0.0916	0.0923	0.6231	0.6342	1435	6	0.0785
100.	-	0.0919	-	0.6279	1431	0	0.0779
1000.	-	0.0913	-	0.6179	1425	0	0.0770
			$B^* = 500$				
0.	0.0874	0.1163	0.5616	1.1500	1693	299	0.1175
1.	0.0897	0.1016	0.5939	0.7982	1521	109	0.0924
10.	0.0910	0.0928	0.6129	0.6408	1438	15	0.0791
100.	-	0.0919	-	0.6281	1431	0	0.0779
1000.	-	0.0913	-	0.6185	1426	0	0.0771

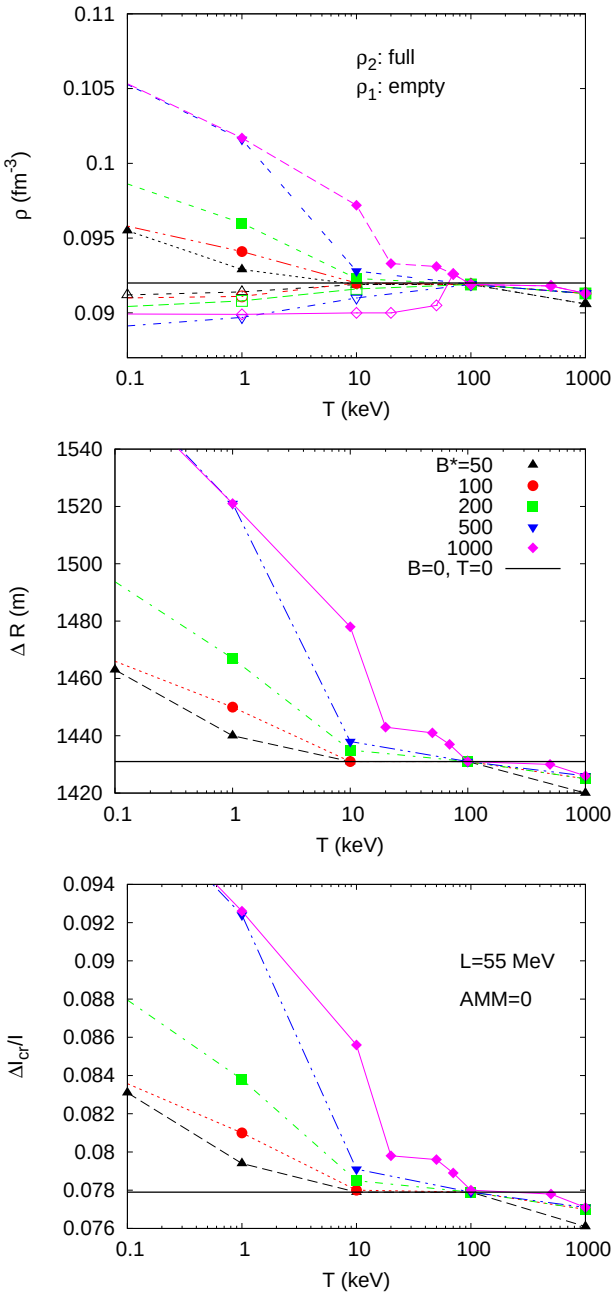

Figure 5.6: The transition densities, ρ_1 (empty) and ρ_2 (full), (top), the crust thickness (middle), and the momentum of inertial crustal fraction (bottom) for NL3$\omega\rho$, with $L = 55$ MeV, for several values of B^* and T. The thermodynamical spinodal formalism without AMM has been used. The horizontal black lines show the location of the respective quantities at zero temperature and zero magnetic field.

Table 5.4: *(continuation)*

T (KeV)	ρ_1 (fm^{-3})	ρ_2 (fm^{-3})	P_1 $\left(\frac{\text{MeV}}{\text{fm}^3}\right)$	P_2 $\left(\frac{\text{MeV}}{\text{fm}^3}\right)$	ΔR (m)	$\Delta R'$ (m)	$\frac{\Delta I_{cr}}{I}$
			$B^* = 10^3$				
0	0.0900	0.1162	0.5985	1.1481	1686	271	0.1174
1.	0.0899	0.1017	0.5982	0.8001	1521	107	0.0926
10.	0.0900	0.0972	0.5984	0.7159	1478	64	0.0856
100.	-	0.0919	-	0.6294	1431	0	0.0780
500.	-	0.0918	-	0.6266	1430	0	0.0778
1000.	-	0.0913	-	0.6189	1426	0	0.0771
			$B^* = 10^4$				
0	0.0839	0.1075	0.5207	0.9484	1584	218	0.1033
1.	0.0840	0.1076	0.5221	0.9513	1587	220	0.1035
10.	0.0840	0.1076	0.5220	0.9503	1586	219	0.1034
100.	-	0.0839	-	0.5215	1367	0	0.0677
500.	-	0.0868	-	0.5627	1389	0	0.0716
1000.	-	0.0903	-	0.6191	1418	0	0.0767

tion density has been recovered. As it can be seen from Table 5.3, for a stronger field, this is not anymore true, but since for these stronger fields, several of the suppositions considered in the present work break, such as the use of the TOV equations or the exclusion of the AMM of the nucleons, we will not discuss so strong fields. Above $T = 100$ keV, ρ_1 and ρ_2 coincide, but they take values below the $T = 0$ transition density: this is the reduction of the extension of the spinodal section due to temperature effects. We conclude that we may expect the appearance of a transition region of nonzero thickness for temperatures in the crust below 100 keV, and a magnetic field intensity at the crust-core transition below $B \sim 5 \times 10^{16}$ G.

With respect to the crust momentum of inertia fraction, we realize that even considering that the thermodynamical approach predicts larger crust-core transition densities, we have obtained values that can account for the Vela glitches which, according to [Andersson et al., 2012], would require a fractional crustal momentum of inertia $\sim 0.065-0.095$, considering that the effective neutron mass, including entrainment effects, is $4-6$ times larger than the neutron bare mass. Further studies should, however, be undertaken, because strong magnetic fields, as the ones considered in the present work, will certainly influence

the neutron superfluid behavior, and affect the neutron entrainment to the lattice.

The main effect of having used the thermodynamical spinodal instead of the dynamical one is that the predicted crust-core transition density is $\sim 10\%$ larger, the crust fraction momentum of inertia $\sim 10-15\%$ larger, and the transition region slightly smaller, but the overall conclusions remain valid.

5.5 Effect of the magnetic field on the distillation effect

The density fluctuations ratio $\delta\rho_p^-/\delta\rho_n^-$ defines the direction of the evolution of the instability which shows how the system separate into a dense liquid and a gas phase. This ratio also measures the efficiency in restoring isospin symmetry: the larger the value, the greater the efficiency. As discussed in [Margueron and Chomaz, 2003, Providência et al., 2006a], the direction of instability defines the way the distillation effect is affected. The distillation effect has been observed experimentally in heavy-ion reactions [Chomaz and Gulminelli, 1999, Xu et al., 2000, Chomaz, 2001], and corresponds to the formation of the clusters with low isospin asymmetry in a background of a neutron gas.

In order to understand under which conditions the unstable modes produce more symmetric dense matter and more asymmetric gas, we will study, in the following, how $\delta\rho_p^-/\delta\rho_n^-$ changes with the magnetic field (see also [Rabhi et al., 2009a, Chen, 2017]), and with the temperature.

In Fig. 5.7, we plot the ratio $\delta\rho_p^-/\delta\rho_n^-$ for different values of the magnetic fields, and for the fixed density $\rho = 0.06$ fm^{-3}, for NL3 model, as a function of the proton fraction, with (bottom panel) and without (top panel) AMM. The middle point corresponds to symmetric matter $y_p = 0.5$, with $\delta\rho_p^-/\delta\rho_n^- = 1$ the ratio of density fluctuations for symmetric matter with $B = 0$.

For $B^* = 10^5$, the spinodal has two bands, corresponding to the occupation of the first and second Landau levels. The large discontinuity of $\delta\rho_p^-/\delta\rho_n^-$ at $y_p \sim 0.67$ corresponds to the transition from the first to the second level. Above this proton fraction value, the curve behaves like the $B = 0$ case, and increases with y_p: this is the range corresponding to larger proton densities and, therefore, less sensitive to the magnetic field. For $y_p < 0.67$, the behavior is quite different: the curve decreases

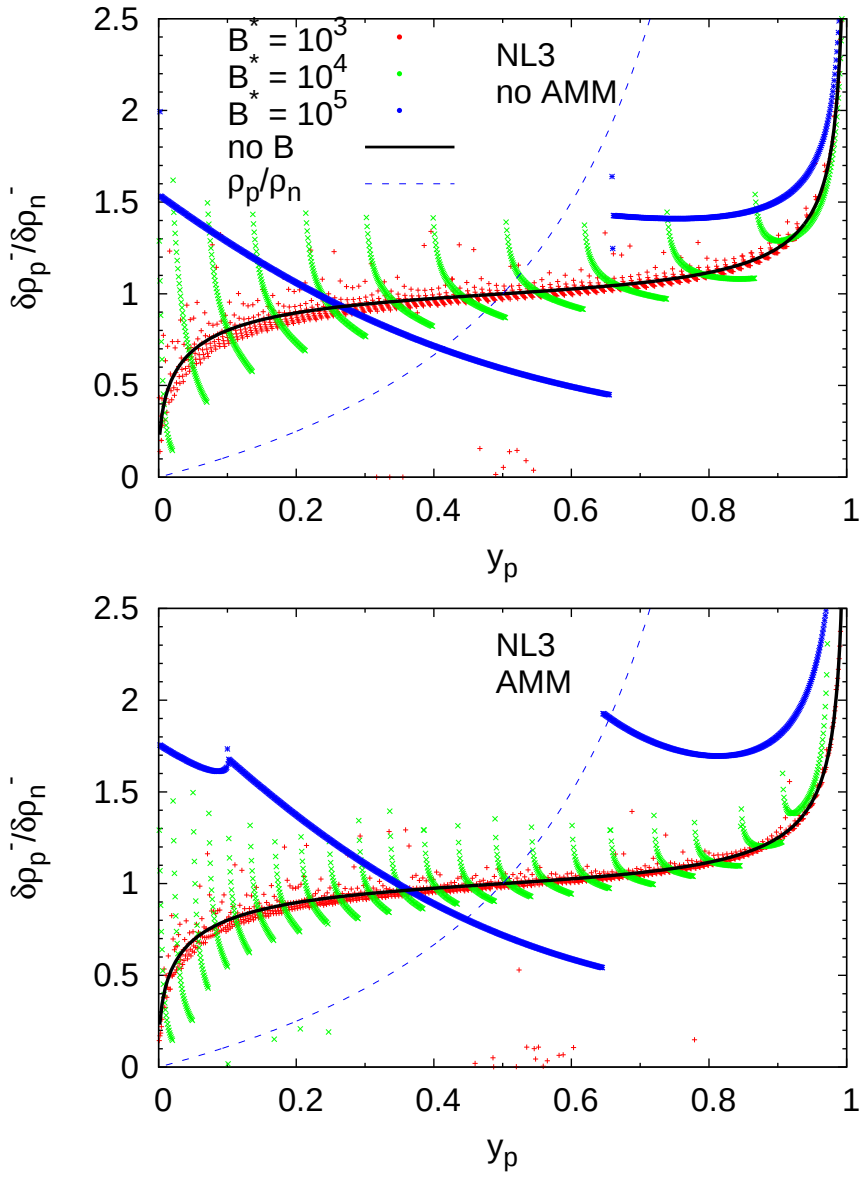

Figure 5.7: $\delta\rho_p^-/\delta\rho_n^-$ plotted as a function of the proton fraction with $T = 0$ MeV and $\rho = 0.06$ fm^{-3}, for different values of the magnetic fields, for NL3 model with (bottom) and without (top) AMM. The dashed line is the ratio between the proton and neutron densities.

from the value at y_p=0 to a value much smaller than the corresponding value of the fraction ρ_p/ρ_n.

The fluctuations will not drive the system out of the first Landau level and, therefore, the larger the proton fraction, the closer the system comes to the top of the band, and the smaller are the allowed proton fluctuations. For $y_p > 0.67$, the Landau level is only partially filled, and the fluctuations are not constrained by the filling of the Landau level.

This process is repeated for $B^* = 10^4$, involving more Landau levels. For each Landau level, the curves decrease, except for the last one, corresponding to last Landau level, which increases, and follows the $B = 0$ behavior. When $B^* = 10^3$, more curves appear. The total curves behave like the $B = 0$ case: the fraction $\delta\rho_p^-/\delta\rho_n^-$ is larger than ρ_p/ρ_n below $y_p = 0.5$, and less than ρ_p/ρ_n above.

The inclusion of the AMM doubles the numbers of discontinuities in the fluctuation ratios. Except for the larger field shown, the fluctuations around the $B = 0$ case are smaller, because the AMM stiffens the EoS.

In Figs. 5.8, we plot the ratio of the proton over neutron density fluctuation $\delta\rho_p/\delta\rho_n$ as the function of nuclear density with the model NL3 for a fixed proton fraction, $y_p = 0.2$. Nuclear matter under different values of the magnetic fields with and without AMM is considered. When the effects of magnetic fields are taken into account, outside the spinodal region defined by $B = 0$, discrete instability regions may occur. We do not restrict ourselves to the densities where the eigenvalue of $\mathcal{F}$ give equation number are negative, but we will obtain the ratio of the fluctuations for a whole range of densities below 0.15 fm^{-3}. We believe that it is still instructive when exploring the direction of the instability under magnetic fields, even realizing that we will be covering both stable and unstable regions.

We observe that the $\delta\rho_p^-/\delta\rho_n^-$ decreases with density, for $B^* = 10^5$. The density fluctuations occur in such a way that the system stays in the same Landau level: the larger the total density, the smaller the fluctuations. Only the first Landau level is occupied, and is almost complete, which prevents the existence of large proton density fluctuations. For $B^* = 10^4$ and $B^* = 10^3$, the curves are divided in too many pieces, and $\delta\rho_p^-/\delta\rho_n^-$ decreases with the density, for each one. Many Landau levels appear for $B^* = 10^4$ and $B^* = 10^3$, as discussed before, and this explains why there are so many discontinuities.

We conclude that the magnetic field will have a direct effect on the distillation, amplifying it or disfavoring it according to the fraction of

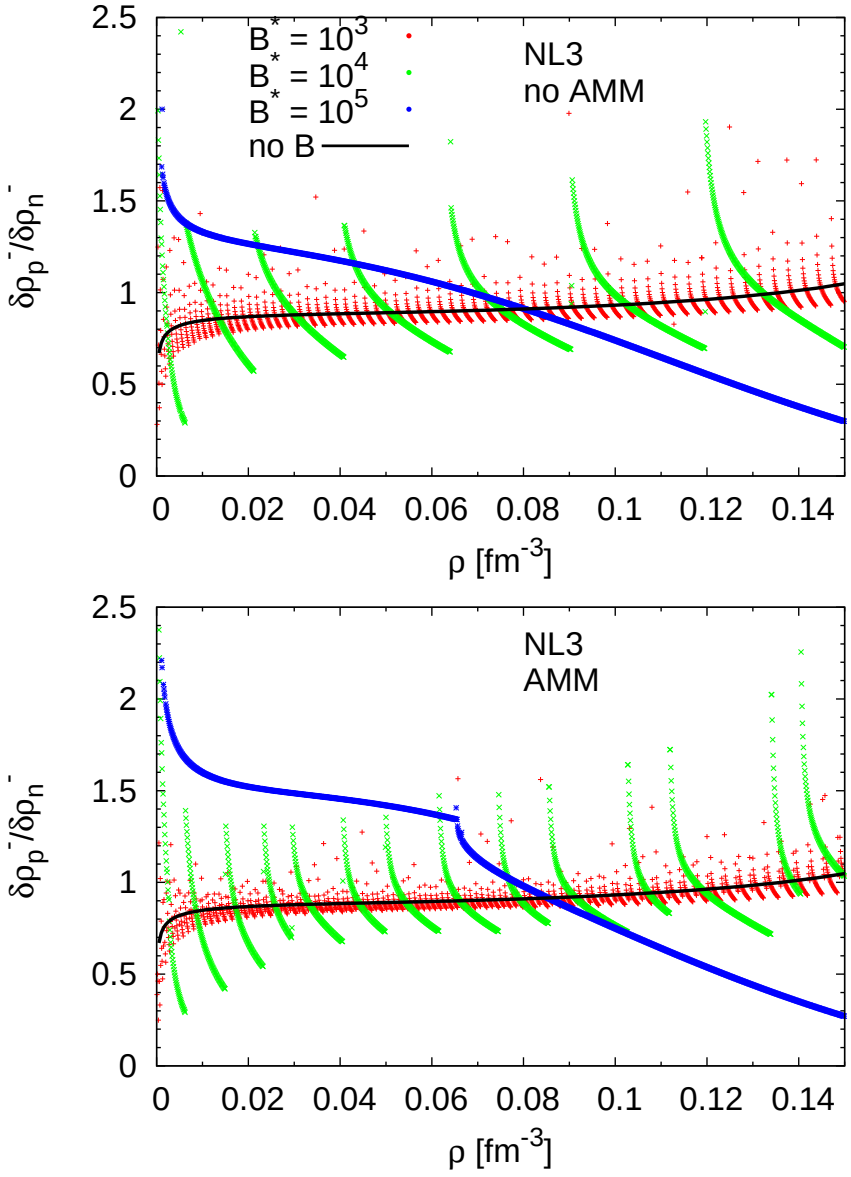

Figure 5.8: $\delta\rho_p^-/\delta\rho_n^-$ plotted as a function of the density with $y_p = 0.2$ for different values of the magnetic fields with (bottom) and without (top) AMM for the NL3 model.

states in a given Landau level already filled. An almost empty level favors the distilation effect, and the opposite occurs, for an almost full level.

In Fig. 5.9, we plot the ratio $\delta\rho_p^-/\delta\rho_n^-$ for $B^* = 10^5$ and $B^* = 10^4$ with $\rho = 0.06$ fm^{-3} as a function of the proton fraction, for different temperatures, and for the NL3 model. We have already discussed that, at $T = 0$ and $B^* = 10^5$, the spinodal has two bands, corresponding to the occupation of the first two Landau levels. The transition from one to the other has a large discontinuity at $y_p \sim 0.67$. The discontinuity disappears when $T > 0.2$ MeV. The curve becomes monotonously increasing when $T > 8$ MeV. This process is repeated for $B^* = 10^4$, involving more Landau levels.

The ratios the ratio $\delta\rho_p^-/\delta\rho_n^-$ decrease with the proton fraction within a Landau level, except for the largest occupied Landau level, where after decreasing, the ratio increases with proton fraction until $y_p = 1$ is reached. We can conclude that the effect of the magnetic fields will get weaker with the increase of the temperature, but, for each magnetic field, there is a temperature below which the effect of magnetic field is non negligible. When this temperature is below the ones occurring inside neutron stars, it is not important to consider the magnetic field effect.

Compared to the $T = 0$ and $B = 0$ case, for both $B^* = 10^5$ and $B^* = 10^4$, there is a temperature, at which the shape of the curve is quite close to the $T = 0$ and $B = 0$ curve. This is easy to understand: the strong magnetic field and finite temperature impose opposite effects on the shape of the spinodal. The strong magnetic fields make the spinodal region larger, while the temperature makes the region smaller. At finite B, the effect of temperature is to wash out the effects of the Landau quantization.

In Fig. 5.10, we show the ratio of the density fluctuation $\delta\rho_p^-/\delta\rho_n^-$ as a function of the density for the NL3 model, for different temperatures, and $y_p = 0.2$, taking $B^* = 10^5$ and $B^* = 10^4$. As before, it is seen that the temperature washes out the effects of the magnetic field, and the behavior gets closer to the one obtained for $B = 0$.

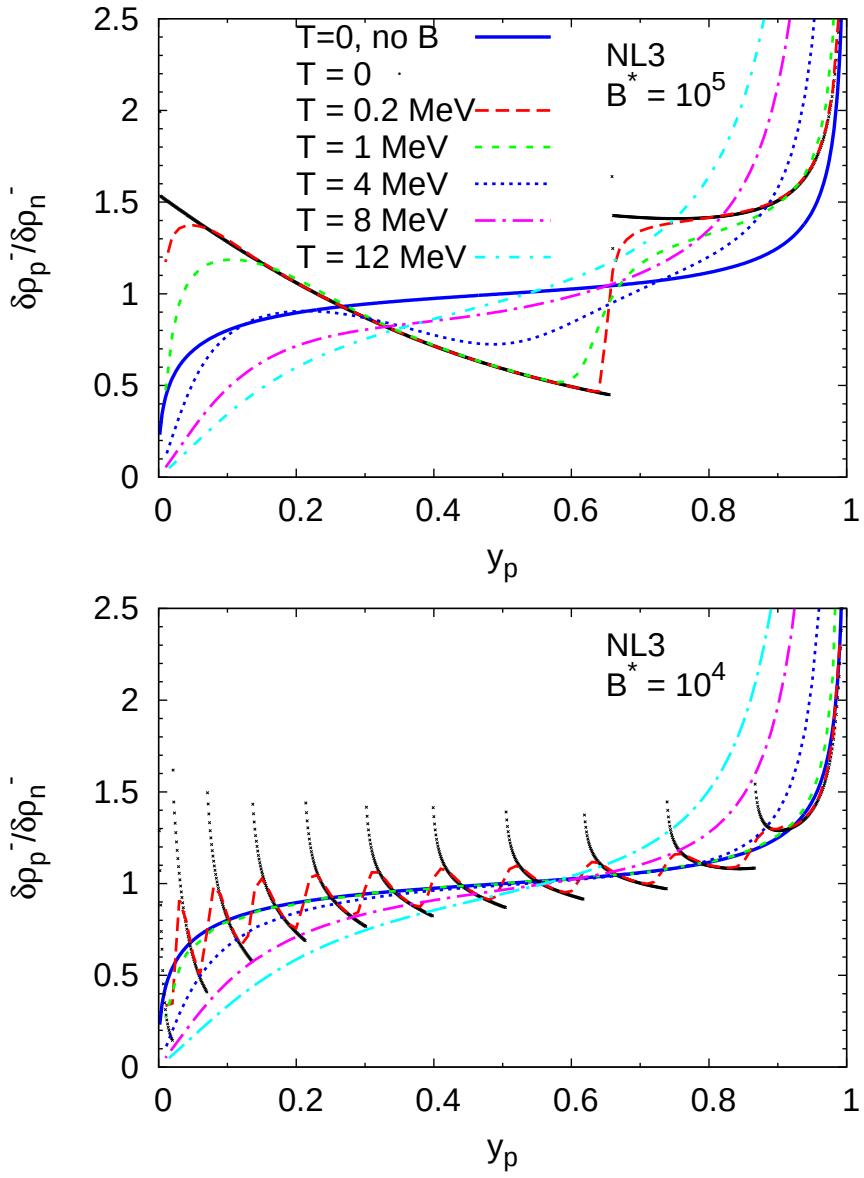

Figure 5.9: $\delta\rho_p^-/\delta\rho_n^-$ plotted as a function of the proton fraction for $B^* = 10^5$ (top) and $B^* = 10^4$ (bottom), with $\rho = 0.06$ fm^{-3}, for several temperatures, and for the NL3 model. The curve for $T = 0$ and $B = 0$ is also shown as a blue line in the figure.

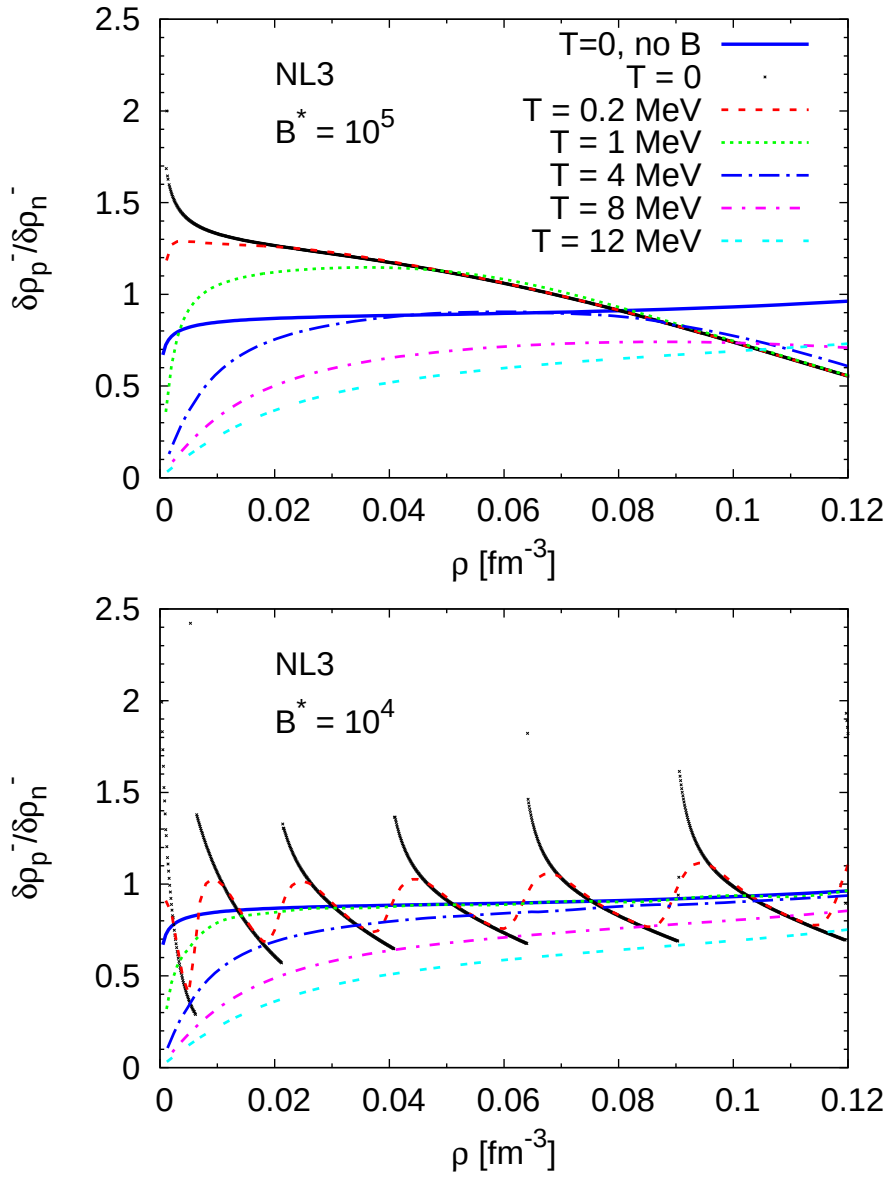

Figure 5.10: $\delta\rho_p^-/\delta\rho_n^-$ plotted as a function of the density for $B^* = 10^5$ (top) and $B^* = 10^4$ (bottom) with $y_p = 0.2$ for several temperatures, and for the NL3 model. The curve for $T = 0$ and $B = 0$ is also shown as a blue line in the figure.

Chapter 6

Conclusions

We have extended the relativistic Vlasov equation, by including the effect of an external magnetic field in the formalism, which gives rise to the Landau quantization of the energy levels of the charged particles. The linearized Vlasov equation was used to calculate the eigenmodes of nuclear and stellar matter in the presence of very strong magnetic fields, as may be found in magnetars. Within this formalism, it is possible to estimate the crust-core transition inside neutron stars from the intersection of the spinodal section, the surface where the eigenmodes go to zero, with the β-equilibrium equation of state. The AMM of protons and neutrons is taken into account, and it is shown that it is not negligible for magnetic fields above 10^{15} G, and that it contributes to an extra complexity of matter at the crust-core transition. Inside these surfaces, matter will separate into a dense and a gas phase.

The Vlasov description of stellar matter modes takes into account both the Coulomb field and finite size effects related to the finite range of nuclear force. We have only considered the propagation of waves in the direction of the magnetic field. The effect of the Landau quantization of the levels of charged particles gives rise to a spinodal section that presents a structure of bands at the border between clusterized and homogeneous matter. As a consequence, it was shown that the transition between the crust and the core of magnetars is defined by a complex region that is $\sim 0.02 - 0.04$ fm^{-3} wide, characterized by a succession of homogeneous and clusterized matter. The determination of the mode associated with the maximum growth rate in the density range delimited by the spinodal section, allowed the estimation of several properties of the clusters that are formed in the unstable regions, in particular, the size and a qualitative prediction of the charge content.

The free energy negative curvature is an indication that stable matter will exist with a nonhomogeneous composition, formed by a dense and a gas phase. When more than one conserved charge is involved, and a long range force, such as the Coulomb force, comes into play, the phase separation is a complex mechanism. Compared with the $B = 0$ situation, it was shown that close to the transition to homogeneous matter, and due to the existence of an irregular spinodal section, there is a heterogeneous region of alternating inhomogeneous and homogeneous matter. Besides, it was also shown that inside the spinodal section, the average size of the clusters and its proton content vary in an oscillatory way, reinforcing the heterogeneity of the inner crust matter, which could have a direct effect on the charge impurity parameter associated to the inner crust at the crust-core interface. The impurity coefficient is a measure of the deviation from a regular distribution of charge, and in [Pons et al., 2013] a high impurity coefficient was needed to cause a fast decay of the magnetic field, and explain the non-observation of isolated pulsars, with periods larger than 12 s.

In particular, at the crust-core transition, the effect on the proton content of clusters is quite strong. The disconnected unstable regions occur with the opening of new Landau levels, until a maximum that we have tried to find. The extension of the spinodal, at zero proton density, defined by $(\rho_p, \rho_n) = (0, \rho_n^{max})$, does not depend on the magnetic field, if the AMM is not considered, and is obtained taking the proton Landau level equal to zero. If the AMM is included, the extension of the spinodal is smaller, it approaches the no-AMM result, as the field becomes weaker. This value of the density, $\rho_n^{max} = 0.21$ fm^{-3} for NL3, and 0.12 fm^{-3} for NL3$\omega\rho$, sets an upper limit on our spinodals at zero proton density, and lowest Landau level, which will, however, be affected by the AMM.

The two main effects that could affect the impurity parameter are: the fluctuation of the cluster sizes, and the proton fraction of the clusters measured from the transition density fluctuations. If larger proton fractions occur in a region where the size of the cluster changes in a short density range, this will probably lead to larger impurity coefficients, and a calculation has to be performed. The magnetic field could, therefore, enforce the impurity parameter. These results indicate that it is necessary to study the transport properties, such as electric conductivity and shear viscosity, of this complex matter, see [Yakovlev, 2015, Ofengeim and Yakovlev, 2015].

The maximum growth rates at constant proton fraction allow a prediction of the structure of the crust-core transition: for fields with in-

tensity 5×10^{17}G, there is a closed region that, although with some fluctuations, follows the $B = 0$ curve, followed by separate regions, whose density width decreases continuously until homogeneous matter sets in. This separate regions appear when a new Landau level starts being filled, and only while filling the bottom of the Landau level.

We refer another pulsar property that could be affected by an increase of the crust. Pulsar glitches are attributed to the angular momentum transfer between the crust and the core [Link et al., 1999], involving the vortex dynamics associated to the neutron superfluid confined in the inner crust. However, the recent detection of an anti-glitch [Archibald et al., 2013], or the indication that, due to entrainment, the inner crust angular moment is not enough to explain the glitch mechanism [Andersson et al., 2012], suggests that the glitch theory has to be clarified. The effects of the magnetic field on the inner crust, in particular, an increase of the crust, the succession of clusterized and homogeneous layers, and a non-monotonic change of the neutron gas background density will certainly affect the glitch mechanism, and should be taken into account in a glitch theory.

Next, we studied the thermodynamical instability of np matter within NL3 and NL3$\omega\rho$ models for some values of magnetic fields at $T = 0$ and finite temperature. The bands are still present due to the Landau quantization under strong magnetic fields. When the magnetic fields get weaker, the bands are replaced by some disconnected regions. We have confirmed that due to the sensitivity of the magnetic field to the proton density, the extension of the crust-core transition region strongly depends on the slope L of the symmetry energy. The larger the slope L, the larger the transition region, because, below saturation density, models with a large L present smaller symmetry energies and, therefore, accept smaller proton fractions. Experimental and theoretical constraints seem to limit L below 80 MeV ($30 < L < 80$ MeV) [Tsang et al., 2012], resulting in a more moderate effect of the magnetic field on the extension of the crust. Properties of magnetized neutron stars that directly depend on the thickness of the crust can set stringent constraints on the symmetry energy slope L due to the great sensitivity of the crust size to this property.

We have also studied the effect of temperature for magnetic fields $B \leq 5 \times 10^{16}$ G. The magnetic field effects on the extension of the transition density are washed out for temperatures above 10^9 K, but below these temperatures, even a field of intensity 2×10^{15} G will have a finite effect on the crust thickness. Microphysical parameters, such as transport coefficients, that enter in the magneto-thermal evolution

equations of a neutron star, are certainly affected by the existence of the crust-core transition region that changes with cooling, and the impact of this effect should be investigated. Recently, a one dimensional thermal-magneto-plastic model, that considered transport coefficients sensitive to temperature, as well as the coupling of the crustal motion to the magnetosphere, has been implemented, and it has been shown that this coupling induces an enrichment and acceleration of the magnetar dynamics [Li et al., 2016].

Appendix A

Equations of motion of the fields

The equations, describing the time evolution of the fields ϕ, V^μ, A^μ, and the third component of the ρ-field $b_{3\mu} = (b_0, \mathbf{b})$, are derived from the Euler-Lagrange formalism:

$$\frac{\partial^2\phi}{\partial t^2} - \nabla^2\phi + m_s^2\phi + \frac{\kappa}{2}\phi^2 + \frac{\lambda}{6}\phi^3 = g_s[\rho_s^p + \rho_s^n] \,, \tag{A.1}$$

$$\frac{\partial^2 V_\mu}{\partial t^2} - \nabla^2 V_\mu + m_v^2 V_\mu \, + 2\Lambda_v g_v^2 g_\rho^2 b_{3\mu} \cdot b^{3\mu} V_\mu = \, g_v[j_\mu^p + j_\mu^n] \,, \tag{A.2}$$

$$\frac{\partial^2 b_{3\mu}}{\partial t^2} - \nabla^2 b_{3\mu} + m_\rho^2 b_{3\mu} \, + 2\Lambda_v g_v^2 g_\rho^2 V_\mu V^\mu b_{3\mu} = \, \frac{g_\rho}{2}[j_\mu^p - j_\mu^n] \,, \tag{A.3}$$

$$\frac{\partial^2 A_\mu}{\partial t^2} - \nabla^2 A_\mu \, = \, e[j_\mu^p - j_\mu^e] \,, \tag{A.4}$$

where the scalar densities are given by

$$\rho_s^p(\mathbf{r}, t) = \frac{eB}{(2\pi)^2} \sum_{\nu,s} \int dp_z f_p \frac{\bar{m}_p M^*}{(\bar{m}_p + s\mu_N \kappa_p B)\epsilon_p} \,, \tag{A.5}$$

$$\rho_s^n(\mathbf{r}, t) = \frac{1}{(2\pi)^3} \sum_s \int d^3p f_n \left(1 - \frac{s\mu_N \kappa_n B}{\sqrt{M^{*2} + p_\perp^2}}\right) \frac{M^*}{\epsilon_n} \,, \tag{A.6}$$

and the components of the four-current density are

$$j_0^i(\mathbf{r},t) = \rho_i = \frac{eB}{(2\pi)^2}\sum_{\nu,s}\int f_i(\mathbf{r},\mathbf{p},t)dp_z, \quad i=p,e\ , \tag{A.7}$$

$$j_0^n(\mathbf{r},t) = \rho_n = \frac{1}{(2\pi)^3}\sum_{s}\int f_n(\mathbf{r},\mathbf{p},t)d^3p\ , \tag{A.8}$$

$$\mathbf{j}^i(\mathbf{r},t) = \frac{eB}{(2\pi)^2}\sum_{\nu,s}\int f_i(\mathbf{r},\mathbf{p},t)\frac{\bar{\boldsymbol{p}}_z^i}{\epsilon_i}dp_z, \quad i=p,e, \tag{A.9}$$

$$\begin{aligned}\mathbf{j}^n(\mathbf{r},t) &= \frac{1}{(2\pi)^3}\sum_{s}\int f_n(\mathbf{r},\mathbf{p},t)d^3p \\ &\times \left[\frac{\bar{\boldsymbol{p}}_z^n}{\epsilon_n}+\frac{\bar{\boldsymbol{p}}_\perp^n}{\epsilon_n}\left(1-\frac{s\mu_N\kappa_n B}{\sqrt{M^{*2}+(\bar{\boldsymbol{p}}_\perp^n)^2}}\right)\right]\ .\end{aligned} \tag{A.10}$$

Appendix B

The coefficients of the determinant of the dispersion relation

The coefficients a_{ij} of the matrix (3.64) can be written as:

$$a_{11} = \sum_{\nu,s} \frac{g_s}{2\pi^2} \frac{G_{\phi_p} M^*}{\omega_s^2} \frac{eB}{P_F^p (s_p^2 - 1)}, \tag{B.1}$$

$$a_{12} = -\sum_{\nu,s} \frac{eB}{2\pi^2 V_F^p (s_p^2 - 1)} \left[\left(1 - \frac{\omega^2}{k_z^2} C_{1p} \right) g_v D_{1p} + \left(1 - \frac{\omega^2}{k_z^2} C_{2p} \right) \frac{g_\rho}{2} D_{2p} + \left(1 - \frac{\omega^2}{k_z^2} \right) \frac{e^2}{\omega_A^2} \right] - 1, \tag{B.2}$$

$$a_{13} = \sum_{\nu,s} \frac{g_s}{2\pi^2} \frac{G_{\phi_p} M^*}{\omega_s^2} \frac{1}{V_F^p \epsilon_F^n (s_p^2 - 1)}, \tag{B.3}$$

$$a_{14} = -\sum_{\nu,s} \frac{1}{2\pi^2 V_F^p (s_p^2 - 1)} \left[\left(1 - \frac{\omega^2}{k_z^2} C_{1p} \right) g_v D_{1n} + \left(1 - \frac{\omega^2}{k_z^2} C_{2p} \right) \frac{g_\rho}{2} D_{2n} \right], \tag{B.4}$$

$$a_{15} = \sum_{\nu,s} \left(1 - \frac{\omega^2}{k_z^2} \right) \frac{e^2}{2\pi^2 \omega_A^2} \frac{eB}{V_F^p (s_p^2 - 1)}, \tag{B.5}$$

$$a_{21} = \frac{\bar{m}_p}{\tilde{m}_p} a_{11} - 1, \quad a_{22} = \frac{\bar{m}_p}{\tilde{m}_p} (a_{12} + 1), \tag{B.6}$$

$$a_{23} = \frac{\bar{m}_p}{\tilde{m}_p} a_{13}, \quad a_{24} = \frac{\bar{m}_p}{\tilde{m}_p} a_{14}, \quad a_{25} = \frac{\bar{m}_p}{\tilde{m}_p} a_{15}, \tag{B.7}$$

$$a_{31} = \sum_s \frac{g_s M^*}{(2\pi)^2} \frac{eB}{\omega_s^2 \epsilon_F^p} \epsilon_F^n P_F^n L^*(s_n), \tag{B.8}$$

$$a_{32} = -\sum_s \left[\left(1 - \frac{\omega^2}{k_z^2} C_{1n}\right) g_v D_{1p} - \left(1 - \frac{\omega^2}{k_z^2} C_{2n}\right) \frac{g_\rho}{2} D_{2p} \right] \times \frac{eB}{4\pi^2} \epsilon_F^n P_F^n L(s_n), \tag{B.9}$$

$$a_{33} = \sum_s \frac{g_s M^*}{(2\pi)^2} \frac{P_F^n}{\omega_s^2} L^*(s_n), \tag{B.10}$$

$$a_{34} = -\sum_s \left[\left(1 - \frac{\omega^2}{k_z^2} C_{1n}\right) g_v D_{1n} - \left(1 - \frac{\omega^2}{k_z^2} C_{2n}\right) \frac{g_\rho}{2} D_{2n} \right] \times \frac{\epsilon_F^n P_F^n L(s_n)}{4\pi^2} - 1, \tag{B.11}$$

$$a_{35} = 0, \tag{B.12}$$

$$a_{41} = a_{31} \frac{H^*(s_n)}{L^*(s_n)}, \quad a_{42} = a_{32} \frac{H(s_n)}{L(s_n)}, \tag{B.13}$$

$$a_{43} = a_{33} \frac{H^*(s_n)}{L^*(s_n)} - 1, \tag{B.14}$$

$$a_{44} = (a_{34} + 1) \frac{H(s_n)}{L(s_n)}, \quad a_{45} = 0, \tag{B.15}$$

$$a_{51} = a_{53} = a_{54} = 0, \tag{B.16}$$

$$a_{52} = \sum_{\nu,s} \left(1 - \frac{\omega^2}{k_z^2}\right) \frac{e^2}{2\pi^2 \omega_A^2} \frac{eB}{V_F^e (s_e^2 - 1)}, \tag{B.17}$$

$$a_{55} = -\sum_{\nu,s} \left(1 - \frac{\omega^2}{k_z^2}\right) \frac{e^2}{2\pi^2 \omega_A^2} \frac{eB}{V_F^e (s_e^2 - 1)} - 1 \tag{B.18}$$

where $\tilde{m}_p = \bar{m}_p + s\mu_N \kappa_p B$, $\omega_s^2 = \omega^2 - k_z^2 - m_{s,eff}^2$, $\omega_A^2 = \omega^2 - k_z^2$, and $s_i = \frac{\omega}{\omega_{0i}}$, $i = p, n, e$.

The remaining coefficients are given by

$$G_{\phi_p} = \frac{g_s M^* \bar{m}_p}{\epsilon_F^p (\bar{m}_p + s\mu_N \kappa_p B)}, \tag{B.19}$$

$$G_{\phi_n} = \frac{g_s M^*}{\epsilon_F^n} \left(1 - \frac{s\mu_N \kappa_n B}{\sqrt{M^{*2} + P_F^{n2}(1 - x^2)}}\right), \tag{B.20}$$

$$C_{1i} = 1 - \frac{\tau_i g_\rho \chi}{2 g_v \omega_\rho^2}, \tag{B.21}$$

$$C_{2i} = 1 - \frac{2\tau_i g_v \chi}{g_\rho \omega_v^2}, \tag{B.22}$$

$$D_{1i} = \frac{\tau_i g_\rho \chi}{2D_\nu} + \frac{g_v \omega_\rho^2}{D_\nu}, \tag{B.23}$$

$$D_{2i} = \frac{g_v \chi}{D_\nu} + \frac{\tau_i g_\rho \omega_v^2}{2D_\nu}, \tag{B.24}$$

$$D_\nu = \omega_v^2 \omega_\rho^2 - \chi, \tag{B.25}$$

$$L(s_n) = \int_{-1}^{1} \frac{x}{(s_n - x)} dx, \quad L^*(s_n) = \int_{-1}^{1} \frac{G_{\phi_n} x dx}{(s_n - x)}, \tag{B.26}$$

$$H(s_n) = \int_{-1}^{1} \left(1 - \frac{s\mu_N \kappa_n B}{\sqrt{M_n^{*2} + P_F^{n2}(1 - x^2)}} \right) \frac{x dx}{(s_n - x)}, \tag{B.27}$$

$$H^*(s_n) = \int_{-1}^{1} \left(1 - \frac{s\mu_N \kappa_n B}{\sqrt{M_n^{*2} + P_F^{n2}(1 - x^2)}} \right) \frac{G_{\phi_n} x dx}{(s_n - x)}. \tag{B.28}$$

Appendix C

Some useful integrals

The following integrals are used in the calculations of the thermodynamical spinodals for finite temperature:

$$\int \frac{p^2}{1+e^{(\sqrt{p^2+M^{*2}}-\nu)/T}} \frac{M^*}{\sqrt{p^2+M^{*2}}} dp$$

$$\underline{\underline{p=\sqrt{y^2-M^{*2}}}} \int \frac{y^2-M^{*2}}{1+e^{(y-\nu)/T}} \frac{M^*}{y} d(\sqrt{y^2-M^{*2}})$$

$$= \int \frac{\sqrt{y^2-M^{*2}}\cdot y}{1+e^{(y-\nu)/T}} \frac{M^*}{y} dy$$

$$= \int \frac{\sqrt{y^2-M^{*2}}\cdot M^*}{1+e^{(y-\nu)/T}} dy$$

$$\underline{\underline{y=x+M^*}} \int \frac{\sqrt{x^2+2M^*x}\cdot M^*}{1+e^{[x-(\nu-M^*)]/T}} dx$$

$$= \sqrt{2}M^{*\frac{3}{2}} \int \frac{\sqrt{x}\sqrt{1+\frac{x}{2M^*}}}{1+e^{[x-(\nu-M^*)]/T}} dx$$

$$\underline{\underline{x=Tz}} \sqrt{2}M^{*\frac{3}{2}} \int \frac{\sqrt{Tz}\sqrt{1+\frac{Tz}{2M^*}}}{1+e^{[z-(\nu-M^*)/T]}} d(Tz)$$

$$= \sqrt{2}M^{*\frac{3}{2}}T^{\frac{3}{2}} \int \frac{z^{\frac{1}{2}}\sqrt{1+\frac{Tz}{2M^*}}}{1+e^{[z-(\nu-M^*)/T]}} dz, \qquad \text{(C.1)}$$

$$\int \frac{1}{1+e^{(\sqrt{p^2+M^2}-\nu)/T}} \frac{M^*}{\sqrt{p^2+M^2}} dp$$

$$
\begin{aligned}
&\overset{p=\sqrt{y^2-M^2}}{=\!=\!=} \int \frac{1}{1+e^{(y-\nu)/T}} \frac{M^*}{y} d(\sqrt{y^2-M^2}) \\
&= \int \frac{1}{1+e^{(y-\nu)/T}} \frac{M^*}{y} \frac{y}{\sqrt{y^2-M^2}} dy \\
&= M^* \int \frac{1}{1+e^{(y-\nu)/T}} \frac{1}{\sqrt{y^2-M^2}} dy \\
&\overset{y=x+M}{=\!=\!=} M^* \int \frac{1}{1+e^{[x-(\nu-M)]/T}} \frac{1}{\sqrt{x^2+2Mx}} dx \\
&\overset{x=Tz}{=\!=\!=} M^* \int \frac{1}{1+e^{[z-(\nu-M)/T]}} \frac{1}{\sqrt{(Tz)^2+2MTz}} d(Tz) \\
&= \frac{M^* T^{\frac{1}{2}}}{\sqrt{2M}} \int \frac{z^{-\frac{1}{2}}(1+\frac{T}{2M}z)^{-\frac{1}{2}}}{1+e^{[z-(\nu-M)/T]}} dz,
\end{aligned} \tag{C.2}
$$

$$
\begin{aligned}
&\int \frac{p^2}{1+e^{(\sqrt{p^2+M^{*2}}-\nu)/T}} dp \\
&\overset{p=\sqrt{y^2-M^{*2}}}{=\!=\!=} \int \frac{y^2-M^{*2}}{1+e^{(y-\nu)/T}} d(\sqrt{y^2-M^{*2}}) \\
&= \int \frac{y^2-M^{*2}}{1+e^{(y-\nu)/T}} \frac{1}{2} \frac{2y}{\sqrt{y^2-M^{*2}}} dy \\
&= \int \frac{\sqrt{y^2-M^{*2}} \cdot y}{1+e^{(y-\nu)/T}} dy \\
&\overset{y=x+M^*}{=\!=\!=} \int \frac{\sqrt{x^2+2M^*x} \cdot (x+M^*)}{1+e^{[x-(\nu-M^*)]/T}} dx \\
&= \int \frac{(x+M^*)\sqrt{x}\sqrt{2M^*}\sqrt{1+\frac{x}{2M^*}}}{1+e^{[x-(\nu-M^*)]/T}} dx \\
&= \sqrt{2M^*} \int \frac{(x^{\frac{3}{2}}+M^*x^{\frac{1}{2}})\sqrt{1+\frac{x}{2M^*}}}{1+e^{[x-(\nu-M^*)]/T}} dx \\
&\overset{x=Tz}{=\!=\!=} \sqrt{2M^*} \int \frac{[(Tz)^{\frac{3}{2}}+M^*(Tz)^{\frac{1}{2}}]\sqrt{1+\frac{Tz}{2M^*}}}{1+e^{[z-(\nu-M^*)/T]}} d(Tz) \\
&= \sqrt{2}M^{*\frac{1}{2}}T^{\frac{5}{2}} \int \frac{z^{\frac{3}{2}}\sqrt{1+\frac{1}{2}\frac{T}{M^*}z}}{1+e^{[z-(\nu-M^*)/T]}} dz + \sqrt{2}M^{*\frac{3}{2}}T^{\frac{3}{2}} \int \frac{z^{\frac{1}{2}}\sqrt{1+\frac{1}{2}\frac{T}{M^*}z}}{1+e^{[z-(\nu-M^*)/T]}} dz,
\end{aligned} \tag{C.3}
$$

$$\int \frac{1}{1+e^{(\sqrt{p^2+M^2}-\nu)/T}}dp$$

$$\overset{p=\sqrt{y^2-M^2}}{=\!=\!=} \int \frac{1}{1+e^{(y-\nu)/T}} d(\sqrt{y^2-M^2})$$

$$= \int \frac{1}{1+e^{(y-\nu)/T}} \frac{1}{2} \frac{2y}{\sqrt{y^2-M^2}} dy$$

$$= \int \frac{y}{1+e^{(y-\nu)/T}} \frac{1}{\sqrt{y^2-M^2}} dy$$

$$\overset{y=x+M}{=\!=\!=} \int \frac{x+M}{1+e^{[x-(\nu-M)]/T}} \frac{1}{\sqrt{x^2+2Mx}} dx$$

$$\overset{x=Tz}{=\!=\!=} \int \frac{Tz+M}{1+e^{[z-(\nu-M)/T]}} \frac{1}{\sqrt{(Tz)^2+2MTz}} d(Tz)$$

$$= \int \frac{Tz+M}{1+e^{[z-(\nu-M)/T]}} \sqrt{T} z^{-\frac{1}{2}} \frac{1}{\sqrt{2M}} (1+\frac{T}{2M}z)^{-\frac{1}{2}} dz$$

$$= \frac{1}{\sqrt{2M}} T^{\frac{3}{2}} \int \frac{z^{\frac{1}{2}}(1+\frac{T}{2M}z)^{-\frac{1}{2}}}{1+e^{[z-(\nu-M)/T]}} dz + \frac{\sqrt{M}}{\sqrt{2}} T^{\frac{1}{2}} \int \frac{z^{-\frac{1}{2}}(1+\frac{T}{2M}z)^{-\frac{1}{2}}}{1+e^{[z-(\nu-M)/T]}} dz. \quad \textbf{(C.4)}$$

List of Figures

1.1 The schematic picture of the structure of a neutron star, taken from [Sharma, 2013]. 2

1.2 The nuclear pasta phases. From left to right: droplets, rods, cross-rods, slabs, tubes and bubbles. Figure taken from [Pais and Stone, 2012]. 3

1.3 Dynamical and thermodynamical instabilities. The transition densities are shown for β-equilibrium matter by square and dot points. 7

1.4 Correlation between the symmetry energy slope L and the crust-core transition density, ρ_t, taken from Ref. [Vidaña et al., 2009]. The transition density is shown for a wide number of nuclear models, in particular, phenomenological approaches: non-relativistic Skyrme forces (black squares), relativistic mean-field (RMF) models (blue triangles for NLWM and red triangles for DDH), QMC (stars), and the microscopic BHF calculation with Argonne V18 potential with a three-body force of the Urbana type (circle). The blue line is a linear fit. 9

1.5 $P\dot{P}$ diagram for the known magnetars and other objects. Objects with a large magnetic field lie on the top right corner. Figure taken from [Harding, 2013]. 14

2.1 Energy per particle for symmetric nuclear matter and neutron matter. The EoS of neutron matter presents a minimum at $\sim 0.6\rho_0$ that is considered unphysical. 20

3.1 Free energy density minus $E_{B0}\rho$, where E_{B0} is the energy per particle at saturation, and ρ is the baryonic density. Points A and B belong to the binodal, A' and B' are spinodal points, and in C the free energy density is concave, therefore, the system is unstable. Figure taken from [Müller and Serot, 1995]. 42

4.1 Dynamical spinodals attained for different momentum transfers k, for $B^* = 5 \times 10^3$, without AMM, and considering the NL3 model. The green line represents the corresponding $B = 0$ spinodal section. 47

4.2 Dynamical spinodals for the NL3 parametrization, for different magnetic field intensities and momentum transfer $k = 50$ MeV. The three panels of the right have been obtained including the AMM, while the last panel gives the spinodal not taking into account the AMM of both protons and neutrons. 48

4.3 The proton chemical potential as a function of the proton density for $B^* = 10^4$, and $T = 0$, with the neutron density fixed at $\rho_n = 0.05$ fm^{-3}. 49

4.4 Dynamical spinodal for NL3$\omega\rho$, a momentum transfer of $k = 75$ MeV, and $B^* = 10^4$ (red), $B^* = 10^3$ (blue), and $B^* = 10^2$ (green) with (top) and without AMM (bottom). A comparison with the $B = 0$ (black lines) results is also made. 50

4.5 Dynamical spinodal for NL3$\omega\rho$, a momentum transfer of $k = 75$ MeV, with AMM (green) and without AMM (red), for $B^* = 10^4$ (top), $B^* = 10^3$ (middle), and $B^* = 10^2$ (bottom). A comparison with the $B = 0$ (black lines) results is also made. The EoS for $\beta-$equilibrium matter is also shown. 52

4.6 Growth rates, $|\omega|$, as a function of the momentum, k, for NL3$\omega\rho$, a proton fraction of $y_p = 0.035$, and $B^* = 10^2$ (red), $B^* = 10^3$ (black), and $B^* = 10^4$ (blue) with AMM (solid) and without AMM (dashed lines), for a fixed baryonic density of $\rho = 0.04$ fm^{-3} (top), $\rho = 0.08$ fm^{-3} (middle), and $\rho = 0.09$ fm^{-3} (bottom). The growth rates for $B^* = 10^2$ in the bottom panel are multiplied by a factor of 10 and are obtained for $\rho = 0.0903$ fm^{-3}. 54

4.7 Largest growth rate (top), the corresponding estimated size of the clusters (middle), and the density fluctuation ratio $\delta\rho_p/\delta\rho_n$ (bottom) versus density, for different proton fractions y_p, and $B^* = 10^3$, with (right) and without (left) AMM, for the NL3 model. 57

4.8 Largest growth rate $\Gamma = |\omega|$ (top panels), the corresponding half-wavelength (middle panels) and the proton-neutron density fluctuation ratio (bottom panels) versus density, for different magnetic field intensities and matter with $y_p = 0.02$ for NL3 and $y_p = 0.035$ for NL3$\omega\rho$. The black curve corresponds to the $B = 0$ results. 58

4.9 Thermodynamical spinodals for different values of magnetic fields in the absence of the AMM for the NL3 model. All sections extend to the same point at $\rho_p = 0$. 60

4.10 Largest growth rate (top panels), the corresponding half-wavelength (middle panels), and the proton-neutron density fluctuation ration (bottom panels) versus density for NL3$\omega\rho$, with a proton fraction of $y_p = 0.035$ for the whole density range, without (left panels) and with (right panels) AMM. Three different values of B are considered: $B^* = 10^2$ (red), $B^* = 10^3$ (green), and $B^* = 10^4$ (blue). A comparison with the $B = 0$ (black lines) results is also made. 62

4.11 Largest growth rate (top panels), the corresponding half-wavelength (middle panels), and the proton-neutron density fluctuation ratio (bottom panels) versus density for NL3$\omega\rho$, and a magnetic field of $B^* = 10^3$, without (left panels) and with (right panels) AMM. Results with the $B = 0$ (black solid lines) calculation are also shown for comparison. The blue points correspond to a calculation with a proton fraction equal to the one found in $\beta-$equilibrium matter, above $\rho_t = 0.0843$ fm^{-3}, the $B = 0$ crust-core transition density. The grey points correspond to a fixed proton fraction of 0.035 in the whole density range. 64

5.1 The dynamical and thermodynamical spinodals for $B^* = 10^4$ and $T = 0$ MeV for the NL3$\omega\rho$ model with AMM. . . . 70

5.2 Details of the crossing of the thermodynamical spinodal with the EoS (red solid line) for NL3$\omega\rho$ with $B^* = 10^3$, considering different temperatures, and taking AMM$= 0$. 71

5.3 The transition densities, ρ_1 (empty) and ρ_2 (full), (top), the crust thickness, ΔR (full) and $\Delta R^* = R(0) - R(\rho_1)$ (empty), (middle), and the crust fractional momentum of inertia (bottom), calculated with (ρ_1, P_1) (empty) and with (ρ_2, P_2) (full), obtained with the $L = 55$ MeV model, at $T = 0$, for several values of B^*, and using the thermodynamical spinodal formalism with (squares) and without AMM (circles), and the dynamical spinodal with AMM (triangles). 74

5.4 Thermodynamical spinodals for different temperatures, and taking $B^* = 10^4$ (top) and $B^* = 10^5$ (bottom) for the NL3 model without AMM. The lack of definition for the smaller fields at low proton density is a numerical constraint that would be overcome with longer CPU time. 76

5.5 Thermodynamical spinodals for several temperatures for (a) NL3$\omega\rho$ with $B = 0$, and (b) NL3 with $B^* = 10^4$ without AMM. The black solid line is the β-equilibrium equation of state at $B = T = 0$. 78

5.6 The transition densities, ρ_1 (empty) and ρ_2 (full), (top), the crust thickness (middle), and the momentum of inertial crustal fraction (bottom) for NL3$\omega\rho$, with $L = 55$ MeV, for several values of B^* and T. The thermodynamical spinodal formalism without AMM has been used. The horizontal black lines show the location of the respective quantities at zero temperature and zero magnetic field. . 81

5.7 $\delta\rho_p^-/\delta\rho_n^-$ plotted as a function of the proton fraction with $T = 0$ MeV and $\rho = 0.06$ fm^{-3}, for different values of the magnetic fields, for NL3 model with (bottom) and without (top) AMM. The dashed line is the ratio between the proton and neutron densities. 84

5.8 $\delta\rho_p^-/\delta\rho_n^-$ plotted as a function of the density with $y_p = 0.2$ for different values of the magnetic fields with (bottom) and without (top) AMM for the NL3 model. 86

5.9 $\delta\rho_p^-/\delta\rho_n^-$ plotted as a function of the proton fraction for $B^* = 10^5$ (top) and $B^* = 10^4$ (bottom), with $\rho = 0.06$ fm^{-3}, for several temperatures, and for the NL3 model. The curve for $T = 0$ and $B = 0$ is also shown as a blue line in the figure. 88

5.10 $\delta\rho_p^-/\delta\rho_n^-$ plotted as a function of the density for $B^* = 10^5$ (top) and $B^* = 10^4$ (bottom) with $y_p = 0.2$ for several temperatures, and for the NL3 model. The curve for $T = 0$ and $B = 0$ is also shown as a blue line in the figure. . . . 89

List of Tables

1.1 Nuclear matter saturation properties of NL3 and NL3$\omega\rho$ models. 12

4.1 Transition densities and pressures for the magnetic fields considered in this study, together with the correspondent fractional moment of inertia of the neutron star crust, for NL3$\omega\rho$, with $L = 55$ MeV, for a star of $M = 1.4$ $M_\odot$ and $R = 13.734$ km. Also shown are the crust thicknesses, ΔR, the thickness due to the inhomogeneous region found when $B \neq 0$, $\Delta R' = R(\rho_1) - R(\rho_2)$, and the difference to the $B = 0$ result, $\Delta R_B = \Delta R - \Delta R(B = 0)$. The results shown take into account the AMM. The transition densities are calculated when $|\omega| = 0$ (see top panels of Figs. 4.10 and 4.11, and the text for more details). The values for ρ_2 correspond to the calculations with a $\beta-$equilibrium matter proton fraction. 66

5.1 Transition densities and pressures calculated within the thermodynamical and dynamical spinodals formalism at $B = T = 0$, and considering four different values of L, with the correspondent fractional moment of inertia of the neutron star crust, for a star of $M = 1.4$ $M_\odot$. Also shown are the crust thicknesses, ΔR, and the radius of a 1.4 solar mass star, $R_{1.4}$. 72

5.2 Transition densities and pressures calculated at $T = 0$ within the formalism of the thermodynamical spinodal with and without AMM, for $50 < B^* < 10^4$ and $L = 55$ MeV, together with the correspondent fractional moment of inertia of the neutron star crust, for a star of $M = 1.4$ $M_\odot$ and $R = 13.734$ km. Also shown are the crust thicknesses, ΔR, the thickness due to the inhomogeneous region found when $B \neq 0$, $\Delta R' = R(\rho_1) - R(\rho_2)$, and the difference to the $B = 0$ result, $\Delta R_B = \Delta R - \Delta R(B = 0)$. 73
5.3 Transition densities and pressures for the magnetic fields considered in this study and several temperatures, together with the crust thicknesses, ΔR, the thickness due to the inhomogeneous region found when $B \neq 0$, $\Delta R' = R(\rho_1) - R(\rho_2)$, and the correspondent fractional moment of inertia of the neutron star crust, obtained from the thermodynamical spinodal without AMM and with $L = 55$ MeV, for a star of $M = 1.4$ $M_\odot$ and $R = 13.734$ km. 80
5.4 *(continuation)* 82

Bibliography

[Abbott et al., 2016] Abbott et al., B. P. (2016). Phys. Rev. Lett., 116:061102.

[Alam et al., 2017] Alam, N., Pais, H., Providência, C., and Agrawal, B. K. (2017). Phys. Rev. C, 95:055808.

[Andersson et al., 2012] Andersson, N., Glampedakis, K., Ho, W. C. G., and Espinoza, C. M. (2012). Phys. Rev. Lett., 109:241103.

[Antoniadis et al., 2013] Antoniadis, J., Freire, P. C. C., Wex, N., Tauris, T. M., Lynch, R. S., van Kerkwijk, M. H., Kramer, M., Bassa, C., Dhillon, V. S., Driebe, T., Hessels, J. W. T., Kaspi, V. M., Kondratiev, V. I., Langer, N., Marsh, T. R., McLaughlin, M. A., Pennucci, T. T., Ransom, S. M., Stairs, I. H., van Leeuwen, J., Verbiest, J. P. W., and Whelan, D. G. (2013). Science, 340:448.

[Aparicio, 1998] Aparicio, J. M. (1998). Astrophys. J. Supp. S., 117:627.

[Archibald et al., 2013] Archibald, R. F., Kaspi, V. M., Ng, C. Y., Gourgouliatos, K. N., Tsang, D., Scholz, P., Beardmore, A. P., Gehrels, N., and Kennea, J. A. (2013). Nature, 497:591.

[Avancini et al., 2006] Avancini, S. S., Brito, L., Chomaz, P., Menezes, D. P., and Providência, C. (2006). Phys. Rev. C, 74:024317.

[Avancini et al., 2009] Avancini, S. S., Brito, L., Marinelli, J. R., Menezes, D. P., de Moraes, M. M. W., Providência, C., and Santos, A. M. (2009). Phys. Rev. C, 79:035804.

[Avancini et al., 2005] Avancini, S. S., Brito, L., Menezes, D. P., and Providência, C. (2005). Phys. Rev. C, 71:044323.

[Avancini et al., 2012] Avancini, S. S., C. C. Barros, J., Brito, L., Chiacchiera, S., Menezes, D. P., and Providência, C. (2012). Phys. Rev. C, 85:035806.

[Avancini et al., 2010] Avancini, S. S., Chiacchiera, S., Menezes, D. P., and Providência, C. (2010). Phys. Rev. C, 82:055807.

[Avancini et al., 2008] Avancini, S. S., Menezes, D. P., Alloy, M. D., Marinelli, J. R., Moraes, M. M. W., and Providência, C. (2008). Phys. Rev. C, 78:015802.

[Baade and Zwicky, 1934] Baade, W. and Zwicky, F. (1934). Phys. Rev., 46:76.

[Boguta and Bodmer, 1977] Boguta, J. and Bodmer, A. R. (1977). Nucl. Phys. A, 292:413.

[Bonche and Vautherin, 1981] Bonche, P. and Vautherin, D. (1981). Nucl. Phys. A, 372:496.

[Bonche and Vautherin, 1982] Bonche, P. and Vautherin, D. (1982). Astron. Astrophys., 112:268.

[Braithwaite and Spruit, 2006] Braithwaite, J. and Spruit, H. C. (2006). Astron. Astrophys., 450:1097.

[Brink and Boeker, 1967] Brink, D. M. and Boeker, E. (1967). Nucl. Phys. A, 91:1.

[Brito et al., 2006] Brito, L., Providência, C., Santos, A. M., Avancini, S. S., Menezes, D., and Chomaz, P. (2006). Phys. Rev. C, 74:045801.

[Broderick et al., 2000] Broderick, A., Prakash, M., and Lattimer, J. M. (2000). Astrophys. J., 537:351.

[Broderick et al., 2002] Broderick, A., Prakash, M., and Lattimer, J. M. (2002). Phys. Lett. B, 531:167.

[Brown and Jackson, 1976] Brown, G. E. and Jackson, A. D. (1976). The Nucleon-Nucleon Interaction. North-Holland Publishing, Amsterdam.

[C. Wen, 2006] C. Wen (2006). Master thesis, Jilin University.

[Cardall et al., 2001] Cardall, C. Y., Prakash, M., and Lattimer, J. M. (2001). Astrophys. J., 554:332.

[Carriere and C. J. Horowitz, 2003] Carriere, J. and C. J. Horowitz, J. P. (2003). Astrophys. J., 593:463.

[Centelles et al., 2009] Centelles, M., Roca-Maza, X., Viñas, X., and Warda, M. (2009). Phys. Rev. Lett., 102:122502.

[Chabanat et al., 1998] Chabanat, E., Bonche, P., Haensel, P., Meyer, J., and Schaeffer, R. (1998). Nucl. Phys. A, 635:231.

[Chakrabarty et al., 1997] Chakrabarty, S., Bandyopadhyay, D., and Pal, S. (1997). Phys. Rev. Lett., 78:2898.

[Chamel, 2012] Chamel, N. (2012). Phys. Rev. C, 85:035801.

[Chamel and Haensel, 2008] Chamel, N. and Haensel, P. (2008). Living Rev. Relativity, 11:10.

[Chamel et al., 2013] Chamel, N., Page, D., and Reddy, S. (2013). Phys. Rev. C, 87:035803.

[Chamel et al., 2015] Chamel, N., Stoyanov, Z. K., Mihailov, L. M., Mutafchieva, Y. D., Pavlov, R. L., and Velchev, C. J. (2015). Phys. Rev. C, 91:065801.

[Chen, 2017] Chen, Y. J. (2017). Phys. Rev. C, 95:035807.

[Chomaz, 2001] Chomaz, P. (2001). Nucl. Phys. A, 681:199.

[Chomaz et al., 2004] Chomaz, P., Colonna, M., and Randrup, J. (2004). Phys. Rep., 389:263.

[Chomaz and Gulminelli, 1999] Chomaz, P. and Gulminelli, F. (1999). Phys. Lett. B, 447:221.

[Colonna et al., 2002] Colonna, M., Chomaz, P., and Ayik, S. (2002). Phys. Rev. Lett., 88:122701.

[Condon and Ransom, 2016] Condon, J. J. and Ransom, S. M. (2016). Essential Radio Astronomy. Princeton University Press.

[Danielewicz et al., 2002] Danielewicz, P., Lacey, R., and Lynch, W. G. (2002). Science, 298:1592.

[Dorso et al., 2012] Dorso, C. O., Giménez Molinelli, P. A., and López, J. A. (2012). Phys. Rev. C, 86:055805.

[Ducoin et al., 2010] Ducoin, C., Margueron, J., and Providência, C. (2010). Eur. Phys. Lett., 91:32001.

[Ducoin et al., 2011] Ducoin, C., Margueron, J., Providência, C., and Vidaña, I. (2011). Phys. Rev. C, 83:045810.

[Ducoin et al., 2008] Ducoin, C., Providência, C., Santos, A. M., Brito, L., and Chomaz, P. (2008). Phys. Rev. C, 78:055801.

[Duncan, 2000] Duncan, R. C. (2000). AIP Conf. Proc., 526:830.

[Duncan and Thompson, 1992] Duncan, R. C. and Thompson, C. (1992). Astrophys. J., 392:9.

[Dutra et al., 2014] Dutra, M., Lourenço, O., Avancini, S. S., Carlson, B. V., Delfino, A., Menezes, D. P., Providência, C., Typel, S., and Stone, J. R. (2014). Phys. Rev. C, 90:055203.

[Dutra et al., 2012] Dutra, M., Lourenço, O., Sá Martins, J. S., Delfino, A., Stone, J. R., and Stevenson, P. D. (2012). Phys. Rev. C, 85:035201.

[Fattoyev and Piekarewicz, 2010] Fattoyev, F. J. and Piekarewicz, J. (2010). Phys. Rev. C, 82:025810.

[Fortin et al., 2016] Fortin, M., Providência, C., Raduta, A. R., Gulminelli, F., Zdunik, J. L., Haensel, P., and Bejger, M. (2016). Phys. Rev. C, 94:035804.

[Frieben and Rezzolla, 2012] Frieben, J. and Rezzolla, L. (2012). Mon. Not. R. Astron. Soc., 427:3406.

[Gallo et al., 2011] Gallo, L. D., Oertel, M., and M.Urban (2011). Phys. Rev. C, 84:045801.

[Gandolfi et al., 2012] Gandolfi, S., Carlson, J., and Reddy, S. (2012). Phys. Rev. C, 85:032801.

[Glendenning, 2000] Glendenning, N. K. (2000). Compact Stars. Springer-Verlag, New-York.

[Gögelein and Müther, 2007] Gögelein, P. and Müther, H. (2007). Phys. Rev. C, 76:024312.

[Goriely et al., 2010] Goriely, S., Chamel, N., and Pearson, J. M. (2010). Phys. Rev. C, 82:035804.

[Goriely et al., 2013] Goriely, S., Chamel, N., and Pearson, J. M. (2013). Phys. Rev. C, 88:024308.

[Greco et al., 2003] Greco, V., Colonna, M., Di Toro, M., and Matera, F. (2003). Phys. Rev. C, 67:015203.

[Grill et al., 2012] Grill, F., Providência, C., and Avancini, S. S. (2012). Phys. Rev. C, 85:055808.

[Haensel, 1978] Haensel, P. (1978). Nucl. Phys. A, 301:53.

[Harding, 2013] Harding, A. K. (2013). Front. Phys., 8:679.

[Harding and Lai, 2006] Harding, A. K. and Lai, D. (2006). Rep. Prog. Phys., 69:2631.

[Hartle, 1967] Hartle, J. B. (1967). Astrophys. J., 150:1005.

[Hartle and Thorne, 1968] Hartle, J. B. and Thorne, K. S. (1968). Astrophys. J., 153:807.

[Hashimoto et al., 1984] Hashimoto, M., Seki, H., and Yamada, M. (1984). Prog. Theor. Phys., 71:320.

[Hebeler et al., 2013] Hebeler, K., Lattimer, J. M., Pethick, C. J., and Schwenk, A. (2013). Astrophys. J., 773:11.

[Hempel and Schaffner-Bielich, 2010] Hempel, M. and Schaffner-Bielich, J. (2010). Nucl. Phys. A, 837:210.

[Hempel et al., 2011] Hempel, M., Schaffner-Bielich, J., Typel, S., and Röpke, G. (2011). Phys. Rev. C, 84:055804.

[Hewish et al., 1968] Hewish, A., Bell, S. J., Pilkington, J. D., Scott, P. F., and Collins, R. A. (1968). Nature, 217:709.

[Horowitz et al., 2015] Horowitz, C. J., Berry, D. K., Briggs, C. M., Caplan, M. E., Cumming, A., and Schneider, A. S. (2015). Phys. Rev. Lett., 114:031102.

[Horowitz et al., 2005] Horowitz, C. J., Pérez-García, M. A., Berry, D. K., and Piekarewicz, J. (2005). Phys. Rev. C, 72:035801.

[Horowitz et al., 2004a] Horowitz, C. J., Perez-Garcia, M. A., Carriere, J., Berry, D. K., and Piekarewicz, J. (2004a). Phys. Rev. C, 70:065806.

[Horowitz et al., 2004b] Horowitz, C. J., Perez-Garcia, M. A., and Piekarewicz, J. (2004b). Phys. Rev. C, 69:045804.

[Horowitz et al., 2004c] Horowitz, C. J., Pérez-García, M. A., and Piekarewicz, J. (2004c). Phys. Rev. C, 69:045804.

[Horowitz and Piekarewicz, 2001a] Horowitz, C. J. and Piekarewicz, J. (2001a). Phys. Rev. Lett., 86:5647.

[Horowitz and Piekarewicz, 2001b] Horowitz, C. J. and Piekarewicz, J. (2001b). Phys. Rev. C, 64:062802.

[Horowitz et al., 2001] Horowitz, C. J., Pollock, S. J., Souder, P. A., and Michaels, R. (2001). Phys. Rev. C, 63:025501.

[Jin et al., 1989] Jin, X., Zhuo, Y., and Zhang, X. (1989). Nucl. Phys. A, 506:655.

[Khan et al., 2012] Khan, E., Margueron, J., and Vidaña, I. (2012). Phys. Rev. Lett., 109:092501.

[Khan et al., 2005] Khan, E., Sandulescu, N., and Giai, N. V. (2005). Phys. Rev. C, 71:042801(R).

[Kiuchi and Yoshida, 2008] Kiuchi, K. and Yoshida, S. (2008). Phys. Rev. D, 78:044045.

[Ko and Li, 1988] Ko, C. M. and Li, Q. (1988). Phys. Rev. C, 37:2270.

[Ko et al., 1987] Ko, C. M., Li, Q., and Wang, R. (1987). Phys. Rev. Lett., 59:1084.

[Köhler, 1965a] Köhler, H. S. (1965a). Phys. Rev., 137:1145.

[Köhler, 1965b] Köhler, H. S. (1965b). Phys. Rev., 138:831.

[Kuksenok et al., 2006] Kuksenok, O., Travasso, R. D. M., and Balazs, A. C. (2006). Phys. Rev. E, 74:011502.

[Kumar et al.,] Kumar, K., Michaels, R., Souder, P. A., and Urciuoli, G. M. http://hallaweb.jlab.org/parity/prex.

[Lai and Shapiro, 1991] Lai, D. and Shapiro, S. L. (1991). Astrophys. J., 383:745.

[Lalazissis et al., 1997] Lalazissis, G. A., König, J., and Ring, P. (1997). Phys. Rev. C, 55:540.

[Lamb et al., 1983] Lamb, D. Q., Lattimer, J. M., Pethick, C. J., and Ravenhall, D. G. (1983). Nucl. Phys. A, 411:449.

[Landau and Lifshitz, 1980] Landau, L. D. and Lifshitz, E. M. (1980). Statistical Physics — Part 1. Pergamon Press, third edition.

[Lassaut et al., 1987] Lassaut, M., Flocard, H., Bonche, P., Heenen, P. H., and Suraud, E. (1987). Astron. Astrophys., 183:L3.

[Lattimer and Lim, 2013] Lattimer, J. M. and Lim, Y. (2013). Astrophys. J., 771:51.

[Lattimer and Prakash, 2000] Lattimer, J. M. and Prakash, M. (2000). Phys. Rep., 333:121.

[Lattimer and Prakash, 2001] Lattimer, J. M. and Prakash, M. (2001). Astrophys. J., 550:426.

[Lattimer and Prakash, 2007] Lattimer, J. M. and Prakash, M. (2007). Phys. Rep., 442:109.

[Lattimer and Swesty, 1991] Lattimer, J. M. and Swesty, F. D. (1991). Nucl. Phys. A, 535:331.

[Lay, 2012] Lay, V. (2012). Master thesis, University of Coimbra.

[Lenk and Pandharipande, 1986] Lenk, R. J. and Pandharipande, V. R. (1986). Phys. Rev. C, 34:177.

[Lenk et al., 1990] Lenk, R. J., Schlagel, T. J., , and Pandharipande, V. R. (1990). Phys. Rev. C, 42:372.

[Li et al., 2008] Li, B.-A., Chen, L.-W., and Ko, C. M. (2008). Phys. Rep., 464:113.

[Li et al., 2016] Li, X., Levin, Y., and Beloborodov, A. M. (2016). Astrophys. J., 833:189.

[Lim and Horowitz, 1989] Lim, K. and Horowitz, C. J. (1989). Nucl. Phys. A, 501:729.

[Lima et al., 2013] Lima, R. C. R., Avancini, S. S., and Providência, C. (2013). Phys. Rev. C, 88:035804.

[Link et al., 1999] Link, B., Epstein, R. I., and Lattimer, J. M. (1999). Phys. Rev. Lett., 83:3362.

[Lorenz et al., 1993] Lorenz, C. P., Ravenhall, D. G., and Pethick, C. J. (1993). Phys. Rev. Lett., 70:379.

[Machleidt and Slaus, 2001] Machleidt, R. and Slaus, I. (2001). J. Phys. G, 27:69.

[Margueron and Chomaz, 2003] Margueron, J. and Chomaz, P. (2003). Phys. Rev. C, 67:041602(R).

[Maruyama et al., 1998] Maruyama, T., Niita, K., Oyamatsu, K., Maruyama, T., Chiba, S., and Iwamoto, A. (1998). Phys. Rev. C, 57:655.

[Maruyama et al., 2005] Maruyama, T., Tatsumi, T., Voskresensky, D., Tanigawa, T., and Chiba, S. (2005). Phys. Rev. C, 72:015802.

[Matsui, 1981] Matsui, T. (1981). Nucl. Phys. A, 370:365.

[Moessner and Ramirez, 2006] Moessner, R. and Ramirez, A. P. (2006). Phys. Today, 59:No. 2, 24.

[Müller and Serot, 1995] Müller, H. and Serot, B. D. (1995). Phys. Rev. C, 52:2072.

[Newton, 2008] Newton, W. G. (2008). PhD thesis, Oxford University.

[Newton and Stone, 2009] Newton, W. G. and Stone, J. R. (2009). Phys. Rev. C, 79:055801.

[Nielsen et al., 1994] Nielsen, M., da Providência, C., da Providência, J., and Lin, W.-R. (1994). Mod. Phys. Lett. A, 10:919.

[Nielsen et al., 1991] Nielsen, M., Providência, C., and da Providência, J. (1991). Phys. Rev. C, 44:209.

[Nielsen et al., 1993] Nielsen, M., Providência, C., and da Providência, J. (1993). Phys. Rev. C, 47:200.

[Ofengeim and Yakovlev, 2015] Ofengeim, D. D. and Yakovlev, D. G. (2015). Europhys. Lett., 112:59001.

[Olausen and Kaspi, 2014] Olausen, S. A. and Kaspi, V. M. (2014). Astrophys. J. Supp. S., 212:1.

[Pais, 2013] Pais, H. (2013). PhD thesis, The University of Tennessee, Knoxville.

[Pais et al., 2015] Pais, H., Chiacchiera, S., and Providência, C. (2015). Phys. Rev. C, 91:055801.

[Pais et al., 2009] Pais, H., Santos, A., and Providência, C. (2009). Phys. Rev. C, 80:045808.

[Pais and Stone, 2012] Pais, H. and Stone, J. R. (2012). Phys. Rev. Lett., 109:151101.

[Pais et al., 2016] Pais, H., Sulaksono, A., Agrawal, B. K., and Providência, C. (2016). Phys. Rev. C, 93:045802.

[Pethick et al., 1995] Pethick, C. J., Ravenhall, D. G., and Lorenz, C. P. (1995). Nucl. Phys. A, 584:675.

[Pons et al., 2013] Pons, J. A., Viganò, D., and Rea, N. (2013). Nature Phys., 9:431.

[Prakash et al., 1997] Prakash, M., Bombaci, I., Prakash, M., Ellis, P. J., Lattimer, J. M., and Knorren, R. (1997). Phys. Rep., 280:1.

[Providência, 2007] Providência, C. (2007). Int. J. Mod. Phys. E, 16:2680.

[Providência et al., 2006a] Providência, C., Brito, L., Avancini, S. S., Menezes, D. P., and Chomaz, P. (2006a). Phys. Rev. C, 73:025805.

[Providência et al., 2006b] Providência, C., Brito, L., Santos, A. M. S., Menezes, D. P., and Avancini, S. S. (2006b). Phys. Rev. C, 74:045802.

[Rabhi et al., 2008] Rabhi, A., Providência, C., and da Providência, J. (2008). J. Phys. G: Nucl. Part. Phys., 35:125201.

[Rabhi et al., 2009a] Rabhi, A., Providência, C., and da Providência, J. (2009a). Phys. Rev. C, 79:015804.

[Rabhi et al., 2009b] Rabhi, A., Providência, C., and da Providência, J. (2009b). Phys. Rev. C, 80:025806.

[Raduta and Gulminelli, 2010] Raduta, A. R. and Gulminelli, F. (2010). Phys. Rev. C, 82:065801.

[Ravenhall and Pethick, 1994] Ravenhall, D. G. and Pethick, C. J. (1994). Astrophys. J., 424:846.

[Ravenhall et al., 1983] Ravenhall, D. G., Pethick, C. J., and Wilson, J. R. (1983). Phys. Rev. Lett., 50:2066.

[Ring, 1996] Ring, P. (1996). Prog. Part. Nucl. Phys., 37:193.

[Ring and Schuck, 1980] Ring, P. and Schuck, P. (1980). The Nuclear Many-Body Problem. Springer-Verlag, New York.

[Sakuragi, 2016] Sakuragi, Y. (2016). Prog. Theor. Exp. Phys., 06:106.

[Santos et al., 2008] Santos, A., Brito, L., and Providência, C. (2008). Phys. Rev. C, 77:045805.

[Schneider et al., 2014] Schneider, A. S., Berry, D. K., Briggs, C. M., Caplan, M. E., and Horowitz, C. J. (2014). Phys. Rev. C, 90:055805.

[Schneider et al., 2016] Schneider, A. S., D. K. Berry, M. E. C., Horowitz, C. J., and Lin, Z. (2016). Phys. Rev. C, 93:065806.

[Serot and Walecka, 1995] Serot, B. D. and Walecka, J. D. (1995). Ad. Nuc. Phys, 16:1.

[SGR Catalogue, 2009] SGR Catalogue (2009). http://www.physics.mcgill.ca/ pulsar/magnetar/main.html.

[Shapiro and Teukolsky, 2004] Shapiro, S. L. and Teukolsky, S. A. (2004). Black Holes, White Dwarfs, and Neutron Stars: The physics of Compact Objects. WILEY, Weinheim.

[Sharma, 2013] Sharma, R. (2013). Seminar presentaton in Los Alamos National Laboratory.

[Shen et al., 1998] Shen, H., Toki, H., Oyamatsu, K., and Sumiyoshi, K. (1998). Nucl. Phys. A, 637:435.

[Skyrme, 1956] Skyrme, T. H. R. (1956). Phil. Mag., 1:1043.

[Sonoda et al., 2007] Sonoda, H., Watanabe, G., Sato, K., Takiwaki, T., Yasuoka, K., and Ebisuzaki, T. (2007). Phys. Rev. C, 75:042801(R).

[Sonoda et al., 2008] Sonoda, H., Watanabe, G., Sato, K., Yasuoka, K., and Ebisuzaki, T. (2008). Phys. Rev. C, 77:035806.

[Sonoda et al., 2010] Sonoda, H., Watanabe, G., Sato, K., Yasuoka, K., and Ebisuzaki, T. (2010). Phys. Rev. C, 81:049902.

[Sumiyoshi et al., 1995] Sumiyoshi, K., Kuwabara, H., and Toki, H. (1995). Nucl. Phys. A, 581:725.

[Tsang et al., 2012] Tsang, M. B., Stone, J. R., Camera, F., Danielewicz, P., Gandolfi, S., Hebeler, K., Horowitz, C. J., Lee, J., Lynch, W. G., Kohley, Z., Lemmon, R., Möller, P., Murakami, T., Riordan, S., Roca-Maza, X., Sammarruca, F., Steiner, A. W., Vidaña, I., and Yennello, S. J. (2012). Phys. Rev. C, 86:015803.

[Tsang et al., 2009] Tsang, M. B., Zhang, Y., Danielewicz, P., Famiano, M., Li, Z., Lynch, W. G., and Steiner, A. W. (2009). Phys. Rev. L, 102:122701.

[Turolla et al., 2015] Turolla, R., Zane, S., and Watts, A. L. (2015). Rep. Prog. Phys., 78:116901.

[Urban and Oertel, 2015] Urban, M. and Oertel, M. (2015). Int. J. Mod. Phys. E, 24:1541006.

[Vicentini et al., 1985] Vicentini, A., Jacucci, G., and Pandharipande, V. R. (1985). Phys. Rev. C, 31:1783.

[Vidaña et al., 2009] Vidaña, I., Providência, C., Polls, A., and Rios, A. (2009). Phys. Rev. C, 80:045806.

[Walecka, 1974] Walecka, J. D. (1974). Ann. Phys., 83:491.

[Watanabe et al., 2001] Watanabe, G., Iida, K., and Sato, K. (2001). Prog. Theor. Phys., 106:551.

[Watanabe et al., 2005] Watanabe, G., Maruyama, T., Sato, K., Yasuoka, K., and Ebisuzaki, T. (2005). Phys. Rev. Lett., 94:031101.

[Watanabe and Sonoda, 2005] Watanabe, G. and Sonoda, H. (2005). AIP Conf. Proceed., 791:101.

[Watanabe and Sonoda, 2007] Watanabe, G. and Sonoda, H. (2007). Soft Condensed Matter. Nova Science Publishers Inc, New York.

[Worley et al., 2008] Worley, A., Krastev, P. G., and Li, B. (2008). Astrophys. J., 685:390.

[Xu et al., 2008] Xu, J., Chen, L. W., Li, B. A., and Ma, H. R. (2008). Phys. Rev. C, 77:014302.

[Xu et al., 2009] Xu, J., Chen, L. W., Li, B. A., and Ma, H. R. (2009). Astrophys. J., 697:1549.

[Xu et al., 2000] Xu et al., H. S. (2000). Phys. Rev. Lett., 85:716.

[Yakovlev, 2015] Yakovlev, D. G. (2015). Mon. Not. R. Astron. Soc., 453:581.

[Yakovlev et al., 2001] Yakovlev, D. G., Kaminkera, A. D., Gnedinc, O. Y., and Haensel, P. (2001). Phys. Rep., 354:1.

[Yuan and Zhang, 1999] Yuan, Y. F. and Zhang, J. L. (1999). Astrophys. J., 525:950.

[Yue and Shen, 2006] Yue, P. and Shen, H. (2006). Phys. Rev. C, 74:045807.